Progress in Materials Science 137 (2023) 101126

Contents lists available at ScienceDirect

Progress in Materials Science

journal homepage: www.elsevier.com/locate/pmatsci

Multiaxial fatigue of additively manufactured metallic components: A review of the failure mechanisms and fatigue life prediction methodologies

Pietro Foti [a], Nima Razavi [a], Ali Fatemi [b], Filippo Berto [a,c,*]

[a] Department of Mechanical and Industrial Engineering, Norwegian University of Science and Technology (NTNU), Trondheim, Norway
[b] Department of Mechanical Engineering, University of Memphis, Memphis, TN, USA
[c] Department of Chemical Engineering, La Sapienza University of Rome, Rome, Italy

ARTICLE INFO

Keywords:
Additive manufacturing
Multiaxial fatigue
Fatigue damage assessment
Crack initiation
Crack growth
Life predictions

ABSTRACT

Additive manufacturing techniques offer significant advantages over conventional manufacturing methods. These include the possibility of realizing highly customized components in which not only can the geometry be defined with a high degree of freedom, but the material composition or geometrical properties can also be manipulated throughout the component by introducing lattice structure zones. Such variations cannot be realized using conventional manufacturing techniques. However, the application of additively manufactured parts at the industrial scale is still limited owing to the high variability in mechanical properties, which also makes it difficult to define feasible tools to assess their structural integrity and determine their expected fatigue life with a sufficient degree of reliability. In addition, real components often experience multiaxial stresses at critical locations owing to their geometry or service-loading conditions. Thus, a proper understanding of the fatigue performance of additively manufactured components with complex geometries cannot neglect the consideration of multiaxial stress states. This review presents an overview of multiaxial fatigue in additively manufactured metallic components, providing insights into crack initiation sites and growth orientations and relating them to the fatigue failure mechanisms in these components. The principal life prediction methodologies applied for the fatigue damage assessment of additively manufactured components under multiaxial fatigue loading are presented, with a particular focus on their accuracy in correlating fatigue data obtained for different loading conditions.

1. Introduction

Additive manufacturing (AM) has gained significant attention in recent years for a wide range of applications in various industries such as aerospace [1–14], automotive [15–26], biomedical [27–38], and nuclear [39]. This is due to the numerous advantages that AM can offer: it allows the realization of components with complex geometries that cannot be realized through conventional techniques [40]; it can create highly customized components in which the mechanical properties can be varied by manipulating the geometry, such as with architectural materials [40–54], or varying the material feedstock throughout the component [55–68]; it allows for the fabrication of replacement parts [69]. A prosthesis may be the best example of utilizing all the advantages of AM [50,70–80]. Indeed,

* Corresponding author.
E-mail addresses: filippo.berto@ntnu.no, filippo.berto@uniroma1.it (F. Berto).

https://doi.org/10.1016/j.pmatsci.2023.101126
Received 5 August 2022; Received in revised form 28 March 2023; Accepted 30 March 2023
Available online 14 April 2023

as we can see from Fig. 1, the geometries of the components are particularly complex because of the need to be patient-specific and mimic the mechanical behavior of bones with a smooth solid surface and a lattice core; in addition, different materials can be used to meet the needs for strength and biocompatibility.

However, despite their promising features, AM components are still not considered reliable for safety-critical or large-scale applications [40]. This is mainly due to the significant lack of understanding of their mechanical behavior, which is more complex owing to the synergistic effect of a wide range of variables and processes and post-process parameters typical for each fabrication process, resulting in a different final structure of each AM component [83–89]. The process parameters for laser powder bed fusion (LPBF) are known to affect the microstructure, residual stresses, surface roughness, and defect morphologies, including scanning speed, laser power, and hatch spacing [90,91]. In addition to the process parameters and post-processing heat treatments [92–98], the component size [99], geometry, orientation, and quantity on the build platform can affect the mechanical properties. This is due to the different thermal dissipation histories during the process due to the various times required for the deposition of each layer [100–103]. Such variations may also result in different behaviors between laboratory specimens and full-scale parts [69].

The industrial-scale application of AM components depends on the availability of feasible tools to assess their structural integrity and determine their expected fatigue life with a sufficient level of reliability. The fatigue phenomenon represents a demanding task for researchers, even with conventionally manufactured components for which there is already a certain degree of expertise gained by many years of research and experimental observations [104–115]. Regarding AM, the understanding of the fatigue phenomenon is further limited by the recency of the processes and their continuous development, the peculiarities of the AM components, variabilities associated with process parameters and post-process treatments, and the very limited amount of experimental data owing to their limited applications.

As demonstrated by Molaei et al. [116] (see Fig. 2), the monotonic tensile strength of AM materials is a poor indicator of fatigue performance owing to variations in the microstructure, defects, residual stresses, and phenomena such as cyclic softening or hardening [117]. However, it is worth noting that research efforts have not only been devoted to the correlation between monotonic behavior and fatigue properties in conventional materials [118–122] but also with some AM materials [123] even though the greater sensitivity of fatigue behavior to the microstructure and defect features makes the finding of such relationships a demanding task [124].

The operational loading conditions of a component in most applications are non-periodic multiaxial [125–127], which are considerably different from those typically studied in research laboratories [128–140] which usually only consider the simplest loading condition, i.e., uniaxial loading. However, even simple loading conditions can result in a local multiaxial stress state owing to the complexity of the geometry [52,141–145], the presence of multidirectional residual stresses [117,146] or the anisotropy determined by the microstructure [100,147,148] and directional lack of fusion (LOF) defects [149–154]. Other issues include the fatigue regime considered [155–159], the effect of loading ratio [160–162], the non-periodicity of the load history in real applications [125,163–166] and the orientation of the loading direction, which changes continuously. For example, Molaei and Fatemi [167] investigated the load history extracted from full-scale flight test data of the lower wing skin of a P-3C aircraft [168].

An important aspect highlighted by Molaei et al. [169] is the variation in the material composition near the defects, which may lead to significant changes in the mechanical properties. Considering the local nature of the fatigue failure, such a variation in the local mechanical properties may contribute to the scatter of the fatigue test data. Some of these AM peculiarities may be reduced by tight control of the process parameters [170–172] or by involving post-processing techniques in the production chain. For instance, residual stresses in AM parts are generally difficult to avoid owing to the nature of AM processes that involve severe temperature gradients and

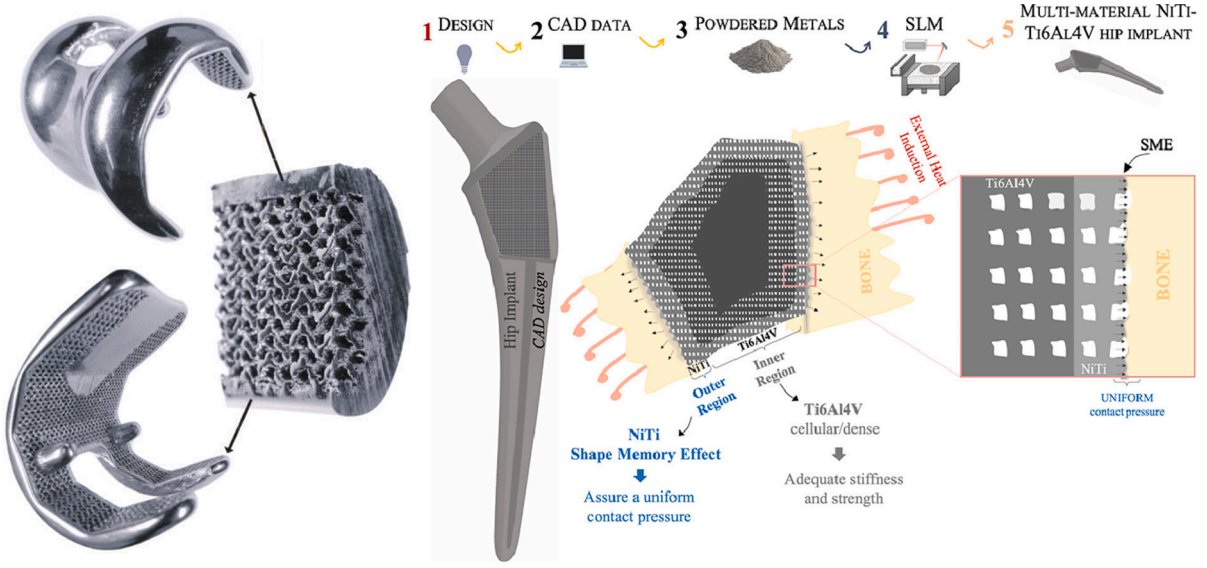

Fig. 1. Examples of complex components realized through AM. Figure adapted from [81,82].

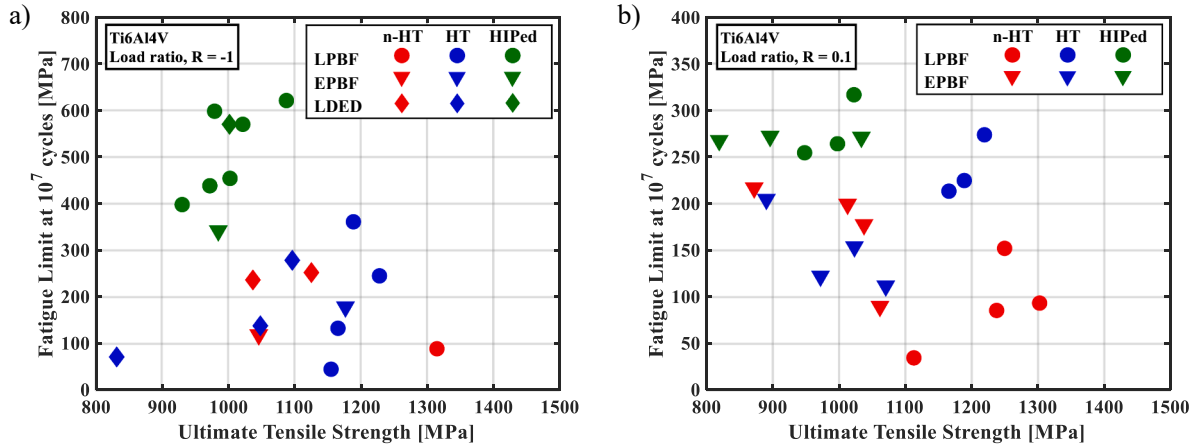

Fig. 2. Fatigue limit defined as fatigue strength at 10^7 cycles vs. monotonic ultimate tensile strength for AM Ti6Al4V in as-built non-heat-treated (n-HT), annealed and/or heat-treated (HT) and hot isostatic pressed (HIPed) conditions for a) R = −1 and b) R = 0.1 stress ratios. Figure adapted from [116].

sharp cooling rates [69]; however, post-processing techniques, such as annealing, have been proven to be effective in reducing their magnitude [93,96,97,146,149,172–179] while post-processing techniques such as hot isostatic pressing (HIP) have been shown to improve the fatigue properties of AM components by changing the defect sizes and morphologies [69].

A wide variety of materials can be processed by AM, such as polymers, metals, ceramics, and composites [180]; however, this review focuses on the multiaxial fatigue of LPBF metal materials and components owing to the lack of sufficient experimental fatigue data under multiaxial loadings for other AM techniques and materials to provide a sufficient overview. It should be noted that, for the same reason, the examples provided in this work mainly focus on LPBF parts. On the other hand, the concepts and considerations about the modelling approaches discussed are more general. Indeed, even if other metal AM technics, such as EB-PBF or DED, may result in different surface finish and defect populations, the discussions regarding their effects on the multiaxial fatigue behaviour of AM metals are expected to be similar, resulting in a more general validity of the discussions provided in the present work.

The main aim of this review is to promote the research in multiaxial fatigue of AM components and to provide guidelines for experimental and theoretical evaluation of the key factors affecting the multiaxial fatigue behavior of AM parts. A widely documented basis on the topic of multiaxial fatigue is indeed fundamental to achieve well-grounded conclusions leading to a proper understanding of this phenomenon and to the development of design methodologies able to ensure the necessary degree of reliability for the industrial application of AM components.

The present review is organized as follows: Section 2 provides an overview of the specimen geometries utilized to investigate multiaxial loading conditions that can be found in the literature; Section 3 focuses on the crack initiation sites and growth orientation, providing insight on the parameters that affect them; Section 4 presents the fatigue prediction methodologies that can be used in dealing with multiaxial fatigue, providing examples of application and comparisons with experimental data to evaluate their accuracy; Section 5 presents the fatigue performance of a real AM component compared with laboratory specimen test results; finally, a summary and final remarks are presented in Section 6. These studies included fatigue data and analyses for LPBF Ti6Al4V and 17-4 PH alloys and different stress states resulting from axial, torsional, and combined axial–torsional loads. Many effects were considered in these studies including defects, surface roughness, anisotropy, post treatments such as HIP, as well as effects often present at the component level such as stress concentrations or notches and variable amplitude loads.

2. Some specimen geometries used for multiaxial fatigue investigation

The mechanical behavior of the material is typically investigated using specimens whose geometry is dependent on the objective of the investigation and the available testing machines that are used to characterize the mechanical behavior of materials and mechanical components. The experimental multiaxial fatigue data available in the literature were obtained from specimens according to the ASTM E2207-08 [181] standard. The specimen in Fig. 3a has a tubular thin-walled circular cross-section in which the wall thickness has a value small enough to meet the thin-walled assumption. Special care should be taken regarding specimen alignment to avoid spurious loads [182].

The possible influences of specimen geometry on the achieved fatigue results have been highlighted in the literature dealing with conventionally manufactured specimens [183–185]. To deal with AM, Fatemi et al. [186] proposed specimen geometries intended to reduce unintentional stress concentrations and stress gradients throughout the wall thicknesses to obtain more uniform stress states in the gauge section. The requirement for the thin-walled assumption results in some issues such as the difficulty of maintaining the concentricity of the inside and outside diameters, the possibility of having an insufficient number of material grains in the cross-section to meet the continuum assumption, and the possibility of buckling during either compression or shear loading. However, AM also

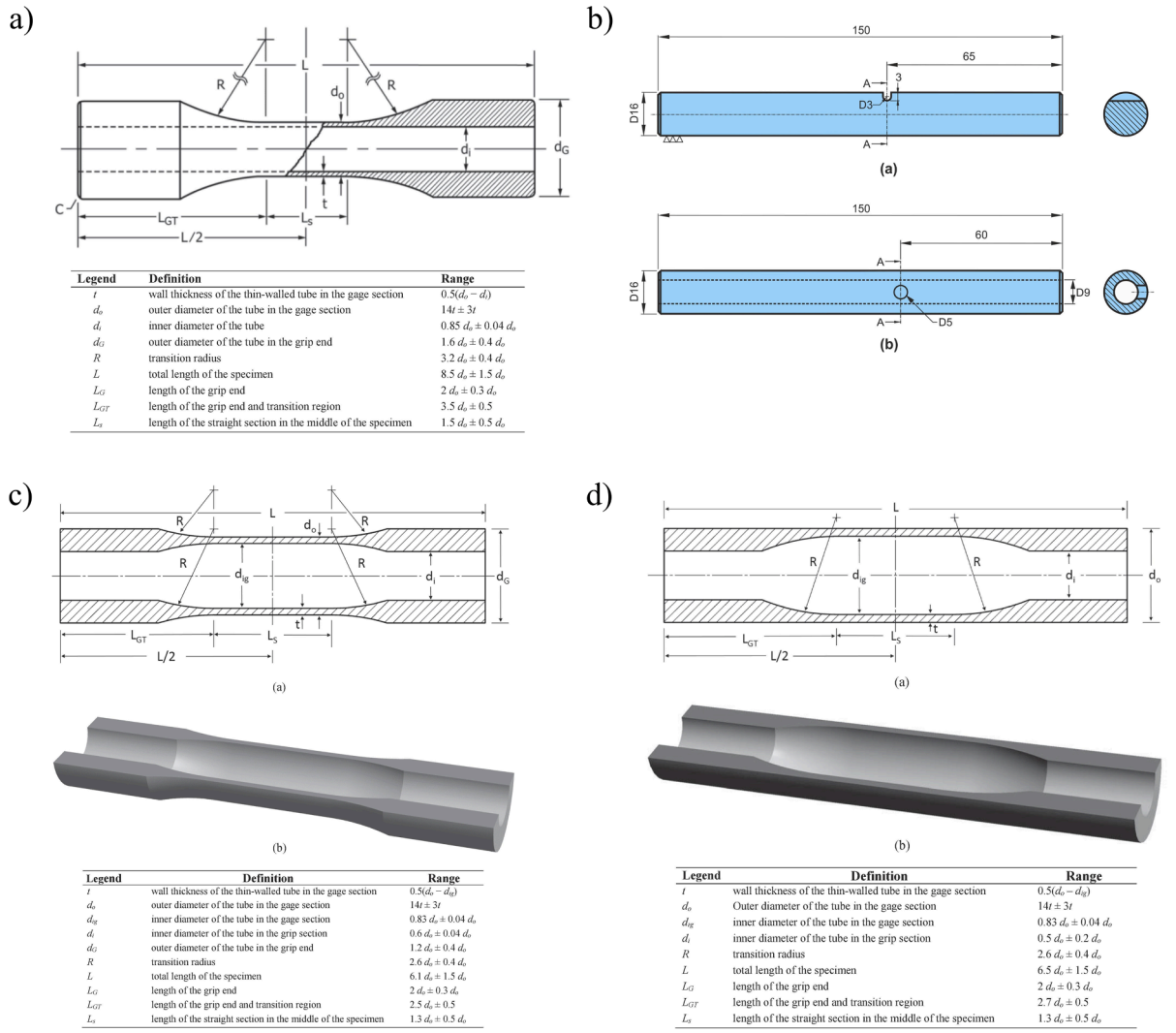

Legend	Definition	Range
t	wall thickness of the thin-walled tube in the gage section	$0.5(d_o - d_i)$
d_o	outer diameter of the tube in the gage section	$14t \pm 3t$
d_i	inner diameter of the tube	$0.85\ d_o \pm 0.04\ d_o$
d_G	outer diameter of the tube in the grip end	$1.6\ d_o \pm 0.4\ d_o$
R	transition radius	$3.2\ d_o \pm 0.4\ d_o$
L	total length of the specimen	$8.5\ d_o \pm 1.5\ d_o$
L_G	length of the grip end	$2\ d_o \pm 0.3\ d_o$
L_{GT}	length of the grip end and transition region	$3.5\ d_o \pm 0.5$
L_s	length of the straight section in the middle of the specimen	$1.5\ d_o \pm 0.5\ d_o$

Legend	Definition	Range
t	wall thickness of the thin-walled tube in the gage section	$0.5(d_o - d_{ig})$
d_o	outer diameter of the tube in the gage section	$14t \pm 3t$
d_{ig}	inner diameter of the tube in the gage section	$0.83\ d_o \pm 0.04\ d_o$
d_i	inner diameter of the tube in the grip section	$0.6\ d_o \pm 0.04\ d_o$
d_G	outer diameter of the tube in the grip end	$1.2\ d_o \pm 0.4\ d_o$
R	transition radius	$2.6\ d_o \pm 0.4\ d_o$
L	total length of the specimen	$6.1\ d_o \pm 1.5\ d_o$
L_G	length of the grip end	$2\ d_o \pm 0.3\ d_o$
L_{GT}	length of the grip end and transition region	$2.5\ d_o \pm 0.5$
L_s	length of the straight section in the middle of the specimen	$1.3\ d_o \pm 0.5\ d_o$

Legend	Definition	Range
t	wall thickness of the thin-walled tube in the gage section	$0.5(d_o - d_{ig})$
d_o	Outer diameter of the tube in the gage section	$14t \pm 3t$
d_{ig}	inner diameter of the tube in the gage section	$0.83\ d_o \pm 0.04\ d_o$
d_i	inner diameter of the tube in the grip section	$0.5\ d_o \pm 0.2\ d_o$
R	transition radius	$2.6\ d_o \pm 0.4\ d_o$
L	total length of the specimen	$6.5\ d_o \pm 1.5\ d_o$
L_G	length of the grip end	$2\ d_o \pm 0.3\ d_o$
L_{GT}	length of the grip end and transition region	$2.7\ d_o \pm 0.5$
L_s	length of the straight section in the middle of the specimen	$1.3\ d_o \pm 0.5\ d_o$

Fig. 3. Specimen geometries for multiaxial loading conditions: a) ASTM E2207-08 [181] thin-walled tubular specimen; b) specimen geometry proposed by Macek et al. [187]; c) thin-walled tubular double-curve specimen proposed by Fatemi and Molaei [186]; d) thin-walled tubular straight outside-diameter specimen proposed by Fatemi and Molaei [186]. Figure adapted from [186,187].

allows for the use of other geometries to investigate the multiaxial fatigue properties. Fatemi and Molaei [186] proposed new specimen geometries (see Fig. 3c and d) with the aim of increasing the wall thickness, while still meeting the conditions for the thin-walled assumption. The proposed geometries also have the advantages of a higher tolerance for internal defects, such as voids and pores, and strengthening the material continuum assumption. In addition, the length of the specimens is reduced, leading to lower expenses for specimen production, and the larger cross-section leads to a higher buckling resistance and a reduction of unintended stress concentration, which also leads to a more uniform stress state in the gauge length.

Other specimen geometries that are used to investigate the multiaxial fatigue behavior of AM components can also be found in the literature, such as those considered by Macek et al. [187] (Fig. 3b).

3. Initiation sites and crack orientations

3.1. Initiation sites

While wrought metals usually have fatigue failures initiating from microscopic regions of localized plastic deformation and grain boundaries resulting from dislocations and slip systems [117], the fatigue performance of AM components is highly affected by internal defects and the high roughness of the as-built surface [116]. The extent of their influence on the fatigue behavior is dependent on the ductility of the material and the microstructure, which is dependent on the type of AM process used for fabrication and post-fabrication treatments [69]. Therefore, a deep understanding of AM defects is of paramount importance for properly assessing the structural

integrity and fatigue behavior of AM components. The most common defects in AM components include unmelted powders, pores due to entrapped gas, LOF defects with irregular shapes, and rough surface defects determined by the production processes. The morphology of these defects can be complex [152], but it can be described by several parameters, such as size, location, and shape, whose influence on the fatigue performance of AM components have been investigated in the literature [152,188–193]. 3D analysis of defects [152,194] is particularly useful dealing with multiaxial fatigue loading, providing information such as diameter, volume, morphology (e.g., sphericity and aspect ratio), and projected area of the volume on various planes, considering that under multiaxial loading, the orientation of the defects may influence the fatigue performance. Fig. 4 shows an example of a variety of defect morphologies that can be found in AM components. In addition, the defect features may also be correlated between themselves; for instance, variability in defect shape and size has been noticed with changing location, especially in as-built surface specimens [152]. For a deeper understanding of defect formation, we refer the reader to [152,195,196]. To determine possible initiation sites in AM components under a generic loading condition, in situ full-field measurements carried out through infrared (IR) thermography or digital image correlation (DIC) can be useful for investigating the strain evolution during the fatigue experiment, as shown by Renzo et al. [197]. The application of thermographic techniques could also prove useful in the real-time monitoring of AM components to overcome the high randomness in the fatigue properties. Renzo et al. [198] monitored the thermal behavior of AM components during multiaxial fatigue loading and showed that a thermographic approach can help identify the most critical point that results in the failure of the component from the first cycles of the fatigue life, as shown in Fig. 5.

3.1.1. Surface conditions

If the surface remains in the as-built condition, the fatigue performance of an AM component is mainly affected by the surface roughness [117,153,199] making aspects such as the microstructure and internal defect sizes and distributions less relevant [167]. The surface roughness is significantly affected by different parameters, such as the specific AM process used [200,201], powder characteristics [202], process parameters [203–205] and post-processing treatments [206,207].

Owing to the layer-by-layer build fashion of AM processes, the surface defects are usually distributed perpendicular to the building direction, creating a network of defects whose alignment with respect to the loading direction can significantly affect the failure mechanism [117,153,208]. Considering this behavior, the orientation of the loading direction with respect to the building direction can result in significant changes in the fatigue strength [205] owing to different values of surface roughness. Several works are available in literature that attempt to apply analytical models considering the surface roughness [192,201,209–211].

Fig. 6 shows how the rough surface of an as-built component results in multiple crack initiation sites that, after a first independent growth, coalesce to failure. Examples of multiple initiation sites for as-built surface specimens have also been reported in [153].

Machining the surfaces of AM components can improve the fatigue performance [200]; combining HIP and subsequent machining of the external surface, when possible, can avoid the influences of both defects and surface roughness on the fatigue behavior [169,212–214]. However, as shown in Fig. 7a and b, in HIPed components, there are still some residual defects that can act as possible crack initiation sites.

Molaei et al. [169] demonstrated through 2D defect studies how the HIP process has almost no effect on pores in LPBF Ti6Al4V owing to the presence of pressurized entrapped argon gas inside and its low solubility in titanium [94]; the gas pores can act as a failure initiation site, as shown in Fig. 7c. In addition, the HIP process does not affect open pores or surface roughness, as shown in Fig. 7b [169,179,209,212,215,216] leading to crack initiation from the outer surface under torsional loading, as shown in Fig. 7d. Regardless of the heat-treatment conditions, when a rough surface is present, the cracking behavior is mainly controlled by surface defects. In addition, it is worth underlining that the machining of the surface must be performed after the HIP treatment owing to the lack of effect

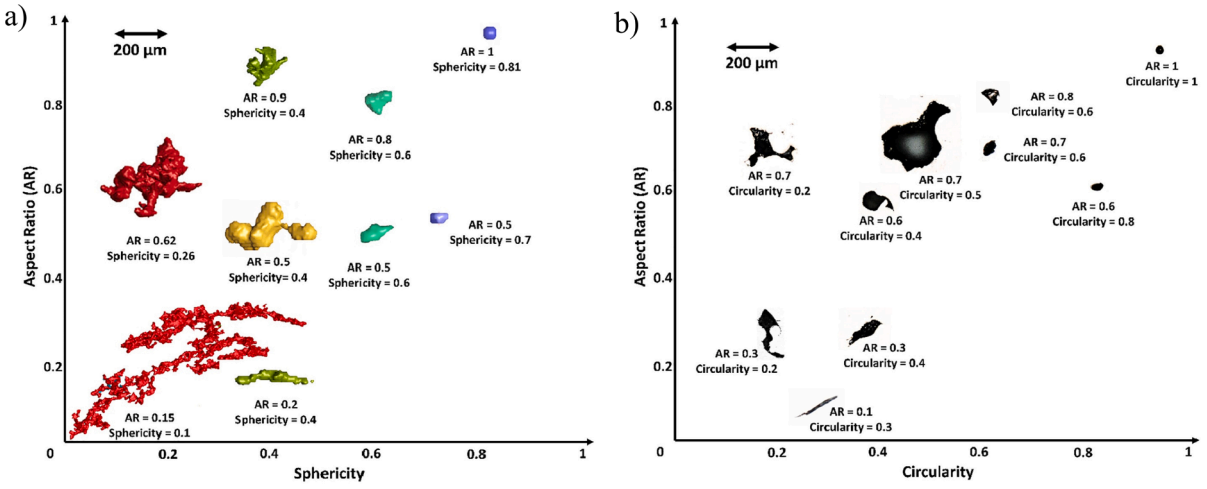

Fig. 4. Defect morphologies in Ti6Al4V annealed specimens obtained through: a) micro-computed tomography results; b) optical microscopy observation (relative size of defects is shown). Figure adapted from [152].

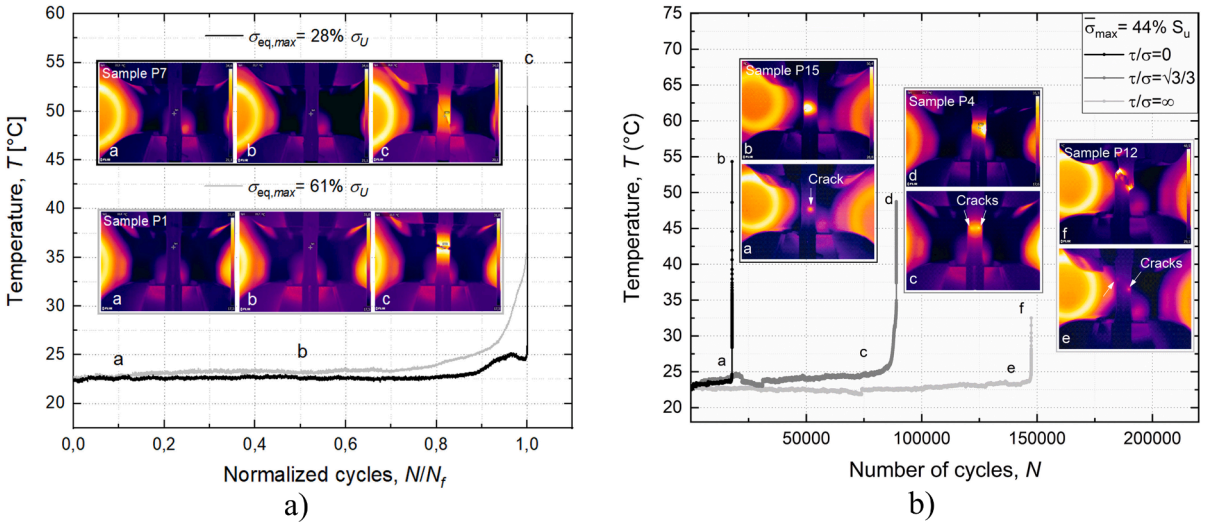

Fig. 5. Temperature evolution for: a) two different applied stress amplitudes for in-phase axial and torsional loading; b) different load conditions at the same equivalent stress amplitude. In each specimen, it is possible to observe from the beginning the failure initiation site in the component. Figure adapted from [198].

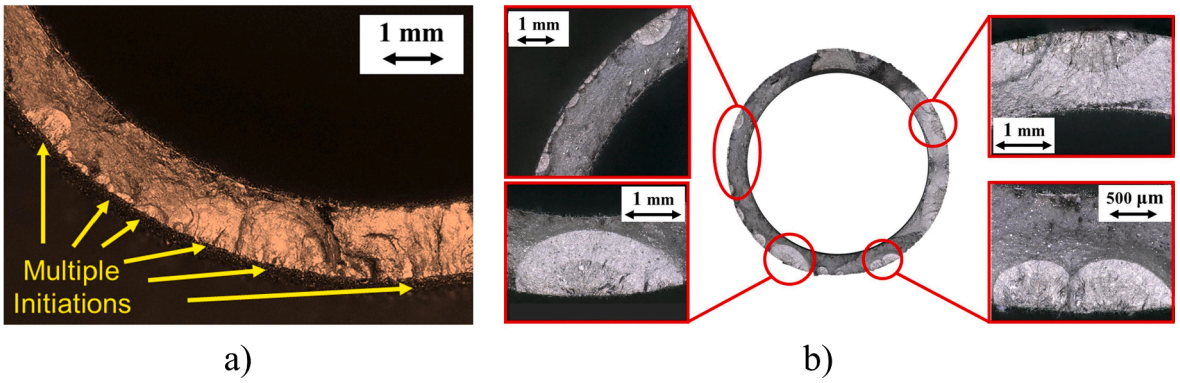

Fig. 6. Multiple crack initiations on an LPBF as-built surface of: a) Ti6Al4V specimen under axial-torsion variable amplitude loading; b) 17-4 PH specimen under combined in-phase axial-torsion loading. Figure adapted from [153,167].

this process has on surface defects [199].

A proper combination of process parameters and post-processing treatments may result in fatigue properties for AM components comparable with those of their wrought counterparts, as can be seen in Fig. 8a [169]. However, it is also worth reporting that such post-processing treatments, even if beneficial for the fatigue performance, do not always ensure that AM materials have a fatigue strength that is comparable with the conventional ones, as shown by Fatemi et al. [199]. They documented inferior fatigue performance of AM parts compared to their wrought counterparts under both as-built and machined surface conditions. However, in [199], the inferior performance even after the post-processing treatments depended also on the fabrication process parameters that resulted in larger initial defects. Moreover, in some applications, surface machining of a complex component could be difficult and expensive, and in applications such as biomedical and orthopedic implants, rough surfaces are preferred over smooth ones [167].

Post-processing techniques can also impact the component microstructure. For instance, HIP treatment, owing to its key parameters such as temperature, pressure, and time, can result in microstructural changes [217]. Even if the HIP process has beneficial effects on the fatigue life by reducing the defect size and altering the morphology, microstructure coarsening can reduce this beneficial effect [178]. In this regard, the key parameters of the HIP process should be chosen considering the possible effects on the microstructure to obtain the highest improvement from this post-processing technique.

When a surface can be machined to achieve a lower roughness, internal defects may become dominant in determining the fatigue behavior of the AM component. Regarding multiaxial fatigue loadings, Molaei and Fatemi [167] applied the critical plane approach and identified a plausible explanation for the lower performance regarding internal defects of machined samples; that is, by machining the surface, the internal defects, whose distribution are more random, determine a higher degree of uncertainty in the experimental data.

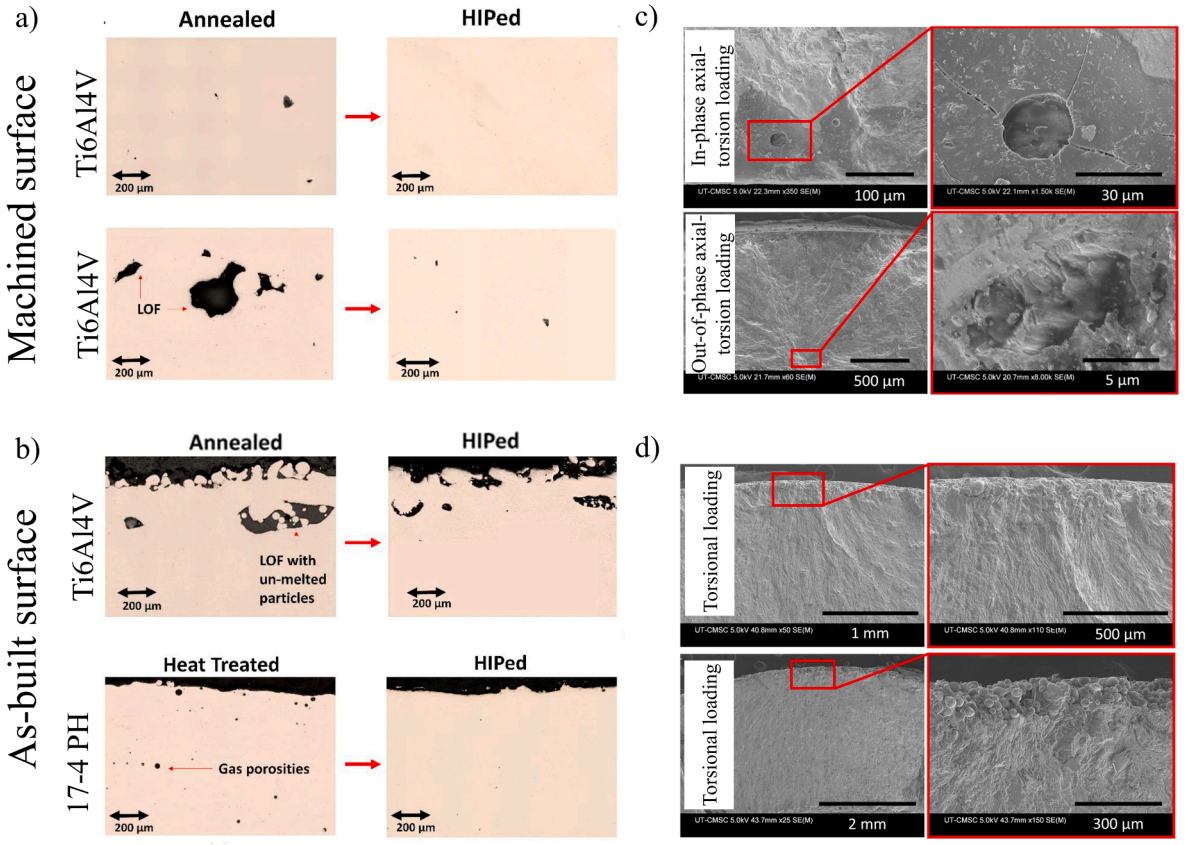

Fig. 7. Defect morphologies representative of AM metals subjected to post-processing heat treatments under a) machined and b) as-built surface conditions; c) fatigue crack initiation sites from internal defects for AM machined surface HIPed specimens; d) fatigue crack initiation sites from the external surface for AM as-built surface HIPed specimens. Figure adapted from [169,188].

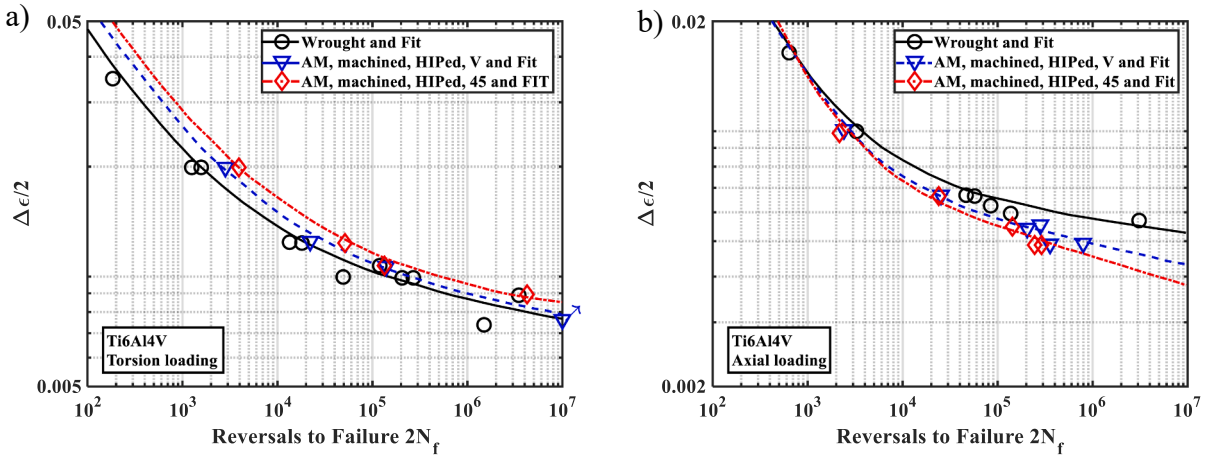

Fig. 8. Test results for wrought and AM HIPed machined Ti6Al4V specimens under a) torsional loading and b) axial loading. Figure adapted from [169].

Considering the discussions above, the internal defect location has a leading role in the fatigue behavior [69] with the defect at or near the surface being more detrimental, as demonstrated by Fatemi et al. [218] through finite element (FE) simulations. However, it is worth noting that the internal defect location is also related to the applied loading conditions: when uniaxial loading is considered for machined surfaces, the internal defects assume a leading role in determining the fatigue behavior of the material, as shown by Zhang and Fatemi [200] while under loading conditions involving shear or bending, being a stress gradient, the defects near the surfaces

continue to assume a leading role in machined surface conditions. Fig. 8 shows the dependence of the fatigue properties on both the loading and surface conditions.

Even if machined components have higher fatigue lives compared to their as-built counterparts [193,199], their fatigue behavior is more difficult to predict due to the randomness of the defect distribution inside the component cross-sections that represent the most favorable crack initiation points, as seen in Fig. 7c. In addition, the depth of machining has been shown to influence the fatigue behavior of AM components [100,173] due to the near-surface defects that can be brought to the surface by machining; consequently, parameters describing the surface roughness alone are not indicative of the fatigue performance of an AM component, as shown by Molaei et al. [153] who documented different fatigue performances for specimens characterized by similar surface roughness parameters but obtained with different techniques (see Fig. 9). This apparent inconsistency in the effect of surface roughness must be attributed to the surface qualities achieved through different techniques. As seen in Fig. 9c, the polished samples exhibited inferior performance compared to the machined samples, in spite of both polished samples and machined samples having the same surface roughness. This is explained by sub-surface defects having moved to the surface due to the removal of approximately 150μm of material in the polished samples, while in the machined samples, all surface and near-surface defects were completely removed after removing 1mm of material.

3.1.2. Complex geometry and notch effect

AM processes are highly appreciated for their ability to fabricate geometrically complex components. However, a complex geometry can result in stress concentrators that may act as favorable fatigue initiation sites and can significantly lower the fatigue performance of an AM component [169,179,209,219–222]. Regarding multiaxial fatigue loadings, Molaei and Fatemi [167] studied notched and unnotched specimens both in the as-built and machined conditions and reported that the presence of global geometrical discontinuities, i.e., notches, may have a much higher detrimental effect than the surface conditions or internal defects that can be

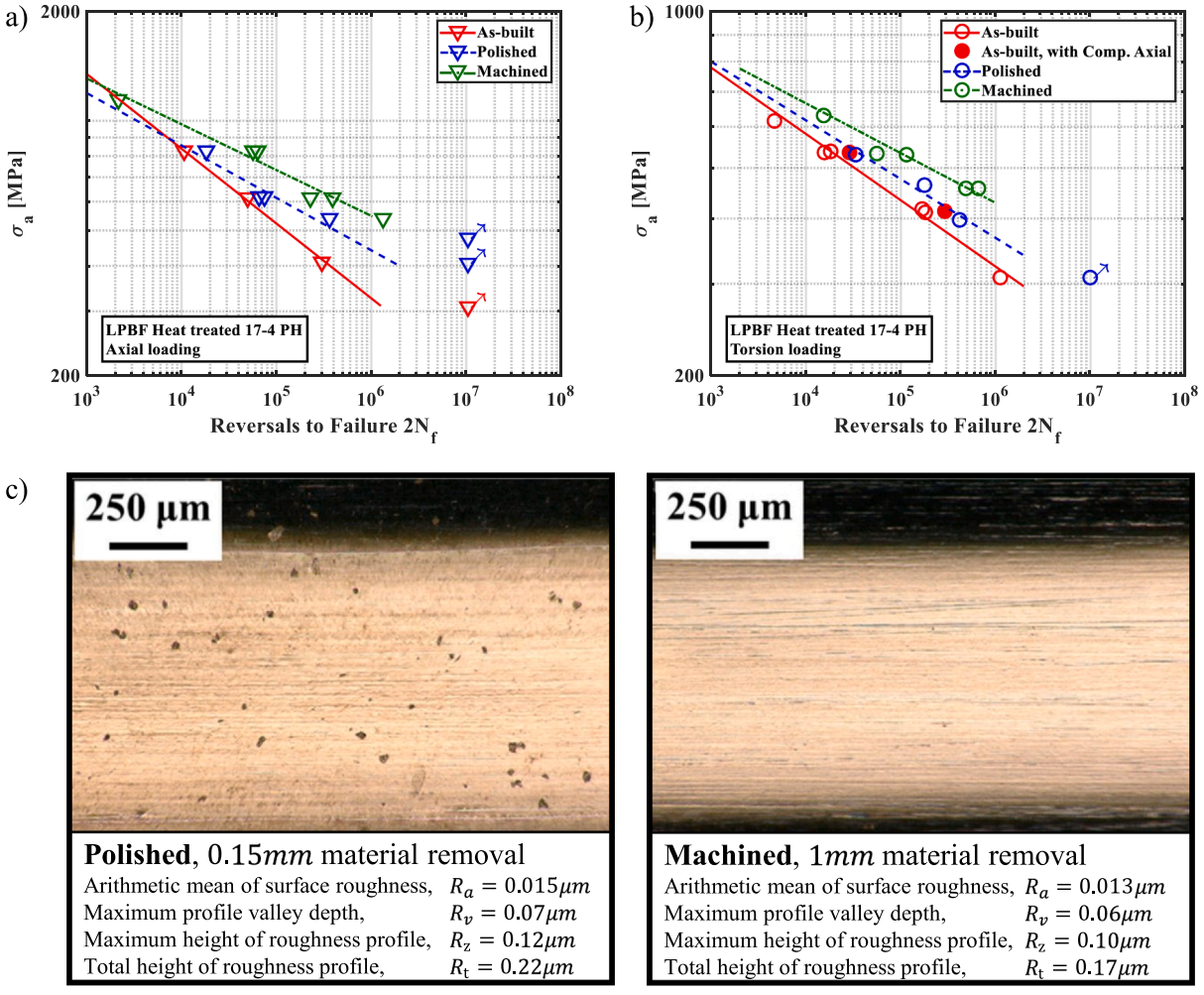

Fig. 9. Fatigue data for LPBF CA-H1025 heat-treated 17-4 PH specimens in as-built state and machined or polished to a similar surface roughness under a) axial and b) torsional loading; c) polished (left) and machined (right) surfaces of LPBF specimens. Figure adapted from [153].

considered as local geometrical discontinuities. However, inhomogeneities in the geometrical discontinuity region can further worsen the fatigue performance by making the crack initiation process easier, as also shown by Macek et al. [187], when studying the fatigue performance of AM 18Ni300 under multiaxial loading conditions. Fig. 10 shows an interlayer defect that acts as a crack initiation point.

The competing failure initiation sites determined by the rough surface, internal defects, and geometrical discontinuities are in accordance with the conclusions of Molaei et al. [223] in which the effects of the rough surface of unnotched as-built specimens are similar to the effect of a mechanically induced notch. From this perspective, both the unnotched and notched as-built surface specimens can be considered as notched specimens with different stress concentration factors. In other words, the notch leading to the higher stress concentration controls the failure of the specimen, as in the case reported in [167]. Indeed, depending on the mechanically induced notch geometry and the loading conditions, a geometrical discontinuity may determine conditions that can be either more or less detrimental than the conditions determined by the surface roughness or internal defects. It is also worth noting that competing effects can exist between the defects and microstructure; indeed, studies on the interaction effect of lamellae width and round pore diameters on the fatigue performance of AM Ti6Al4V have shown that defects with a diameter lower than eight times the microstructure characteristic length have no influence on microcrack growth [224].

Other studies on notched AM components under multiaxial fatigue loading are available in the literature. In [208], for the notch geometry considered, regardless of the loading and surface conditions, the location of crack initiation was determined by the highest stressed location along the geometrical discontinuity, as shown in Fig. 11. However, it is worth mentioning that the conclusion of [208] may not be a general conclusion for AM notched components, and the initiation location can vary depending on notch acuity. Additionally, when dealing with non-proportional loading conditions, the location of the maximum stress at the notch changes continuously throughout the loading, creating multiple possible locations for failure initiation [225].

An aspect that should not be neglected while studying the multiaxial fatigue behavior of notched components is how the notch has been created; indeed, several studies have been conducted on components with geometrical discontinuities created in a subsequent production step by drilling a hole in the component, which does not reflect the conditions that can be found in real AM components, in which the aim is to build geometrical discontinuities during the AM process. Molaei et al. [223] investigated this aspect by performing fatigue tests under multiaxial loading conditions for the specimen geometry shown in Fig. 3a, in which holes were created both during and after the AM process, as shown in Fig. 12. The component with the hole built during the AM process shows deviations from the designed geometry that could result in higher stress concentrations than expected and, therefore, premature failures. In addition, the roughness changes along the notch edges as a function of the surface orientation with respect to the building direction, which can potentially affect the fatigue failure initiation point due to induced higher stress concentration from both the stair stepping effect and the presence of overhanged partially melted particles.

However, it is worth underlining that the deviations between the expected and observed fatigue initiation sites were noticed only when dealing with torsional loading that had an expected failure initiation site in the top half of the hole where the roughness was highest. On the other hand, regardless of loading conditions, the fatigue properties were lower for the specimens with the hole built during the AM process, as compared to the specimens having the hole drilled in a subsequent step. It should be mentioned that machining of the AM component surface could be avoided if the surface roughness is low enough that the notch effect prevails; however, this would be highly dependent on the notch geometry, and its determination and achievement may not be a feasible task. Fatemi et al. [117] discussed that, if proper process parameters are used for fabrication, fatigue properties comparable to those of wrought material could also be obtained without HIPing the component. In addition, in an extended investigation of the notch–defect interaction, Solberg et al. [220] showed that the defects along a geometrical discontinuity may determine a change in the failure initiation site, as shown in Fig. 13, depending on the notch acuity and surface roughness.

The conclusions obtained by Solberg et al. [220] are related to the change in surface roughness in as-built conditions owing to the various orientations of external surfaces with respect to the building direction obtained through different notch geometries. Regarding

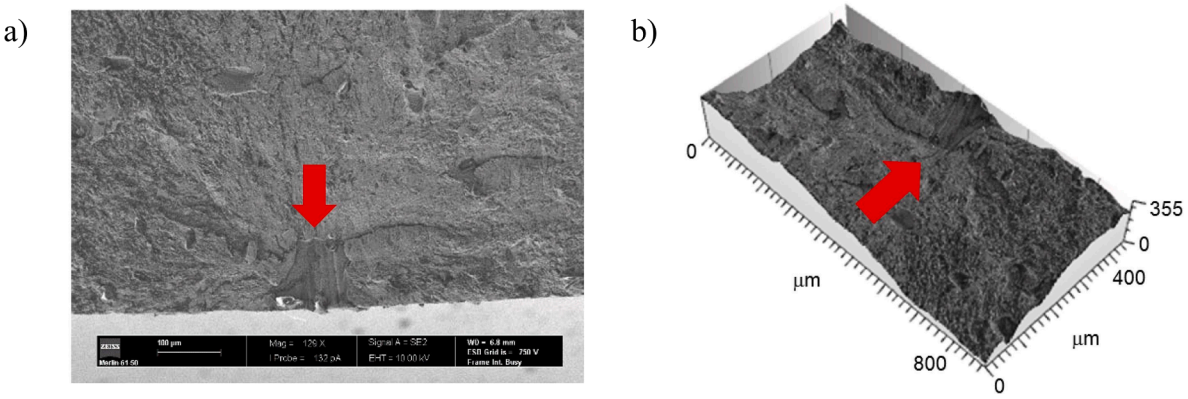

Fig. 10. a) Scanning electron microscopy (SEM) micrograph of the fracture surface of a notched AM 18Ni300 specimen and b) 3D reconstruction of crack initiation site showing the presence of an interlayer defect. Figure adapted from [187].

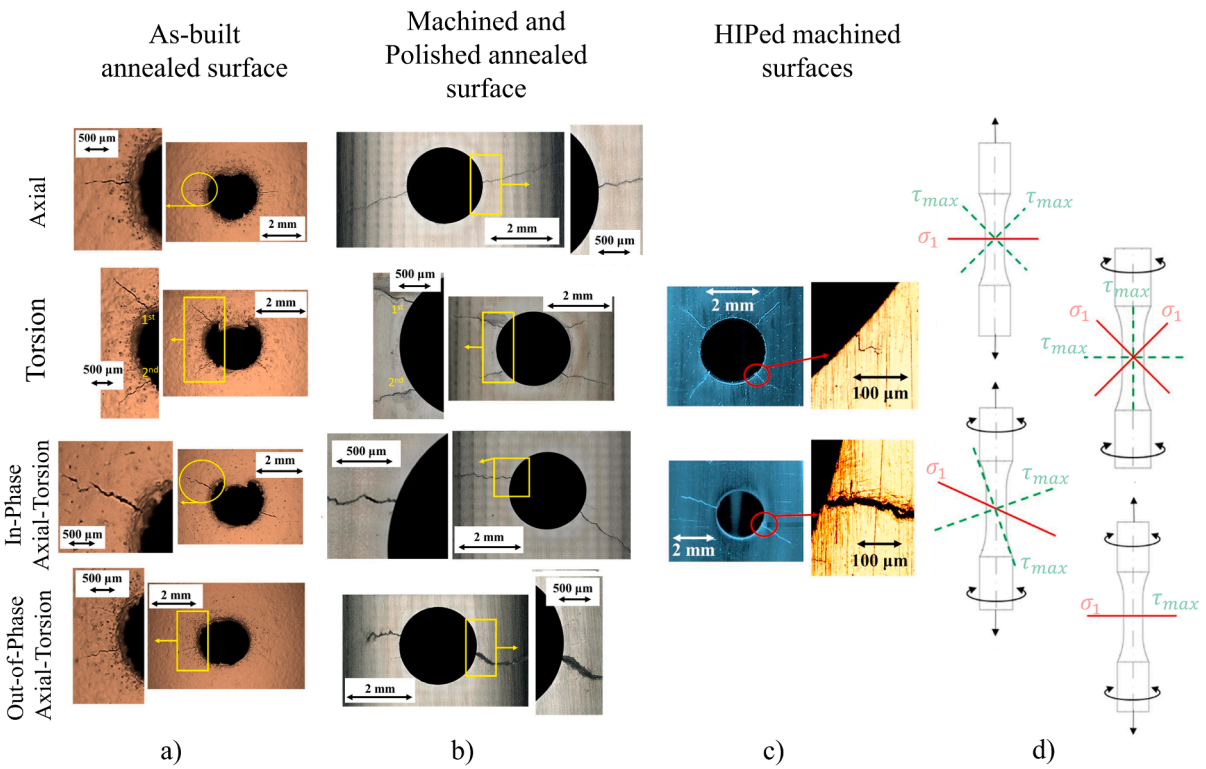

Fig. 11. Crack paths of notched LPBF Ti6Al4V specimens under different loading conditions for (a) as-built annealed surface, (b) machined and polished annealed surface, and (c) HIPed machined surface; d) maximum principal plane and maximum shear plane directions. Figure adapted from [208,223].

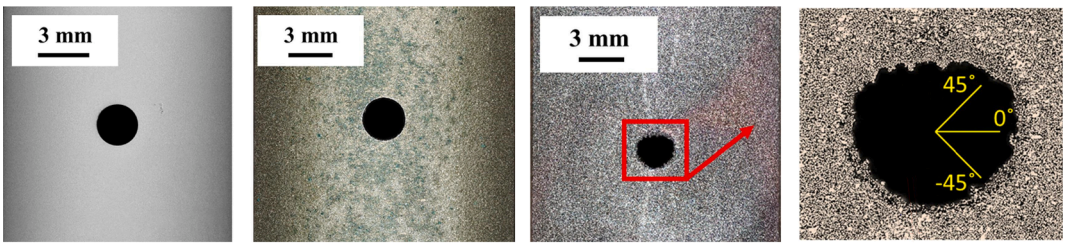

Fig. 12. Hole in thin-walled tubular specimen: a) machined by drilling in a wrought component; b) machined by drilling after AM process and left in the as-built state; c) built during the AM process; d) magnification of c). Figure adapted from [223].

the effect of the building direction on the fatigue performance of AM, several investigations can be found in the literature [93,149,151,193,208,212,226–230]; however, they mostly analyzed the uniaxial fatigue loading properties. In addition to the various surface roughnesses achieved depending on the building direction, other possible causes for the different fatigue performance achieved by changing the printing orientation may be found in irregularly shaped LOF defects, whose direction and morphology are affected by the building direction [149–154], and in the microstructure that determines anisotropic features [93,231,232]. Considering the process parameters to reduce the surface roughness and the amount of LOF defects, performing heat treatments to homogenize the microstructure [96] and machining the components [233] could represent effective solutions to reduce the influence of the build direction on the fatigue properties of AM components. However, the anisotropic behavior of AM materials can be considered as a variable in design and fabrication of mechanical components which can be taken advantage of in some applications.

3.2. Crack orientations

3.2.1. Surface conditions and load level effect on the failure mechanism

Crack growth mechanisms are typically studied under uniaxial loading and mode I crack growth. In real applications, components

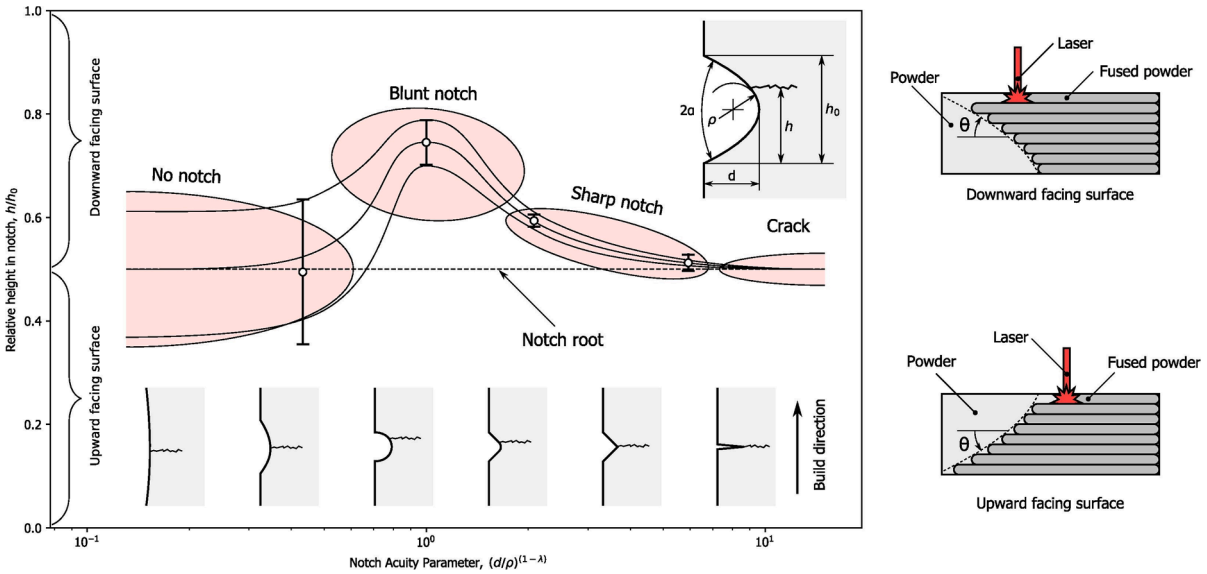

Fig. 13. Diagram relating failure initiation site in a notched region to the notch acuity. Figure adapted from [220].

usually experience multiaxial loads; consequently, cracks can also grow under mixed-mode conditions in various directions [128,164,208]. Indeed, studies on LPBF Ti-4Al-6 V and 17-4 PH specimens under multiaxial loading conditions [234] have shown that cracks can grow either in mode I and continue growing in mode I or in shear mode. The shear cracks can then change their direction and align with the maximum principal stress (MPS) plane as mode I cracks or grow in shear or mixed mode. In addition, crack growth behavior is also dependent on the stress ratio, whose value, if low, determines the significance of roughness-induced crack closure, and its influence can be detected in shear-driven failure and is affected by crack path, crack tip plasticity, and the extent of crack tip displacement in mode II and mode III, depending on the crack aspect ratio and specimen geometry [235].

In addition, the failure mechanisms of AM components may be different from those of their wrought counterparts, resulting in different fatigue crack orientations. By investigating the fatigue crack orientations under different loading conditions, Fatemi et al. [218] observed how the failure mechanisms of wrought and AM specimens could be different; while all failure cracks for the wrought material occurred on or near the orientation of the maximum shear plane (see Fig. 14a), crack orientations for both AM as-built annealed and machined annealed specimens were along the MPS plane, indicating a brittle behavior (see Fig. 14b and c) and suggesting that the surface conditions may not have a strong influence on the crack orientation for smooth AM components, even if possible influences cannot be excluded a priori. However, as-built annealed AM specimens and machined and polished annealed AM specimens are both characterized by a martensitic microstructure that remains after the annealing process (see Fig. 14f) and by the presence of large internal defects that determine the brittle behavior [208]. A different failure mechanism has indeed been found in AM machined HIPed specimens [169] (see Fig. 14d), which presented cracks oriented along the maximum shear planes, indicating a ductile behavior similar to that of the wrought material (see Fig. 14d in comparison with Fig. 14a). This can be attributed to the change in microstructure and defect characteristics determined by the HIP technique, which led to the transformation of the α-martensite structure to the ductile α-β phase (see Fig. 14g). It is also worth noting that different build orientations were considered for these specimens, but no significant difference was noticed in the failure mechanism.

However, the failure mechanism is not only dependent on the component microstructure. A change in the failure mechanism of AM Ti6Al4V was documented in [117,169,208] by changing the fatigue regime from low cycle fatigue (LCF), characterized by failure on the maximum shear planes involving plastic deformation, to high cycle fatigue (HCF), characterized by failure along the maximum principal plane indicating the dominance of internal defects (see Fig. 15a, b, and c). Renzo et al. [197,198,236] detected the same change in the failure mechanism of AM Ti6Al4V under in-phase axial-torsion loading (see Fig. 15d). Molaei et al. [153] documented different failure mechanisms with increasing applied stress levels for AM 17-4 PH stainless steel. Bressan et al. [237] investigated the fatigue behavior in the LCF regime of Ti6Al4V under multiaxial loading, detected higher plasticity and absorbed energy from the specimens in heat-treated conditions compared to their untreated counterparts, and observed that the hardening and softening curves depended on the heat treatment when dealing with the axial strain path and on the layering when dealing with the 90° out-of-phase strain path. This could also determine the change in the failure behavior of the specimens.

It is worth noting that, regardless of the building direction, in machined surface conditions, cracks do not always propagate along the weak build plane, as might be expected; indeed, Fig. 15b I shows specimens characterized by cracks both in the vertical and horizontal directions with the same build direction, while the specimens with different build directions shown in Fig. 15b III and c III present failure along the same direction. However, the possible influence of the surface defect networks in determining the crack orientation cannot be excluded when dealing with as-built surface conditions. Molaei et al. [208], documenting failure in as-built surface annealed Ti6Al4V under torsional loading, noticed that failures, even if in accordance with the assumed maximum shear

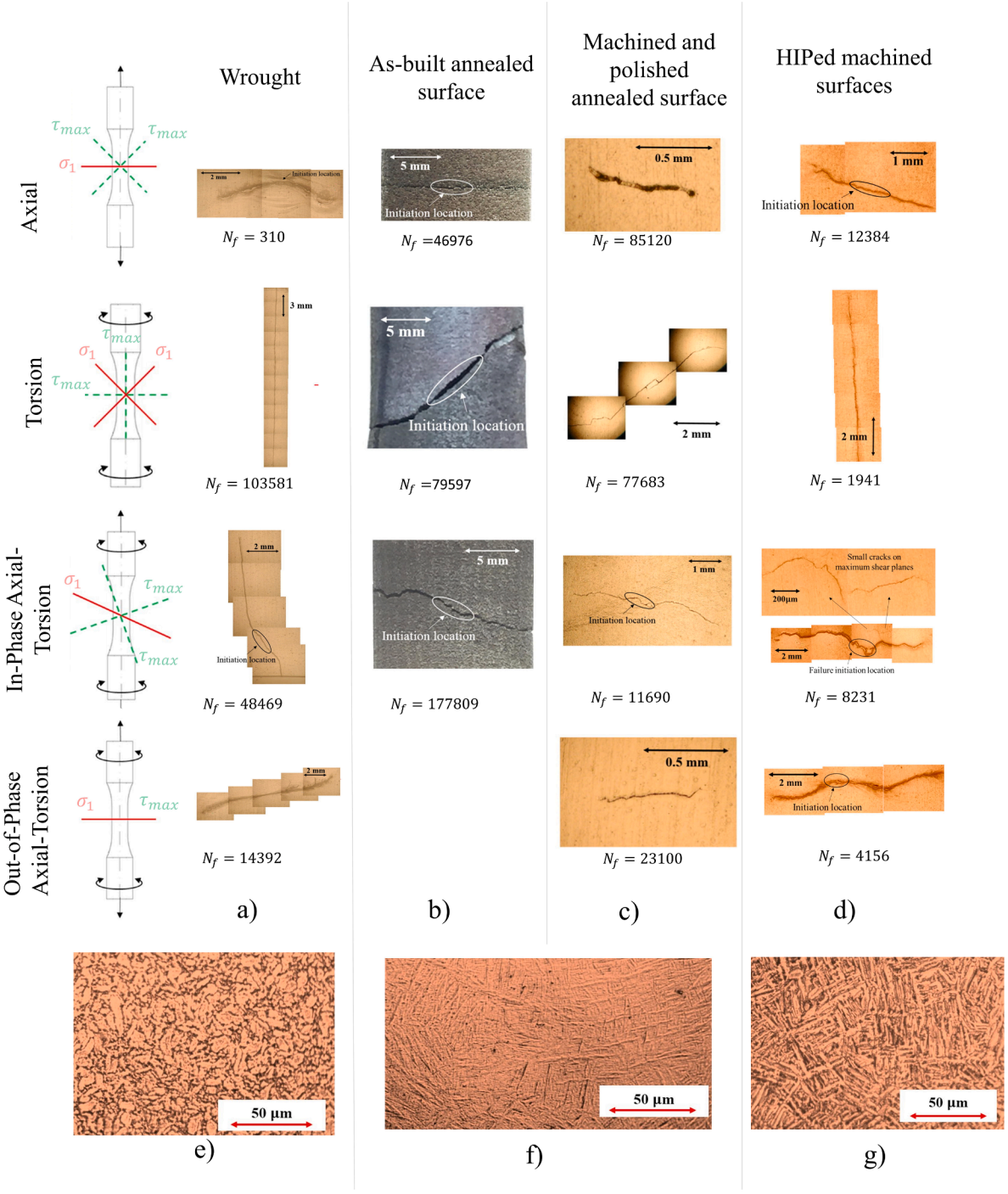

Fig. 14. Crack orientations for a) wrought and AM in b) as-built annealed, c) machined and polished annealed, and d) HIPed machined surface condition specimens under different loading conditions for Ti6Al4V; optical microscopy of etched: e) wrought material showing equiaxed α-β microstructure; f) AM annealed at 700 °C for 1 h condition showing martensite microstructure; g) AM HIPed at 920 °C and 100 MPa for 3 h condition showing elongated α grains embedded in α-β phase microstructure. The maximum principal plane and maximum shear plane directions are reported for each loading condition for a better interpretation of the failure mechanism. Figure adapted from [169,218].

stress mechanism of failure in the LCF regime, occurred only horizontally (see Fig. 15a I), while machined surface annealed specimens presented failures in both maximum shear planes at high loads as well as propagating cracks on both the maximum principal planes at low and medium loads (see Fig. 15b and c). Therefore, the influence of surface condition on the crack path cannot be excluded. Studies on AM as-built 17-4 PH specimens [153,208] provided further proof of the influence of these surface defect networks, as shown in

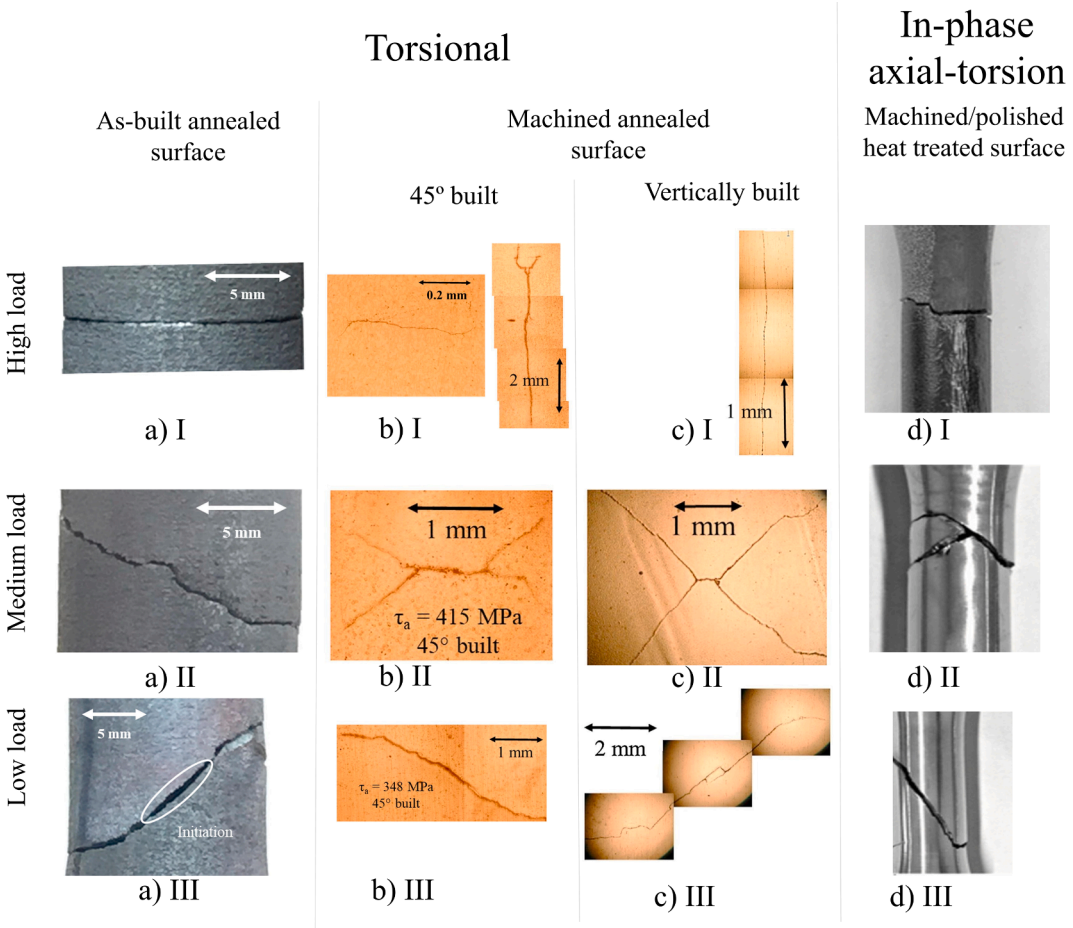

Fig. 15. Examples of crack orientations with changing load on AM Ti6Al4V specimens under torsional loading in a) as-built annealed, b) 45° built machined annealed surface, and c) vertically built machined annealed surface; d) in-phase axial-torsion loading in machined/polished heat-treated surface. Figure adapted from [169,198,208].

Fig. 16. Molaei et al. [153] demonstrated the influence of these fabrication defects through torsional fatigue tests performed with different degrees of superimposed static compressive stress perpendicular to the defect network to lower their influence on crack initiation and growth orientation.

The synergistic action of defects may also result in cracks with unexpected orientations. Fig. 17 shows two LOF defects that started propagating following different orientations (one growing according to mode I orientation and the other according to mode II) before coalescing and determining the dominant crack. Molaei et al. [208] studied the fatigue behavior of notched components and reported that secondary cracks can initiate and grow from the geometrical discontinuity after the first crack grows sufficiently long to affect the stress distribution around the notch.

Another aspect worth mentioning regarding the crack orientations under multiaxial fatigue loading is crack branching, i.e., the deviation of the crack orientation during its growth following other failure mechanisms, causing possible formation of multiple crack fronts.

Molaei et al. [208] documented this phenomenon by studying the fatigue behavior of AM 17-4 PH and Ti6Al4V. The comparisons between the dominantly shear- and axial-loaded specimens showed that, when axial loading was involved, the crack branched to mode I even if it initiated propagation in mode II, as can be seen in Fig. 18; similar observations have been reported by Renzo et al. [236]. The crack growth direction is then dependent on the applied shear and normal stresses on the crack plane [238], which reveals the importance of the friction- and roughness-induced crack closure effect in the crack growth process, with crack growth in mode II occurring if the driving force (shear mode deformation at the crack tip) is stronger than the friction of the crack surfaces [239]. This, in fact, is due to the increased plasticity at the crack tip, which could destroy the crack face asperities and, therefore, reinforce the effective mode II driving force and prevent branching to mode I. Different behaviors can be observed in wrought materials, such as crack branching due to crack face friction and roughness-induced closure effects. However, after the first branching, the crack may change its direction again owing to several factors, such as internal defects and interaction with other propagating cracks (see Fig. 17).

Crack branching is also influenced by the fatigue regime; indeed, cracks have been seen to propagate longer in mode II before

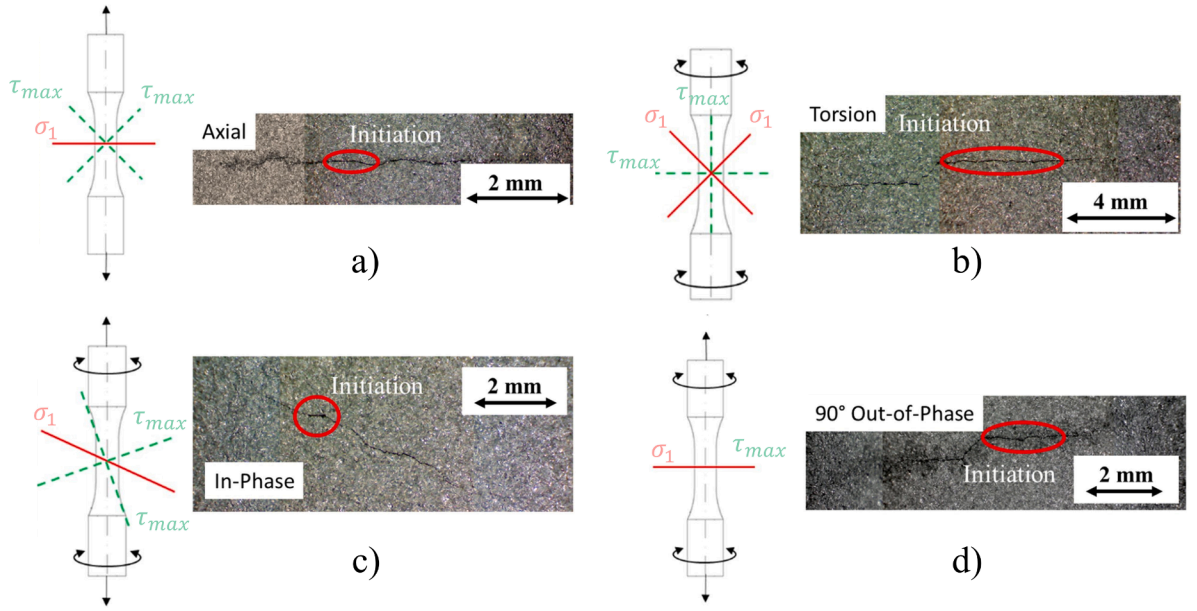

Fig. 16. Effect of multiple circumferentially connected defect networks on failure crack initiation and growth orientation of LPBF as-built surface CA H1025 heat-treated 17-4 PH alloy under a) axial, b) torsional, c) in-phase axial-torsion and d) 90° out-of-phase loading conditions. The maximum principal plane and maximum shear plane directions are reported for each loading condition for a better interpretation of the failure mechanism. Figure adapted from [153].

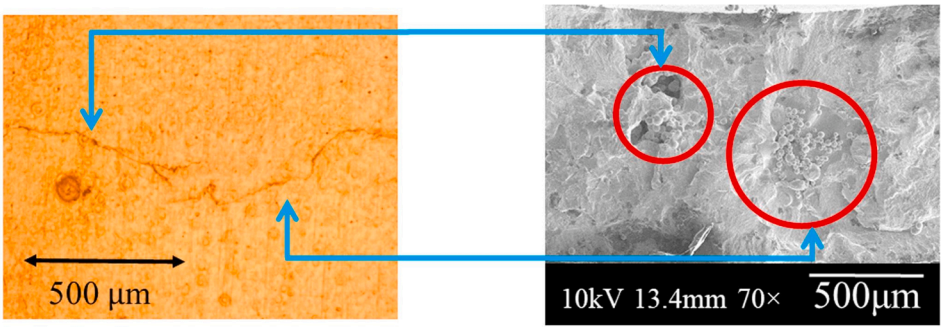

Fig. 17. Uncommon crack orientation determined by the synergistic action of two LOF defects under in-phase axial-torsion loading; one defect is following mode I orientation while the other presents mode II orientation. Figure adapted from [208].

branching with increasing loading levels, as can be observed from Fig. 15b and c. Gates and Fatemi [240] explained the same behavior for wrought 2024-T3 aluminum alloy, arguing that increasing the loading level leads to an increase in the effective shear-mode driving force owing to the combined effect of friction and roughness. As shown in the figure, this could cause the crack to initiate and grow primarily in mode I as the load level decreases.

3.2.2. Notch effect on crack orientation

Another factor that can influence the orientation of fatigue cracks is the presence of geometrical discontinuity, which is inevitable in AM components. Molaei et al. [208] investigated the fatigue behavior of notched specimens of machined and HIPed Ti6Al4V and both as-built and machined heat-treated 17-4 PH under multiaxial loading conditions. The failure mechanisms were found to be in accordance with what was previously observed for unnotched specimens; the machined surface condition resulted in mode II growth regardless of the nominally applied loading condition, while the as-built surface conditions were characterized by crack growth in mode I, owing to the additional friction determined by the rough surface and unmelted particles affecting the closure mechanism, as shown in Fig. 11.

An interesting aspect is represented by the crack branching determined by the stress gradient caused by the geometrical discontinuity. Although shear-mode crack initiation has been observed for machined surface specimens, when the crack grows in the lower stressed regions of the notched components, the frictional effects lead to a transition into mode I growth [223]. This behavior is consistent not only with that observed by Gates and Fatemi [241] for wrought 2024-T3 aluminum alloy, but also with the observed

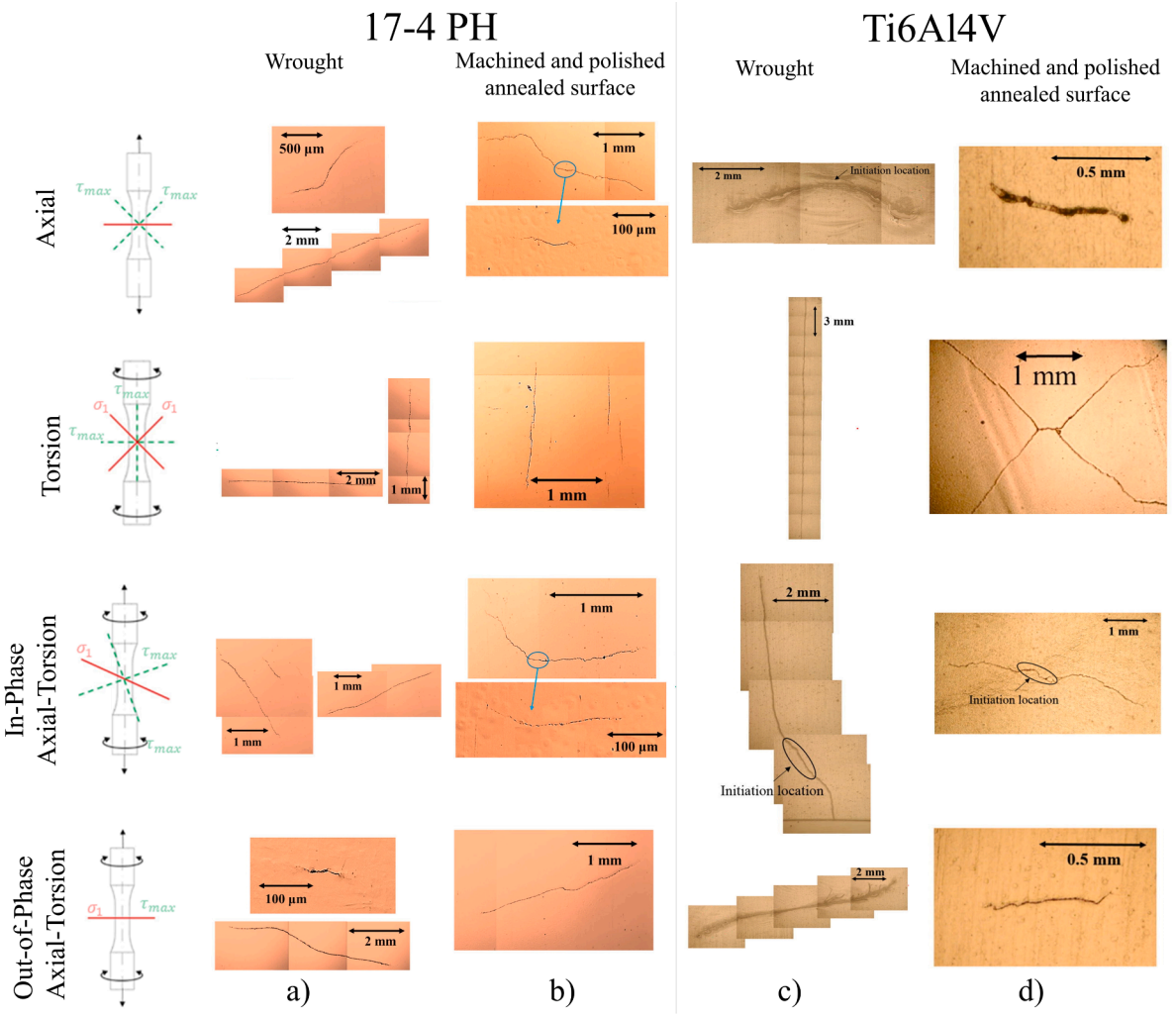

Fig. 18. Failure crack paths showing branching for a) wrought and b) AM machined surface 17-4 PH and c) wrought and d) AM machined surface Ti6Al4V specimens under different loading conditions; solid red lines indicate maximum principal plane orientations, dashed green lines represent maximum shear plane directions, and dashed black lines indicate Fatemi–Socie (FS) critical plane orientations. The maximum principal plane and maximum shear plane directions are reported for each loading conditions for a better interpretation of the failure mechanism. Figure adapted from [208].

dependence of the crack path on the load level for the unnotched specimens, where the crack branches to mode I after initiation in mode II as the applied stress level decreases.

4. Fatigue life prediction methodologies

Despite the undeniable need for research that qualitatively assesses the effects of different parameters on the fatigue performances of AM components, without suitable tools to quantitatively define the effects of different parameters, AM components will lack structural and fatigue reliability; as a consequence, real applications of AM cannot be expected to flourish, resulting in significant limitations in the advancement of this technology.

To date, only a few multiaxial fatigue assessment methodologies have been applied to assess the fatigue life of AM components that account for both the defects and surface conditions. In the following sections, the principal life prediction methodologies applied for the fatigue damage assessment of AM components under multiaxial fatigue loading are presented, with a particular focus on their accuracy in correlating fatigue data obtained under different loading conditions.

4.1. Von Mises and maximum principal stress (MPS) criteria

Fatemi et al. [199,218] studied the fatigue behavior of wrought, as-built AM, and machined AM thin-walled tubular Ti6Al4V

specimens, considering axial, torsional, in-phase axial-torsion, and 90° out-of-phase axial-torsion loads. The data were summarized using both the von Mises equivalent stress amplitude and MPS amplitude (see Fig. 19).

Although the von Mises criterion showed good correlation in the axial, torsional, and combined in-phase axial-torsion fatigue data, poor data correlation was achieved when dealing with the 90° out-of-phase tests. Similar conclusions were reached by Molaei et al. [153], who studied the multiaxial fatigue behavior of AM 17-4 PH.

Better correlations between the data were observed through the application of MPS criterion. The reason behind the poor performance of the von Mises criterion can be found in the behavior of the material; indeed, the von Mises equivalent stress performs well in dealing with the proportional stress states of ductile materials; however, the AM specimens showed brittle behavior, for which the MPS criterion is more suitable [242].

However, both methods failed to correlate the out-of-phase axial-torsion fatigue data. Considering that the real loading conditions affecting a component are often characterized by non-proportional variable amplitude multiaxial stress states, these methods are limited in practical applications.

Fig. 19 reports the fatigue test data considered by Fatemi et al. [218] summarized through these two criteria for comparison in both machined and as-built conditions.

4.2. Critical plane approach

The critical plane approach, which is well known in the literature and has been applied with various methodologies [243–254], uses the basic material fatigue properties to determine the failure orientation [255–257] and crack initiation life. In AM components, the fatigue properties used to apply the critical plane approach are obtained from specimens produced with the same process parameters that should result in a statistically similar distribution of defects. Following this procedure, the effect of defects is indirectly considered; however, it is worth highlighting that such a procedure does not explicitly consider the effect of some parameters on the surface roughness and defect distribution, such as the surface orientation, component size, and component geometry (see Section 3.1).

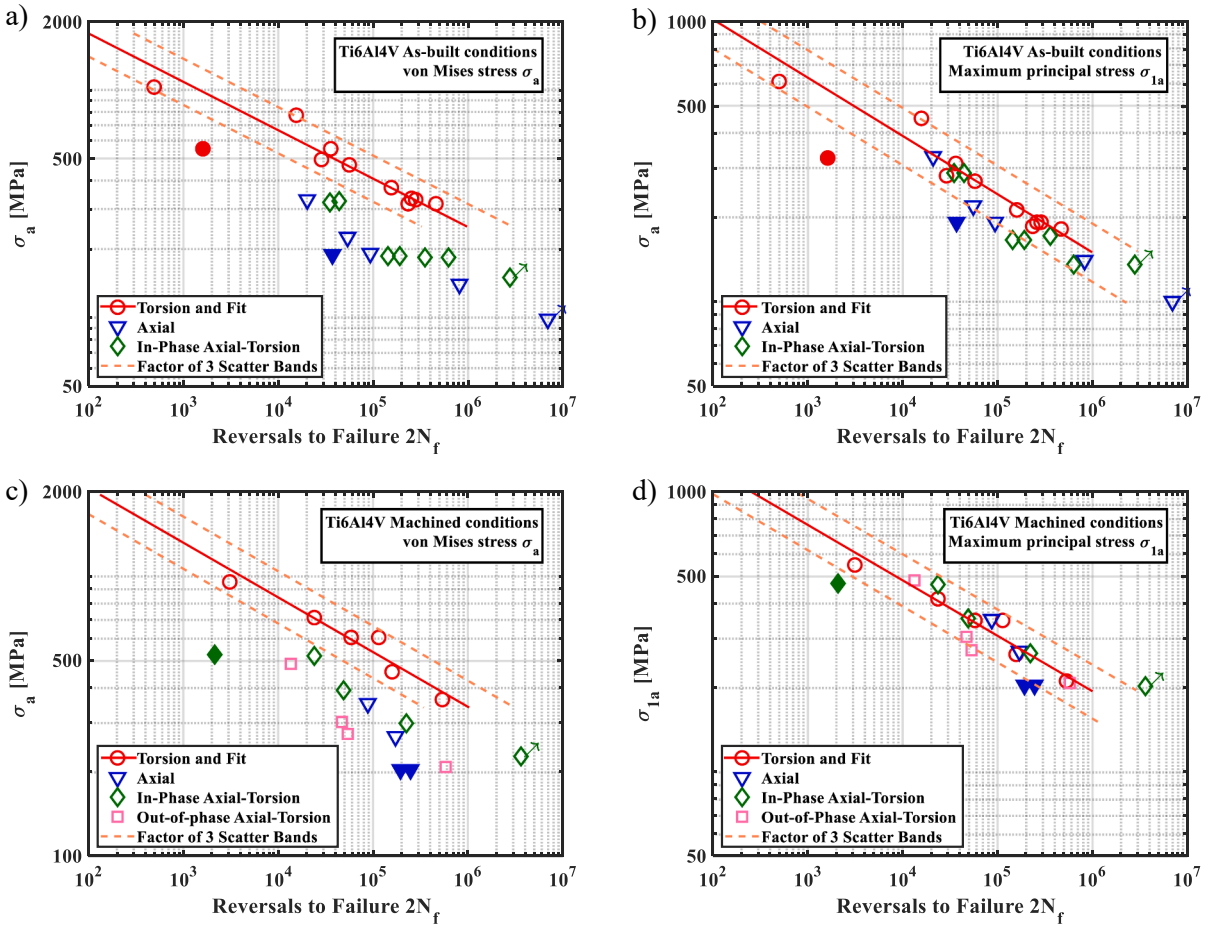

Fig. 19. Correlation of fatigue data obtained for Ti6Al4V specimens based on: (a) von Mises equivalent stress amplitude in as-built conditions; (b) MPS amplitude in as-built conditions; (c) von Mises equivalent stress amplitude in machined conditions; (d) MPS amplitude in machined conditions. Figure adapted from [218].

The critical plane approach consists of several steps. The first step includes the determination of the nominal or local stress/strain, depending on the geometrical features of the component. The stresses are then projected in the shear and normal components onto different plane orientations. Damage is then computed for each plane using the selected damage parameter. Damage values on each plane are then used to evaluate the expected fatigue life of the component using a damage accumulation rule.

Different damage parameters are available depending on the failure mechanism; there are both tensile-based critical plane parameters for the tensile failure mechanism, such as the Smith–Watson–Topper (SWT) typical in the HCF regime [167] and shear-based critical plane parameters, such as the Fatemi–Socie (FS), for the shear failure mechanism.

The SWT parameter can be evaluated through [258]:

$$\sigma_{1,\max}\left(\frac{\Delta\varepsilon_1}{2}\right)=\frac{\left(\sigma_f^{'}\right)^2}{E}\left(2N_f\right)^{2b}+\sigma_f^{'}\varepsilon_f^{'}\left(2N_f\right)^{b+c} \tag{1}$$

where $\sigma_{1,\max}$ denotes the maximum stress on the maximum principal strain range plane, $\Delta\varepsilon_1$ denotes the maximum principal strain range, $\sigma_f^{'}$ denotes fatigue strength coefficient, $\varepsilon_f^{'}$ denotes fatigue ductility coefficient, $2N_f$ denotes reversals to failure, b denotes fatigue strength exponent, c denotes fatigue ductility exponent and E denotes Young's modulus.

However, it must be highlighted that a proper choice for the fatigue failure criteria cannot neglect consideration of the failure mechanisms; indeed, with the aim to prove the poor data correlation that can result by not properly considering the failure mechanism, Molaei et al. [153]applied the critical plane approach using the SWT parameter to correlate the fatigue data of as-built surface heat-treated 17-4 PH but this criterion did not result in an acceptable fatigue data correlation. In any case, the poor data correlation shown for the dataset considered in [153] is due to the shear failure mechanism, while good correlation with SWT parameter may be expected when the SWT parameter is used for tensile failure mechanism.

The FS parameter can be evaluated through:

$$\frac{\Delta\gamma_{\max}}{2}\left(1+k\frac{\sigma_{n,\max}}{\sigma_y}\right)=\frac{\tau_f^{'}}{G}\left(2N_f\right)^{b_0}+\gamma_f^{'}\left(2N_f\right)^{c_0} \tag{2}$$

where $\Delta\gamma_{max}$ is the maximum shear strain range experienced on any plane, $\sigma_{n,max}$ is the maximum normal stress occurring on the same plane, σ_y is material yield strength, $\tau_f^{'}$ is shear fatigue strength coefficient, $\gamma_f^{'}$ is shear fatigue ductility coefficient, b_0 is shear fatigue strength exponent, c_0 is shear fatigue ductility exponent, G is shear modulus, $2N_f$ is reversals to failure and k is a material-dependent parameter that reflects the influence of normal stress on fatigue damage.

Molaei et al. [208] applied the FS critical plane parameter, suitable for ductile behavior or shear failure mechanism materials, to summarize the fatigue data of AM machined HIPed Ti6Al4V material under different loading conditions considering the fatigue life assessment method and pure torsion strain-life properties, as seen in Fig. 20a; Molaei and Fatemi [169] also considered the FS critical plane parameter to correlate AM machined heat-treated 17-4 PH specimens under various multiaxial loading conditions, as seen in Fig. 20b.

A modified form of the FS parameter (see Eq. (2)), proposed by Gates and Fatemi [259], has been shown to capture the transition of the failure mechanism from shear in the LCF to tensile in the HCF [117,153,208,260] and to better account for the mean tensile stress effects [259]. The modified FS parameter can be evaluated as follows:

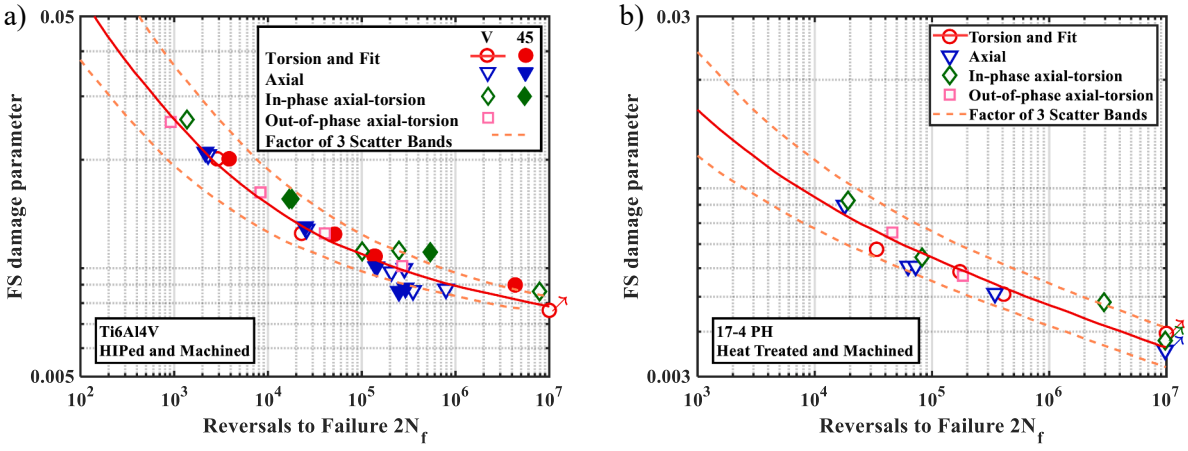

Fig. 20. Correlation of fatigue data through the FS damage parameter criterion of a) AM machined surface heat-treated 17-4 PH stainless steel alloy and b) AM machined surface HIPed Ti6Al4V alloy. Figure adapted from [169,208].

$$\frac{\Delta\gamma_{\max}}{2}\left(1+k\frac{\sigma_{n,\max}}{G\Delta\gamma}\right)=\frac{\tau_f'}{G}(2N_f)^{b_0}+\gamma_f'(2N_f)^{c_0} \tag{3}$$

The only difference from the FS parameter in Eq. (2) is that σ_y has been replaced with $G\Delta\gamma$ to normalize the normal stress term where $\Delta\gamma$ is the shear strain range.

Molaei et al. [153] applied the modified FS critical plane parameter for both machined and as-built conditions of AM 17-4 PH material under different loading conditions, and the summary is shown in Fig. 21a; additionally, Molaei et al. [117] considered both machined and as-built AM Ti6Al4V under different loading conditions, as seen in Fig. 21b. Difficulties in correlating the torsional fatigue data have been reported by Molaei et al. [153] for as-built AM 17-4 PH material that showed premature failures in the short-life regime, which was attributed to the effect of surface defect networks.

Fatemi et al. [117] and Molaei et al. [225] investigated, through the FS critical plane approach, the multiaxial fatigue behavior of notched AM Ti6Al4V and 17-4 PH under different surface conditions. In notched fatigue, the stress gradient induced by the geometrical discontinuity needs to be properly accounted for; in this regard, in [117,225], the FS critical plane approach was applied, using the theory of critical distances (TCD) [261–264] considering as critical distance, i.e., a material characteristic length, the largest observed defect length for each of the conditions studied, as shown in Fig. 22f; similar works can be found in the literature [265–270]. As can be seen in Fig. 22, the combination of the two approaches allows for an accurate multiaxial fatigue data correlation, within a scatter band of ±3, with the exception of the notched as-built Ti6Al4V specimens under torsional loading reported in Fig. 22e; this is attributed to the stair-stepping effect at the notch that resulted in lower fatigue performance due to higher-than-expected stress concentrations.

Fatigue performance under variable amplitude loading conditions was investigated by Molaei and Fatemi [167] with both notched and unnotched AM specimens tests for both Ti6Al4V alloy and 17-4 PH stainless steel. The authors applied a multiaxial cycle counting method [271,272] to decompose the load history in equivalent constant-amplitude loading. Fig. 23 shows the predictions of the critical plane approach applied to the Ti6Al4V and 17-4 PH alloys specimens. As can be seen, nearly all the data fall within the scatter bands of 1/3 and 3. The conservativisms shown by the machined samples are explained in Section 3.1.

4.3. Fracture mechanics approach

The metal fatigue damage process mainly involves nucleation and growth of microcracks up to a length of about a few grains on the order of one or two hundred microns, followed by small crack growth (typically less than 2 mm) [260], then long crack growth (>2 mm).

Because defects are present in the AM parts, the first step of crack nucleation may be non-existent. Therefore, the fatigue life may only consist of the small and long crack growth processes. Considering the significance of defects in controlling the fatigue behavior of AM metals, methods that explicitly consider their influence are of high interest in damage-tolerant design applications.

The use of fracture mechanics (FM)-based parameters, such as the stress intensity factor (SIF), which can explicitly consider defects, could represent a valid tool to assess their fatigue behavior, as already proven for AM components under uniaxial loading [195,234]. Several approaches can be considered to correlate uniaxial and multiaxial fatigue data based on crack growth properties; however, an appropriate approach must be chosen by considering the fatigue damage behavior to be assessed by the observation of typical fracture surfaces. In any case, the application of these approaches may be demanding, and for some applications, simpler approaches may lead to advantages in terms of time and computational costs.

The determination of crack growth properties may also require additional effort and financial resources to be acquired, and it is possible to find these properties for various AM metals [117,179,273,274] evaluated through standardized specimens, but they are mostly limited to mode I crack growth, and there is still a lack of crack growth properties for cracks starting from naturally occurring AM defects. In addition, it is worth highlighting how the mechanical properties of AM components are related to several parameters involved in their realization process, as presented in the previous sections. The common practice for dealing with the multiaxial fatigue assessment of AM components through the FM approach [116,167,200,225,234,275] is to consider mode I crack growth properties

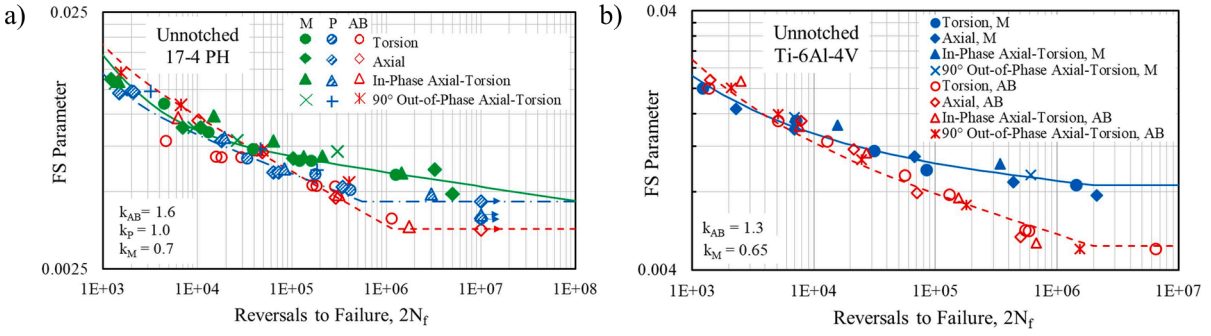

Fig. 21. Unnotched multiaxial constant amplitude fatigue data correlations based on modified FS damage parameter for LPBF; a) as-built (AB) and polished (P) surface not-HIPed, and machined (M) surface HIPed 17-4 PH [153] alloys and b) as-built (AB) surface and machined (M) surface Ti6Al4V [117]. Diagrams taken from [167].

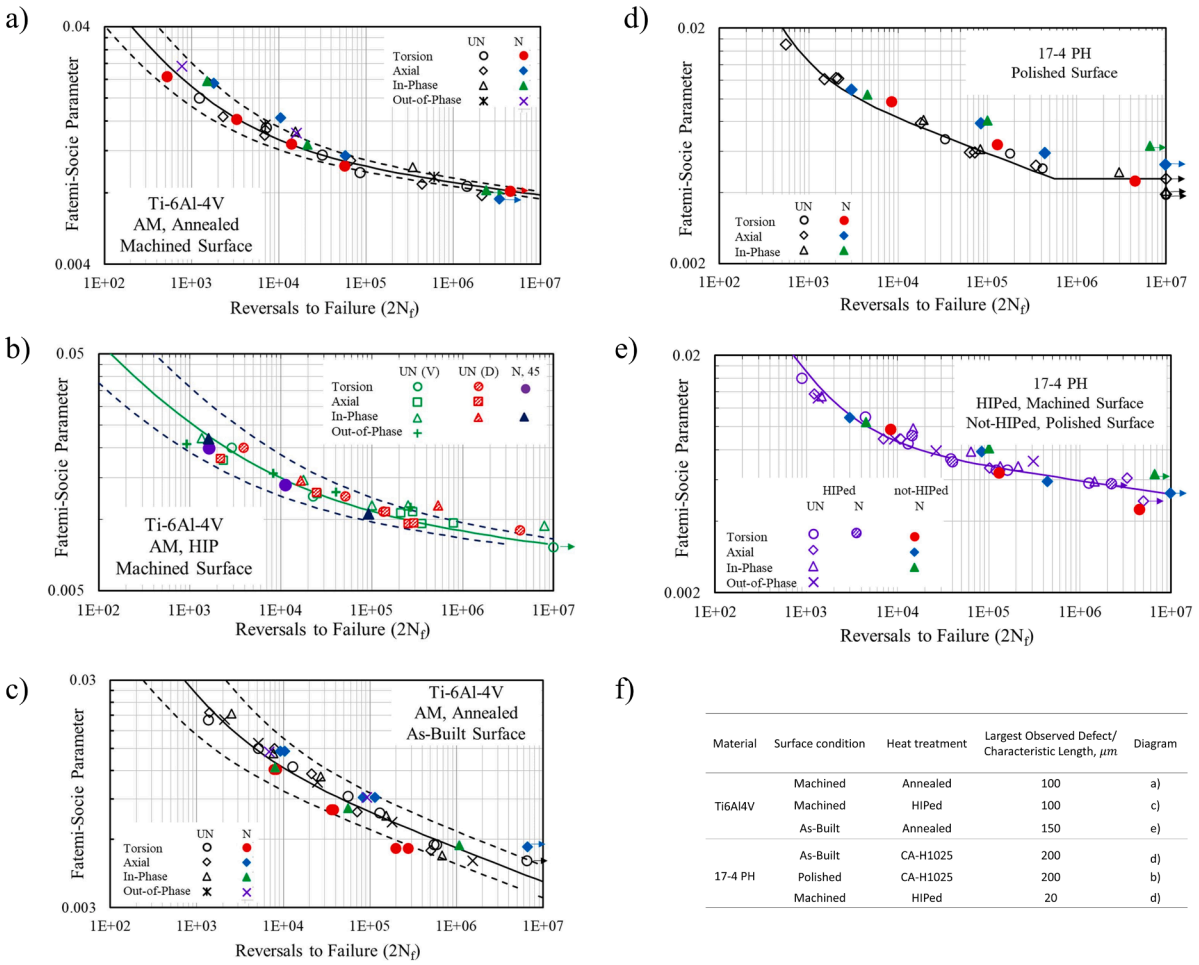

Material	Surface condition	Heat treatment	Largest Observed Defect/ Characteristic Length, μm	Diagram
Ti6Al4V	Machined	Annealed	100	a)
	Machined	HIPed	100	c)
	As-Built	Annealed	150	e)
17-4 PH	As-Built	CA-H1025	200	d)
	Polished	CA-H1025	200	b)
	Machined	HIPed	20	d)

Fig. 22. Multiaxial notched (N) and unnotched (UN) fatigue data correlation based on FS damage parameter of: Ti6Al4V specimens with a) machined surface annealed, b) machined surface HIPed, and c) as-built surface annealed conditions; 17-4 PH specimens with d) polished surface and e) HIPed machined surface and not-HIPed polished surface; f) largest observed defect size for different material and surface conditions used in the application of the TCD theory; (D) and (V) are related to the building direction and stand for diagonally and vertically, respectively. Dashed lines indicate the factors of 1/3 and 3 scatter bands. Figure adapted from [225].

obtained from previous studies (and thus generally related to other process parameters) and assume them to be a reasonable estimation for the properties of the components analyzed, as long as the microstructure is similar.

Some considerations must be made regarding the crack-growth properties to better understand their influence on the estimated fatigue life. Indeed, the fracture toughness value has been shown to have a small influence on the fatigue life predictions [234], even if the fracture toughness is highly dependent on the AM process variations; similar effects on the fatigue life predictions have been documented for the final crack length at failure [200]. The threshold value is dependent on the nominal load ratio, but its value at $R = 0.1$ represents a conservative lower bound estimate for $R = -1$ if the entire stress range is considered [276]. Another parameter that significantly affects the predicted fatigue life is the initial assumed crack length [234].

Regarding the mixed-mode fatigue properties, when dealing with conventionally manufactured components, the stress intensity threshold derived for mode I has already been shown by Campbell and Ritchie [277] to represent a conservative lower bound estimate for the mixed-mode fatigue crack growth threshold, and similar conservative considerations have been performed for AM components [116,167,200,225,234,275].

An equivalent SIF range ΔK_{eq} can also be considered when dealing with mixed-mode crack growth conditions by adding individual energy release rates. For a planar crack under plane stress conditions, this leads to the following equation [242]:

$$\Delta K_{eq} = \left[\Delta K_I^2 + \Delta K_{II}^2 + (1+\nu)\Delta K_{III}^2\right]^{0.5} \tag{4}$$

where ΔK_i is the mode-i stress intensity factor and υ is the Poisson ratio. However, the evaluation of ΔK_{eq} can be simplified depending on the failure mechanism observed; indeed, when the tensile failure mode is dominant, ΔK_{eq} is assumed to be equal to ΔK_I, as ΔK_{II} and ΔK_{III} would be negligible, and the MPS can be considered as an equivalent stress to directly evaluate ΔK_{eq} [275]; when in-plane shear

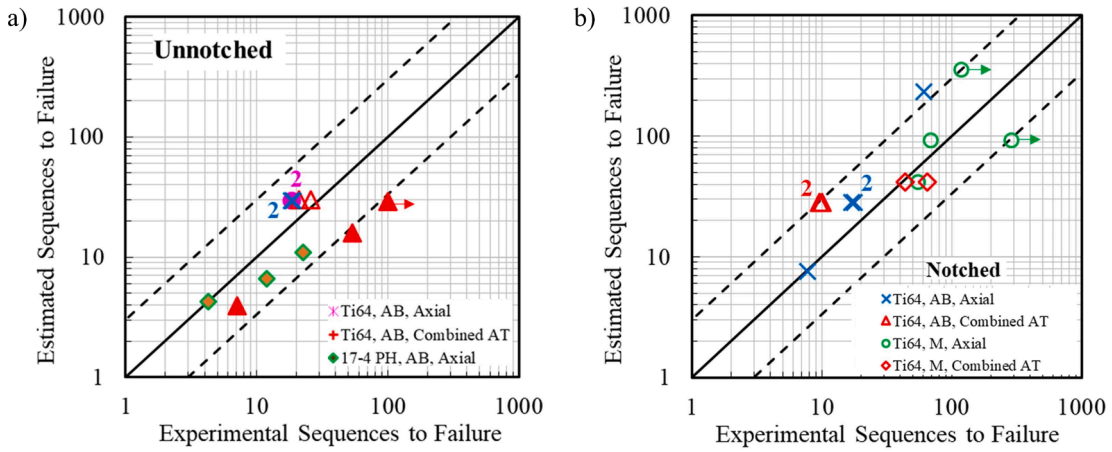

Fig. 23. Experimental vs predicted (through FS critical plane approach) fatigue life under variable amplitude fatigue loadings for a) unnotched Ti6Al4V and 17-4 PH in as-built conditions and b) notched Ti6Al4V in different surface conditions; Dashed lines indicate the factors of 1/3 and 3 scatter bands. Figure adapted from [167].

failure is dominant, ΔK_{eq} is assumed to be equal to ΔK_{II}, as ΔK_I and ΔK_{III} would be negligible [275], and the possibility of evaluating ΔK_{II} can also be through the FS critical plane parameter extended in the form of a shear-based SIF range according to [278,279]:

$$\Delta K_{II} = G\Delta\gamma_{\max}\left(1+\frac{k\sigma_{n,\max}}{G\Delta\gamma}\right)\sqrt{\pi a} = 2G(FS)\sqrt{\pi a} \tag{5}$$

where the parameters are those used in Eq. (3), as explained in Section 4.2 and a represents crack depth (see Fig. 25b).

When dealing with shear failure, an important aspect to consider is the roughness-induced crack closure, which is dependent on the crack path, crack tip plasticity, and crack tip displacement in mode II [275], and the combined effect of friction and roughness plays a key role in determining the crack path by reducing the effective shear-mode driving force, especially at lower loading levels. This aspect has already been discussed in Section 3.2 dealing with crack orientations; a critical level, referred to as either a mode II threshold or a point at which the potential for mode I growth exceeds that of the shear-mode crack, can be determined to explain the observed crack branching. This phenomenon has been extensively studied by Gates and Fatemi [240]. They proposed a model considering the reduction in the effective mode II SIF due to crack face interaction effects based on the average effective crack asperity angle and the sliding coefficient of friction, μ, which represents the friction between opposing crack faces under ideal contact conditions; through this model, the effective stress values and SIFs can be determined.

At this time, the application of FM-based models for the fatigue life prediction of AM metals under multiaxial loading is still limited to a few contributions: Zhang and Fatemi [200] predicted the fatigue life for as-built surface tubular Ti6Al4V specimens tested under axial, torsional, and in-phase axial-torsion loading conditions; Molaei and Fatemi [167] studied the fatigue performance of Ti6Al4V and 17-4 PH under variable amplitude service loading conditions; Molaei et al. [225] analyzed notched uniaxial and multiaxial fatigue behavior of AM Ti6Al4V and 17-4 PH stainless steel under different fabrication heat treatments and surface roughness conditions following the same procedure of Molaei and Fatemi [167]; Sanaei and Fatemi [275] investigated the fatigue behavior of AM Ti6Al4V and 17-4 PH under multiaxial loading conditions; Molaei et al. [116] analyzed the fatigue behavior of AM Ti6Al4V under multiaxial loading conditions.

4.3.1. Considerations regarding surface roughness and defects modeling

To explicitly consider the defects inside the component, assumptions must be made regarding the initial defect size, location, and shape; these features can significantly affect the performance of these approaches in estimating the fatigue life. Therefore, the proper application of these approaches for design purposes cannot neglect statistical analysis to describe the defect features. In this regard, considering the average defect size as the representative defect size for all specimens in one batch showed good performance in correlating the experimental fatigue results [188,280] demonstrating the validity of these approaches for design purposes. On the other hand, when dealing with a real component, in some cases, the defect features can be determined through techniques such as 3D X-ray computer tomography [152] and the FM approaches can be applied considering the actual defects in the component for monitoring purposes. In this regard, Sanaei and Fatemi [188] applied the FM approach considering the initial size of the defect that acts as a failure initiation site.

One major issue is determining the size and shape of the defects; indeed, various defect morphologies can appear in AM components, as shown in Fig. 4. A feasible way to account for the size of the initial defect was proposed by Murakami [281] using the square root of the area ($\sqrt{area}$) method. According to this method, the defect area is defined as the effective area of a smooth contour projected perpendicular to the loading direction that circumscribes the irregularly shaped defect, as shown in Fig. 24b. This approach is based on experimental evidence showing that irregularly shaped defects also grow, driven by the SIF, toward a round shape [116,234], as can be

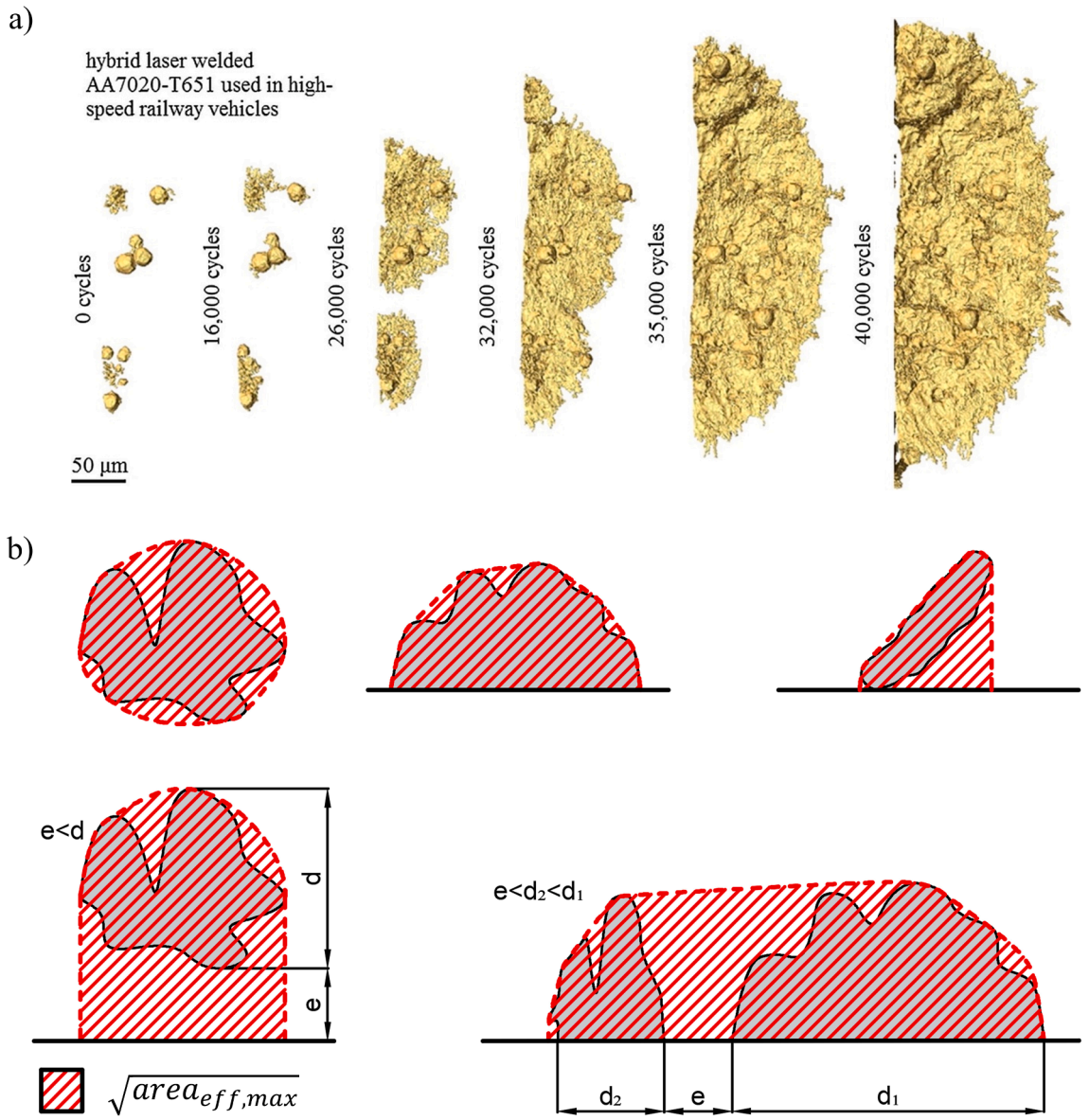

Fig. 24. a) Synchrotron radiation computed laminographic (SR-µ CT) observation of fatigue crack evolution from multiple surface-breaking pores to semi-elliptical surface crack; b) effective size of irregularly shaped defects according to the Murakami $\sqrt{\text{area}}$ method. Figure adapted from [281,282].

seen in Fig. 24a.

The main characteristics of a defect are its size, i.e., length, area, or volume, depending on the application, and shape, represented by the defect aspect ratio.

The most detrimental defects in AM components are usually at or near the component surface, especially when the component is left in the as-built condition [117,153,199,218] and the synergistic effects of surface roughness and subsurface defects should be considered. It is worth highlighting that the spherical powder particles fused on the surface of the as-built AM specimens do not carry load or act as significant stress raisers [153,276]. Consequently, only the valley part of the surface profile was considered as a crack in [200,209,211]. To deal with surface roughness and subsurface defects, an equivalent semi-elliptical surface crack can be assumed. The aspect ratio of this surface crack can, however, affect the predictions from the FM approach. Sanaei and Fatemi [234], assuming a constant aspect ratio of the crack throughout the growth life, and reported a difference of approximately 30 % when changing the aspect ratio from 1 to 0.5. In this regard, in [116,167] the assumed initial crack and aspect ratios were based on observations of the component fracture surfaces, reporting good agreement between the experimental and predicted fatigue life. The size of the initial crack length can be established using Murakami's method [283,284] which allows the determination of an effective initial crack size, $\sqrt{area_{\text{eff},max}}$, defined as:

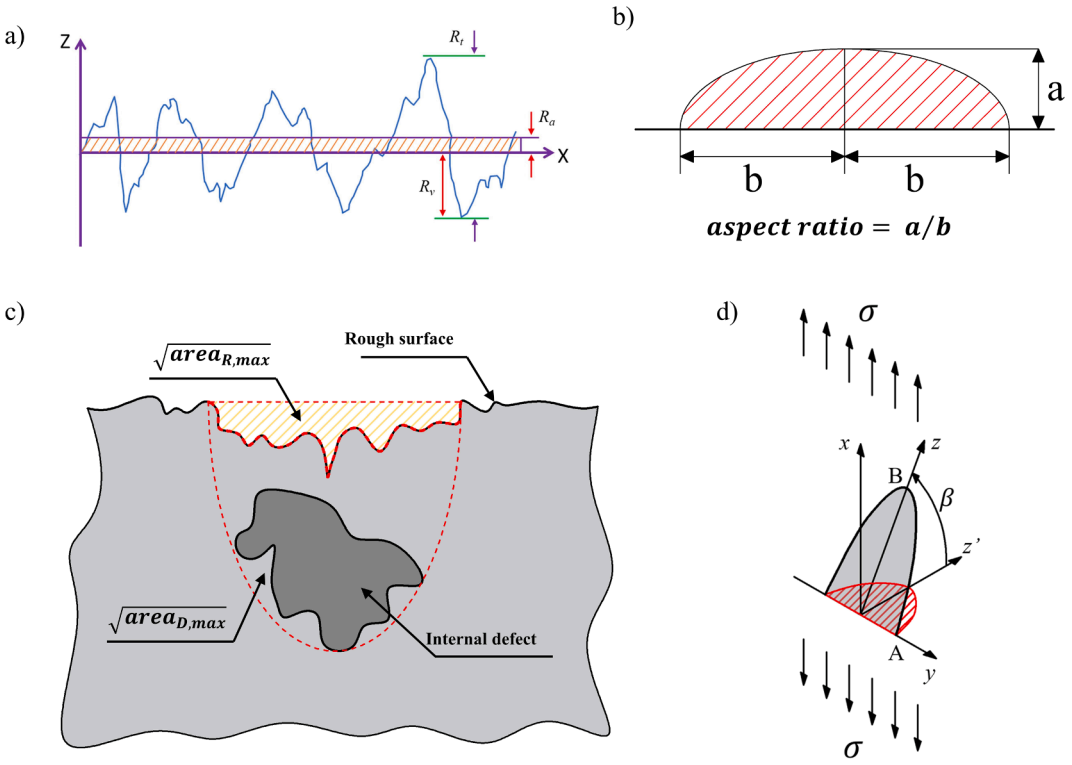

Fig. 25. a) Surface roughness parameters (figure from [153]); b) definition of the aspect ratio; c) equivalent defect size given by the combination of the maximum prospective equivalent surface defect determined from the surface roughness profile ($\sqrt{\text{area}_{R,\max}}$) and the maximum prospective internal defect size ($\sqrt{\text{area}_{D,\max}}$); d) inclined semi-elliptical surface crack.

$$\sqrt{area_{eff,\max}} = \sqrt{area_{D,\max}} + \sqrt{area_{R,\max}} \tag{6}$$

where $\sqrt{area_{D,max}}$ is the maximum prospective internal defect size and $\sqrt{area_{R,max}}$ is the maximum prospective equivalent surface defect size obtained from the surface roughness profile, as shown in Fig. 25c.

The $\sqrt{area_{R,max}}$ term, as explained in [116], is evaluated from the roughness profile acquired through stylus surface profilometry and assuming the surface roughness to be equivalent to periodic notches with notch depth a and notch pitch $2b$, according to the following equation:

$$\frac{\sqrt{area_{R,\max}}}{2b} \cong 2.97\left(\frac{a}{2b}\right) - 3.51\left(\frac{a}{2b}\right)^2 - 9.74\left(\frac{a}{2b}\right)^3 for\left(\frac{a}{2b}\right) < 0.195 \tag{7}$$

$$\frac{\sqrt{area_{R,\max}}}{2b} \cong 0.38 for \frac{a}{2b} > 0.195 \tag{8}$$

The terms a and b are determined through surface roughness parameters. A possibility considered by Sanaei and Fatemi [275] is to assume $a = R_{max}$, where R_{max} is the largest of seven successive values of $R_{t,i}$ (see Fig. 25a) calculated over an evaluation length, and b is the average pitch of the measured roughness profile; however, other works in the literature [200,211] have considered $a = R_v$, where R_v is the maximum valley depth (see Fig. 25a). Sanaei and Fatemi [275] highlighted the fact that their choice of $a = R_{max}$ was due to the impossibility of the stylus method accurately capturing the surface profile owing to the stylus itself; however, interestingly, they noticed that the evaluated equivalent surface roughness defect size $\sqrt{area_{R,max}}$, considering $a = R_{max}$, was very close to the value of R_v.

In the more general case of an inclined semi-elliptical crack, the SIF geometry factor, Y, can be evaluated as suggested by Murakami [285]:

$$Y_{IB} = [(0.66 + 0.23\beta^2) + (0.462 + 0.17\beta^2)(1 - \frac{a}{b})]\cos^2\beta \tag{9}$$

$$Y_{IIB} \cong \left(0.71 - 0.13\frac{a}{b}\right)\sin\beta\cos\beta \tag{10}$$

where a/b is the aspect ratio and β is the inclination angle, according to Fig. 25b and d.

Another possibility is to consider the projection of the defect area, $\sqrt{area_p}$, on the plane perpendicular to the MPS direction in the

case of tensile failure mode.

$$\sqrt{area_p} = \sqrt{area_{eff,\max}}\cos\beta \tag{11}$$

where $\sqrt{area_{\mathrm{eff},max}}$ is the effective initial crack size (see Eq. (6)). With reference to Eq. (11), according to Murakami [285], the SIF can be evaluated as:

$$K_I = Y \cdot \sigma\sqrt{\pi\left(\sqrt{area_p}\right)} \tag{12}$$

where the SIF geometry factor, Y, is 0.65 for surface defects and 0.5 for internal defects [286]. According to Sanaei and Fatemi [234], when dealing with the shear failure mode, a similar approach can be considered by projecting the defect area on the maximum shear plane.

A simplified approach to consider the surface roughness effect was proposed by Zhang and Fatemi [200] who considered the surface roughness as a surface crack with a depth given by the sum of the maximum surface valley, R_v, and a defect-induced crack length, a_0. By assuming a semi-circular crack, the stress intensity factor can be evaluated as:

$$K_I = \alpha\sigma\sqrt{\pi(R_v + a_0)} \tag{13}$$

where α denotes the SIF correction factor [200]. However, assumptions must be made based on component geometry. Zhang and Fatemi [200] considered a thumbnail crack in a hollow cylinder; with the crack growing through the wall of the tubular specimen, then changing to a center through-thickness crack [281] to meet the proper geometrical conditions.

As procedures to evaluate the SIFs in the case of AM defects, these can be used to predict the fatigue life through fatigue crack growth methods. The most commonly used FM models, based on SIFs, are presented in the following section.

4.3.2. *Fracture mechanics approaches applied to AM components under multiaxial loading conditions*

When a small plastic zone at the crack notch tip can be assumed according to the material properties, the fatigue life estimation can be performed according to linear elastic fracture mechanics (LEFM) following the Paris equation for the linear steady crack growth rate region:

$$\frac{da}{dN} = C\left(\Delta K_{eq}\right)^n \tag{14}$$

where C and n are parameters depend on the material used, a is half of the crack length, N are cycles and ΔK_{eq} is the equivalent SIF range. The fatigue life, N_f, can be assessed as:

$$N_f = \int_{a_0}^{a_c} \frac{da}{A\left(\Delta K_{eq}\right)^n} \tag{15}$$

where a_0 is the initial crack length and a_c is the critical crack length. It should be noted that this procedure can be applied to deal with long cracks. The Kitagawa–Takahashi method approximates a crack size, called small crack size, to distinguish between small and long cracks for the material considered. The small crack size, a_{small}, can be obtained by comparing the equations for the long crack threshold and fatigue limit [242]:

$$a_{small} \approx \frac{1}{\pi}\left(\frac{\Delta K_{th}}{\Delta\sigma_f}\right)^2 \tag{16}$$

where ΔK_{th} is the SIF threshold value and $\Delta\sigma_f$ is the fatigue limit.

A generalized Paris equation can be effective in avoiding modeling the plasticity effect at a short crack tip. This approach was used to achieve an asymptotic match between the Paris and Basquin equations or a Kitagawa–Takahashi method extended to a finite life [188,287]. The application of the generalized Paris equation for AM components was proposed by Sanaei and Fatemi [234] on the assumption that in the ideal case of a defect-free condition, the AM component would behave like a wrought metal, with failure starting at slip bands, and would have the same fatigue properties. In this ideal case, the fatigue life, $2N_f$, estimated through the integration of the Paris equation (Eq. (14)) should be equal to the prediction of Basquin's equation (Eq. (17)) for the wrought material:

$$\frac{\Delta\sigma}{2} = \sigma_f^{'}\left(2N_f\right)^b \tag{17}$$

where $\Delta\sigma$ is the stress range, $\sigma_f^{'}$ is the fatigue strength coefficient and b is the fatigue strength exponent. Details about the applications of this approach can be found in [234].

Another widely used crack growth equation is NASGRO, which accounts for the stress ratio R, crack closure, and tails at the upper and lower ends of the growth rate curve and is given by [288]:

$$\frac{da}{dN} = D\left[\left(\frac{1-f}{1-R}\right)\Delta K\right]^{n} \frac{\left(1-\frac{\Delta K_{th}}{\Delta K}\right)^{p}}{\left(1-\frac{K_{\max}}{K_c}\right)^{q}} \tag{18}$$

where D and n are material parameters, p and q are empirical coefficients that determine the curvature of the growth rate curve in the tail regions selected to fit the experimental data, ΔK_{th} is the threshold SIF range, R is the stress ratio, f is the Newman crack closure function [288], K_{max} is the maximum SIF, and K_c is the critical SIF.

In the Hartman–Schijve (H–S) variant of NASGRO, the material constants, D and P, are no longer dependent on the crack length. This equation captures the growth of small submillimeter cracks [289,290]:

$$\frac{da}{dN} = D\left[\frac{\Delta K - \Delta K_{thr}}{\sqrt{1-\frac{K_{\max}}{A}}}\right]^{P} = D\left[\frac{\Delta K - \Delta K_{thr}}{\sqrt{1-\frac{\Delta K}{(1-R)A}}}\right]^{P} \tag{19}$$

where A is the cyclic fracture toughness and ΔK_{thr} is the effective lower fatigue threshold selected to fit the measured da/dN versus ΔK data according to the H–S equation; it is worth highlighting that these are different from the actual fracture toughness K_C and fatigue crack growth threshold ΔK_{th}, which are experimentally derived [289].

The sensitivity of the predictions using the H–S variant of the NASGRO equation to the parameters involved are available in the literature [234]. The initial defect size can significantly affect the predictions and becomes less significant as the initial defect becomes more elongated; the effects of variations in the constant D and exponent P on the prediction curve become less significant in the HCF, and the threshold value ΔK_{th} has a significant effect on the prediction results, particularly in the HCF. A, which represents the cyclic fracture toughness, and the final crack size barely affect the predictions.

Another option is to use software such as FASTRAN [291–293] whose fatigue model is based on a plasticity-induced crack closure mechanism and considers an effective SIF range. Using a damage rule that does not require the reordering of the loading history makes it particularly useful when dealing with real operational conditions [167]. The main crack-growth relation used by FASTRAN is:

$$\frac{da}{dN} = C\left(\Delta K_{eff}\right)^{m}\left[1-\left(\Delta K_0/\Delta K_{eff}\right)^{p}/\left(1-\left(K_{\max}/K_{Ie}\right)^{q}\right)\right] \tag{20}$$

where C and m are the Paris equation constants, p and q are constants used to fit the test data in either the threshold or fracture regions, ΔK_0 is the effective stress intensity factor at the threshold, ΔK_{eff} is the effective stress intensity factor, ΔK_{max} is the maximum stress intensity factor, and K_{Ie} is the elastic stress intensity factor at failure. ΔK_{eff} is calculated as follows:

$$\Delta K_{eff} = \left[\left(1-\sigma_0^{'}/\sigma_{\max}\right)/(1-R)\right]\Delta K \tag{21}$$

In this equation, $\sigma_0^{'}$ is the crack-opening stress calculated using FASTRAN. This value is higher than σ_0, which is the crack-opening stress computed from the original crack-opening stress equations without using the crack tip growth element. More information on the model considered by the FASTRAN software can be found in [167,292,293]. However, it is worth highlighting that FASTRAN only considers mode I crack growth, and to extend its application to multiaxial loading conditions or mixed-mode crack growth in which the effective area of the defect continuously changes according to the loading, Molaei and Fatemi [167] estimated the crack initiation defect by projecting the defect on the maximum damage plane orientation according to the FS critical plane approach. The application of FASTRAN has also been extended for the fatigue assessment of notched components under the assumption of mode I crack initiation and growth with an equivalent axial stress to be evaluated starting from the local equivalent von Mises stress using the appropriate stress concentration factors [167,225].

4.3.3. Application of FM for multiaxial fatigue assessment of unnotched geometries

Dealing with as-built AM components, Zhang and Fatemi [200] compared two different methodologies to establish the initial crack size considering the surface roughness through the application of the Paris law (see Eq. (14)). Fatigue tests of unnotched AM Ti6Al4V specimens under both annealed and HIPed conditions were used to assess the accuracy of the considered methodologies. Owing to the brittle martensitic microstructure of their annealed Ti6Al4V specimens (see Fig. 14f), the assumption of a small plastic zone required for the application of LEFM following the Paris equation was verified.

The first approach analyzed by Zhang and Fatemi [200] considered the surface roughness as a surface crack with a depth given by the sum of the maximum surface valley, R_v, and a defect-induced crack length, a_0 (see Eq. (13)), which was assumed to be negligible; thus, $a_0 = 0$. The second approach considered Murakami's defect area method, as explained in Section 4.3.1, neglecting the term related to subsurface defects. The comparison between fatigue data related to annealed and HIPed conditions revealed non-conservative predictions by the first approach for the annealed conditions, which could be related to multiple crack interactions on the rough surface, synergistic effects of the rough surface and subsurface defects not accounted for in the models, or the inability of the surface profiler to accurately describe the deepest valley of the surface profile.

However, it is worth highlighting the accuracy of their predictions considering that the fatigue crack growth data were estimated from experimental data in the literature with consequent possible differences in process parameters, geometry, and all the other aspects treated in the previous section. The crack growth rate was assumed to be the same for different loading conditions, even though different fatigue crack growth rates have been reported in the literature with changing loading conditions [241,294]. The estimated

small crack size, according to [242], was higher than the initial assumed crack length, R_v, revealing possible small crack growth effects not accounted for in the model.

A more conservative prediction from the $\sqrt{area}$ model compared to the roughness model described by Eq. (13) was also observed at the same stress level, as seen in Fig. 26; this was due to a larger initial crack length estimated by the Murakami method.

It is worth highlighting that Sanaei and Fatemi [234], by applying the $\sqrt{area}$ method, documented a roughness-equivalent defect size very close to the value of the R_v parameter assumed as the initial crack length in the first approach used in [200], despite being calculated with different surface roughness parameters with respect to those considered in [200]. This indicates that the Murakami method can be highly affected by the surface parameters chosen to determine the roughness-equivalent defect size; indeed Molaei et al. [116] evaluated the equivalent surface roughness defect size according to [234] and, without neglecting the synergistic effect due to the subsurface defects that were relatively large in the fatigue dataset considered, they were able to predict with an acceptable degree of accuracy the fatigue test data under different loading conditions. Indeed, it is worth noting how the predictions in [116], even considering the effect of subsurface defects, were less conservative when compared with the predictions in [200] as seen by comparing Fig. 26a and Fig. 27a. However, this could also be related to the different aspect ratios considered for the assumed initial crack—lower in [116], which has been seen to reduce the expected fatigue life. Acceptable predictions, as documented in [116] also deal with machined surface conditions in which only the internal defects were considered in evaluating the effective initial defect size owing to the relatively negligible values of the measured surface roughness; see Fig. 27b.

The same dataset considered by Molaei et al. [116] has also been investigated by Sanaei and Fatemi [275] using the H–S variant of the NASGRO equation; in this case, a higher degree of inconsistency was detected between the expected and experimental results, specially at very short and long fatigue lives, as seen in Fig. 28. The causes of this discrepancy have been hypothesized to be the consideration of a unique value of the initial crack length and aspect ratio for all the specimen batches, and in the failure mechanism that, under complex loading conditions, could differ significantly from the tensile failure mode.

Using the H–S variant of NASGRO and considering the FS parameter as the driving force for crack growth, Sanaei and Fatemi [275] investigated also a dataset with different surface conditions, in which shear-dominated failures were observed. Similar to the other dataset, a unique initial defect size and aspect ratio were considered for all the batches, and the fatigue crack growth properties were based on mode I values found in the literature. In this case, however, the predictions showed conservativism at the HCF and non-conservativism at the LCF,; the discrepancies at the LCF could be related to extended local plasticity and consequent violation of the LEFM assumptions. However, it is worth noting that long crack growth rate properties were used for predictions, as the needed small crack growth rate properties were not available; the predictions are expected to improve if small crack growth properties for each crack growth mode are considered.

Improved accuracy has been observed with the application of the H–S variant of the NASGRO equation for 17-4 PH stainless steel experiencing shear-dominated failure, as shown in Fig. 29.

It is also worth mentioning that, in the case of unnotched specimens under variable amplitude service loading conditions, a recent study [167] employed the FASTRAN software for fatigue life prediction. Assuming a semi-elliptical crack with size established as in [234], good agreement was found between the predicted and experimental sequences for the failure of the Ti6Al4V and 17-4 PH AM specimens in both the as-built and machined conditions.

4.3.4. Application of FM for multiaxial fatigue assessment of notched geometries

The fatigue life prediction of complex geometries using FM-based models is further complicated by the interaction between the component geometry and defects. Assuming mode I crack initiation and growth for notched components, it has been shown in literature [167,225], through the software FASTRAN (see Eq. (20)), the importance of the assumptions made regarding the relative position between the initial crack and global geometrical discontinuity in the component. Location and shape of the assumed initial

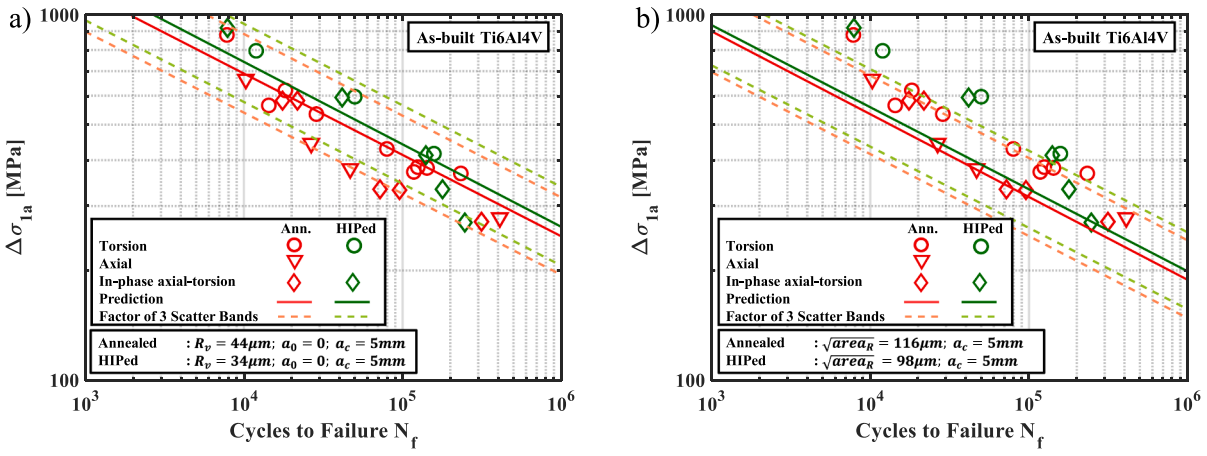

Fig. 26. Fatigue life prediction of as-built annealed (Ann.) or HIPed Ti6Al4V specimens accounting for surface roughness through a) Eq. (13) and Paris law and b) Murakami method and Paris law. Figure adapted from [200].

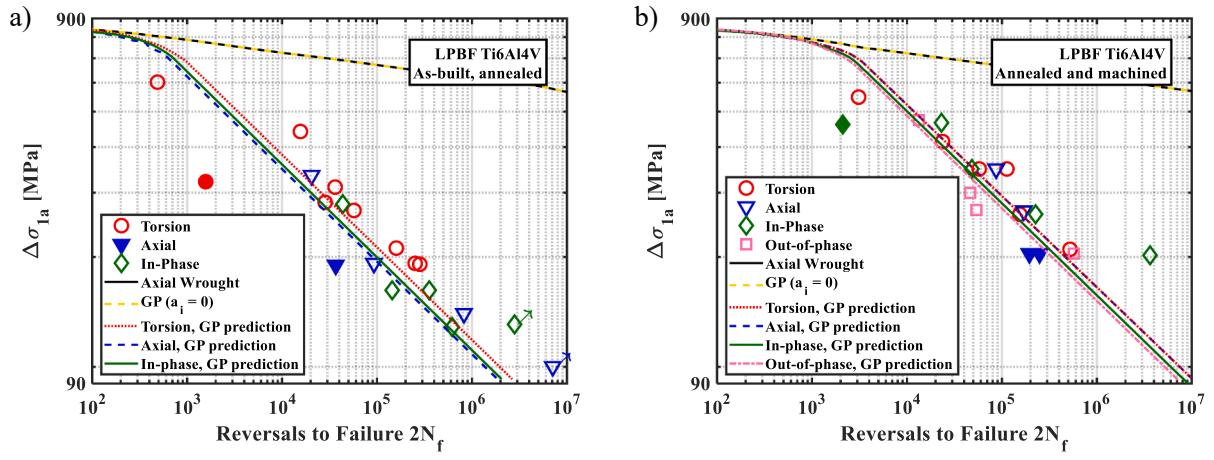

Fig. 27. Fatigue life prediction through generalized Paris Law for annealed LPBF TI6Al4V specimen under different loading conditions for a) as-built surface condition (Aspect ratio = 0.25) and b) machined surface condition (Aspect ratio = 0.5). Figure adapted from [116].

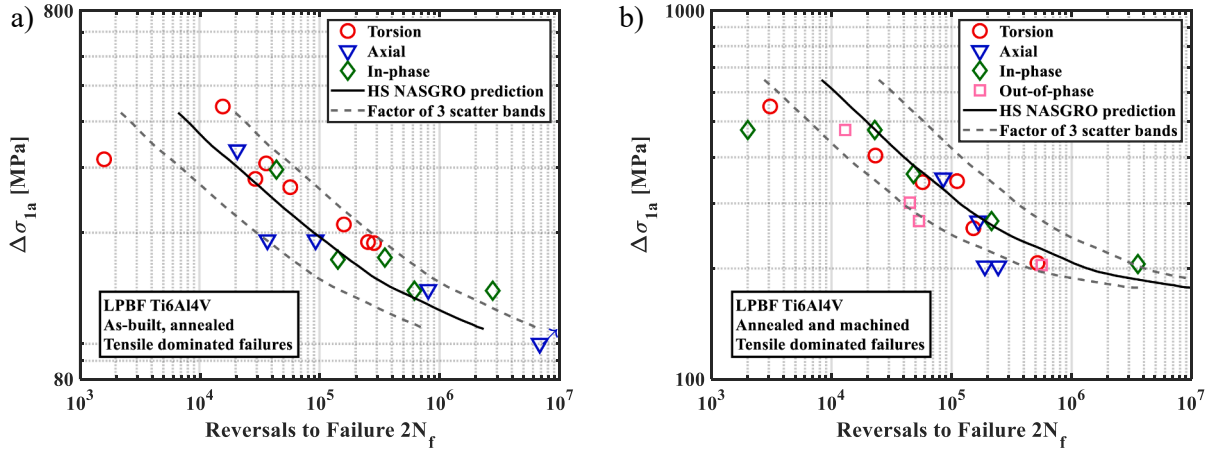

Fig. 28. Fatigue life prediction through H–S NASGRO equation for LPBF annealed Ti6Al4V specimens experiencing tensile-dominated failure under multiaxial loading conditions for a) as-built and b) machined surface conditions. Figure adapted from [275].

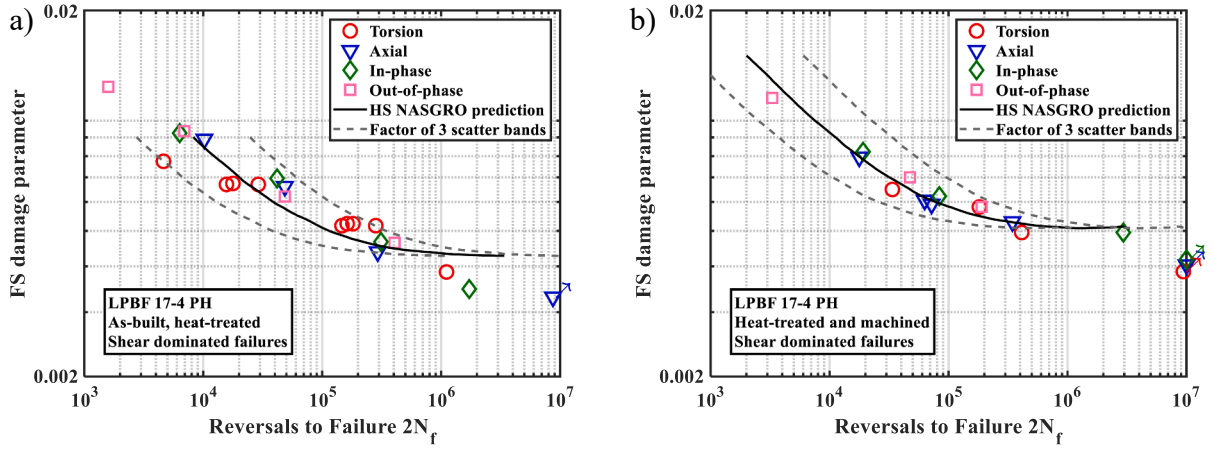

Fig. 29. Fatigue life prediction through H–S NASGRO equation for LPBF heat-treated 17-4 PH under multiaxial loading conditions for a) as-built and b) machined surface conditions. Figure adapted from [275].

crack have also been shown to be dependent on the surface conditions.

Regarding the Ti6Al4V as-built notched component, Molaei et al. [225] assumed a through-thickness crack at the notch edge in the thickness direction due to the rough surface, as shown in Fig. 30a. The initial defect size, a, in Fig. 30a, was defined in two different ways: with and without considering the synergistic effect of surface roughness and subsurface defects. The maximum roughness profile valley depth, R_v, as in [200], and the sum of R_v plus the maximum observed subsurface defect, R_v + *defect*, were assumed as initial crack lengths, with better prediction for the latter hypothesis for as-built surface conditions (see Fig. 30c). This may seem in contrast with the observations in [200], but it is worth highlighting that, while Molaei et al. [225] investigated as-built components, the specimens considered in [200] were subjected to post-treatment processes (annealing or HIPing); indeed, in [200] a sensitivity analysis of the fatigue life prediction model revealed that the consideration of an additional defect-related size led to worse fatigue life estimations for the fatigue data analyzed, again demonstrating the importance of the heat treatments performed on the AM specimens. Another difference between the two studies is that the FM approach considered by Molaei et al. [225] and applied through the FASTRAN software [291–293] is based on plasticity-induced crack closure and considers an effective SIF range. Indeed, consideration

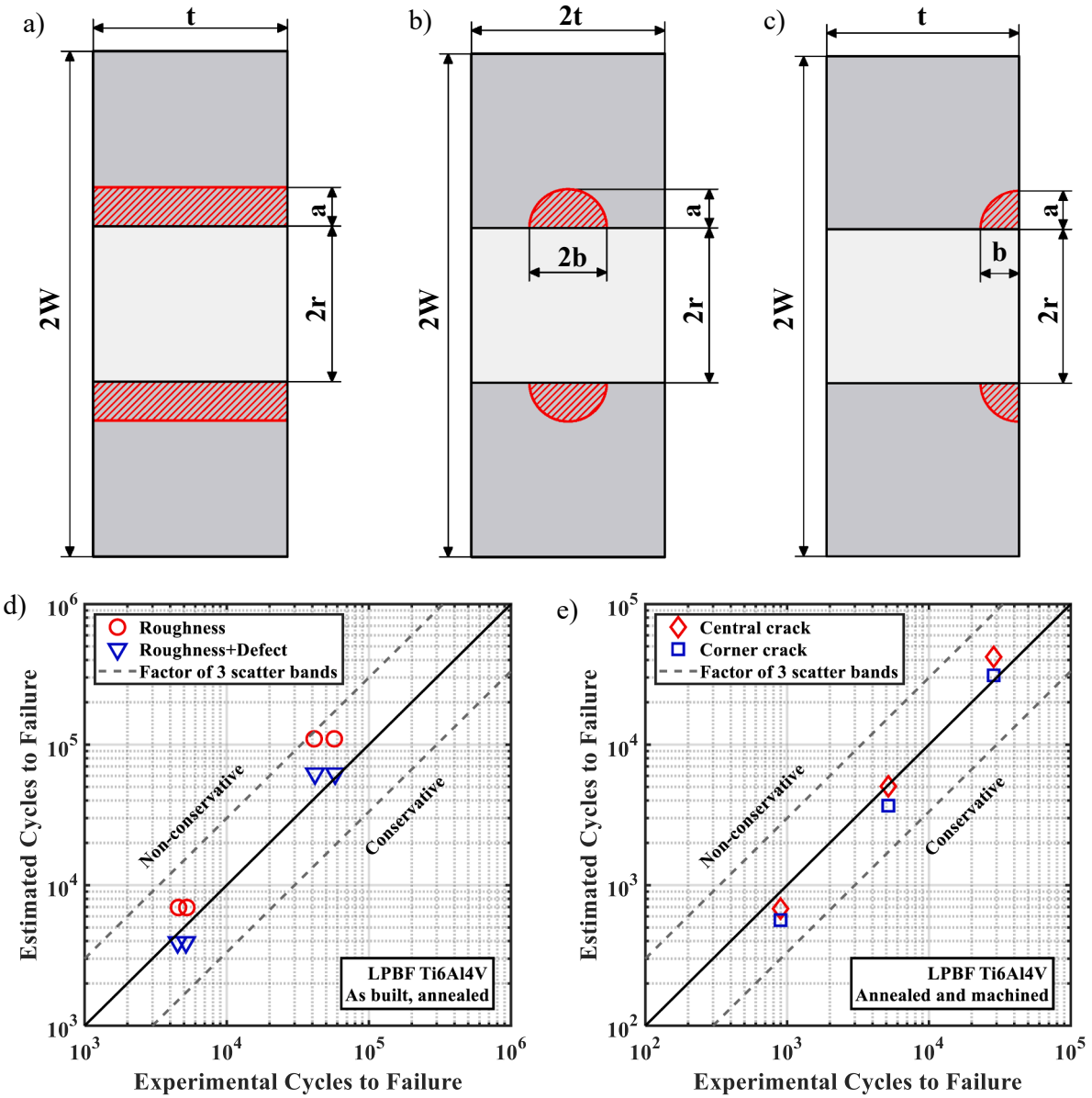

Fig. 30. a) Through-thickness crack with width c equal to R_v and R_v +defect representative of as-built specimens; b) center crack configuration; c) corner crack configuration representative of machined surface notched specimens; d) life estimation and sensitivity to the size of the considered defect for notched annealed as-built Ti6Al4V specimens under uniaxial loading; e) life estimation and sensitivity to the size of the location of the defect for notched annealed machined Ti6Al4V specimens under uniaxial loading. Figure adapted from [225].

of the crack closure phenomenon leads to the same initial defect size resulting in a higher expected fatigue life. However, it is worth noting that the component geometry was different in the two studies (unnotched in [200] and notched in [225]). Considering the negligible effect of the surface roughness in the machined condition, two different crack/defect configurations were also considered: two symmetrical cracks at the center of the notch hole (see Fig. 30b) and two symmetrical corner cracks at the edge of the notch hole (Fig. 30c) with a crack aspect ratio of one for simplicity. The configuration shown in Fig. 30b leads to more accurate results for Ti6Al4V specimens, as shown in Fig. 30e, which is in accordance with the experimental observations showing crack initiation in the specimen thickness region [225] in which a slightly higher equivalent stress was observed [167].

Another aspect that should be considered is that in both [225] and [167], the fatigue life was divided into two stages: small crack growth (SCG) and long crack growth (LCG). For machined conditions, the SCG was assumed to finish when the crack reached a length equal to half the wall thickness and was seen on the outer surface for the center crack configuration to have a proper comparison with experimental data. For consistency reasons, the same crack length was assumed to be the end of the SCG phase in the other configurations. Looking at the crack length vs. cycles for LCG estimations, as shown in Fig. 31, a high degree of accuracy of the predicted vs. experimental fatigue life can be observed. It is also important to highlight that the experimental data considered both constant amplitude (Fig. 31a and Fig. 32b) and variable amplitude loads as a realistic load history measured from underwing of an aircraft (Fig. 31b and Fig. 32b); more details about the load history can be found in [167].

The fatigue life prediction of the method described above is shown in Fig. 32a, which deals with axial, torsional, in-phase, and 90° out-of-phase fatigue tests [225] and in Fig. 32b under variable amplitude service loading conditions [167] showing a good degree of accuracy for all the surface conditions and both AM metals considered. However, considering the high degree of accuracy of the model in the LCG region that it is possible to observe in Fig. 31, the lower accuracy of the predictions at a longer life could be related to small crack growth not properly considered due to unavailability of small crack growth data to be used for the predictions., The higher data scatter for the Ti6Al4V specimens in machined surface condition was reported to be due to a higher degree of randomness in the size and location of the internal defects, in contrast to the as-built surface condition where cracks initiate from the rough surface.

5. Modeling of real AM components

Specimens defined in standards represent the main means for investigating the material fatigue behavior, achieving insights regarding the failure mechanisms and influencing parameters. The experimental results are also useful for assessing the performance of various methods to determine the fatigue life, with the aim of applying the same methods with reliable estimations to real components. However, when dealing with AM parts, the mechanical properties and fatigue performance of real components may differ significantly from those achieved through specimens, owing to the large number of parameters that have been shown to influence the expected fatigue behavior. Assessing the fatigue performances of real components is an expensive task, but it is necessary when a higher degree of safety should be guaranteed; the research efforts are all devoted to minimizing the cost and time for this expensive investigation.

Kasprzak et al. [295] performed uniaxial fully-reversed fatigue tests on an AM machined HIPed flight-critical nacelle link of an aircraft made with LPBF Ti6Al4V, along with witness coupons printed in two different directions, as shown in Fig. 33a. The link was tested under axial loading with $R = -1$ and the witness coupons were tested under axial loading at $R = 0.1$ and $R = -1$ load ratios. Tubular specimen test results built on a different built Platform and subjected to axial, torsion, and combined in-phase and out-of-phase loadings at $R = -1$ are also shown in the figure.

Stresses and strains at the critical fatigue locations of the nacelle link were achieved through nonlinear FE analysis considering the steady-state cyclic stress–strain properties. Even when the fatigue tests were performed through a global uniaxial load on the component (see Fig. 33b), owing to the geometry, a multiaxial stress state characterized the critical location in the component, and the comparison between the FE analysis and the actual fracture surfaces confirmed the consistency between the expected and actual failure locations, as shown in Fig. 33c, d, and e. Through FE analysis, Molaei et al. [116] showed that there was no correlation between the nominal stress ratio applied through the global load and the local stress ratio at the critical location that changed during the test, owing to the presence of residual stresses determined by plastic deformation during the tensile portion of the load, as shown in Fig. 33e.

Molaei et al. [116] correlated the results from the components and specimen coupons tested by Kasprzak et al. [295] and those tested in [169] using the modified FS critical plane reported in Eq. (3). Fig. 33f shows a summary of the results with a good correlation between all the data, which led to the conclusion that, under some conditions, a good estimation of the fatigue properties of real components can be achieved starting from laboratory specimens. However, it was highlighted that the considered data were related to component and specimens subjected to both HIPing and surface machining that, as has been shown in previous sections, significantly affect the scatter of the fatigue results in AM components. The machining of the surfaces results in a higher uncertainty in the location of the critical defects in the component, while the degree of the beneficial effect of HIP on the fatigue properties of the AM components strictly depends on subsequent machining to remove surface and near surface defects, as well as the initial size of the internal defects and, as a consequence, on the process parameters.

6. Summary and outlook

AM processes have the potential to offer significant advantages with respect to conventional manufacturing methods in mechanical components; indeed, while the production chain in conventional manufacturing involving several technologies needs to be tailored to a single product, AM techniques allow the possibility of realizing highly customized components not only in their geometry, but also in the material properties that could be controlled by introducing topologically optimized structure zones or changing the material composition throughout the component.

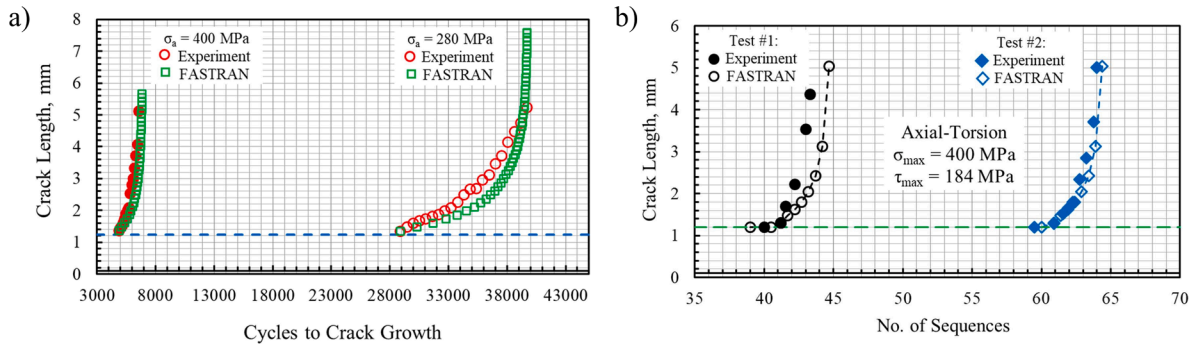

Fig. 31. Predicted vs. experimental LCG data for LPBF machined surface notched Ti6Al4V specimens under a) axial and constant amplitude loading and b) axial-torsion variable amplitude service loading conditions. Figure adapted from [167,225].

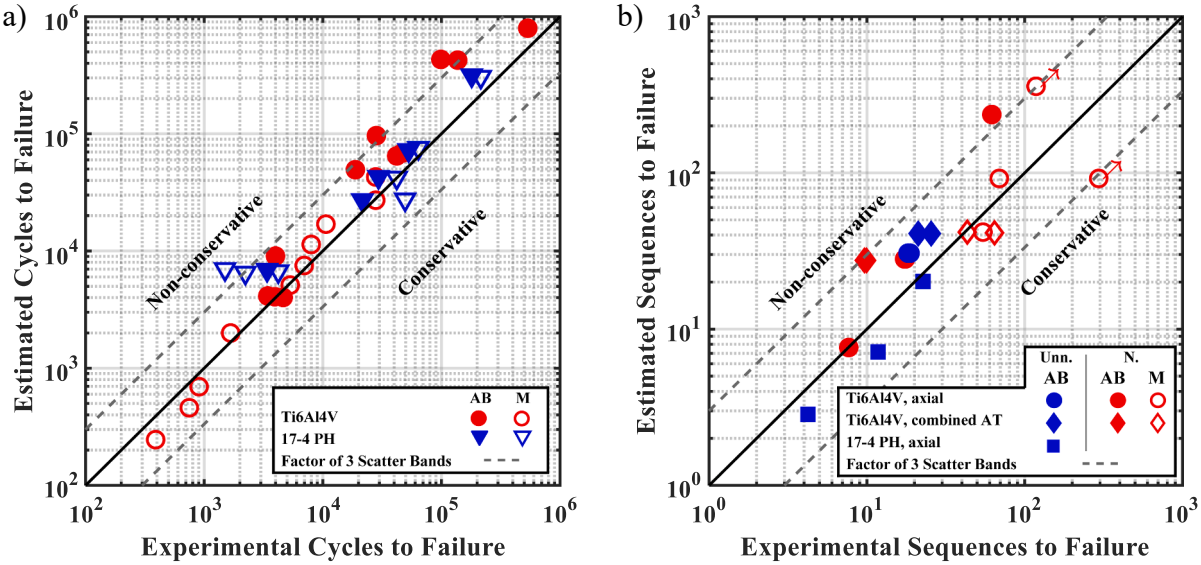

Fig. 32. Fatigue life prediction of FASTRAN software for LPBF Ti6Al4V and 17-4 PH alloys under: a) constant amplitude notched axial, torsional, in-phase, and 90° out-of-phase loading conditions; b) notched (N.) and unnotched (Unn.) variable amplitude axial and axial-torsion loading conditions. Both as-built (AB) and machined (M) conditions were considered. Figure adapted from [167,225].

However, their acceptance for industrial-scale applications at present is limited not only because of size and quantity restrictions, but also because of the high variability in the mechanical properties of these components subjected to the many manufacturing process parameters and post-process treatments. The establishment of reliable tools to assess their structural integrity and predict their expected fatigue life is indeed a challenging task.

An important advantage of the additive manufacturing process is the ability to manufacture complex geometries. However, such complex geometries often result in multiaxial stresses at fatigue-critical locations owing to the component geometry itself, or from application of multi-directional loads. In addition, anisotropic features and residual stress fields determined due to the complex thermal history experienced by AM components during their realization result in multiaxial stresses. Thus, multiaxial fatigue cannot be neglected to reach a proper understanding of the fatigue performance of these components and achieve reliability in their application.

The effects of several parameters were discussed in the present review, analyzing the fatigue behavior of AM metallic components with a focus on multiaxial stresses. The review considered studies that included fatigue data and analyses for LPBF Ti6Al4V and 17-4 PH alloys and different stress states resulting from axial, torsional, and combined axial–torsional loads. Many effects were considered including defects, surface roughness, anisotropy, post treatments such as HIP, as well as effects often present at the component level such as stress concentrations or notches and variable amplitude loads.

Process and post-process conditions significantly affect defect content, primarily consisting of porosity and LOF voids, which in turn affect fatigue performance, particularly at longer lives. Not only the size, but also shape, orientation, location, and distribution of defects can affect the fatigue behavior. Even with an optimum processing window for yielding maximum part density, LOF defects which are flat and often unmeasurable via standard density measurement methods, may still exist at relatively high part densities. LOF voids are more detrimental due to their irregular shape, as they can cause a greater stress concentration, when compared with

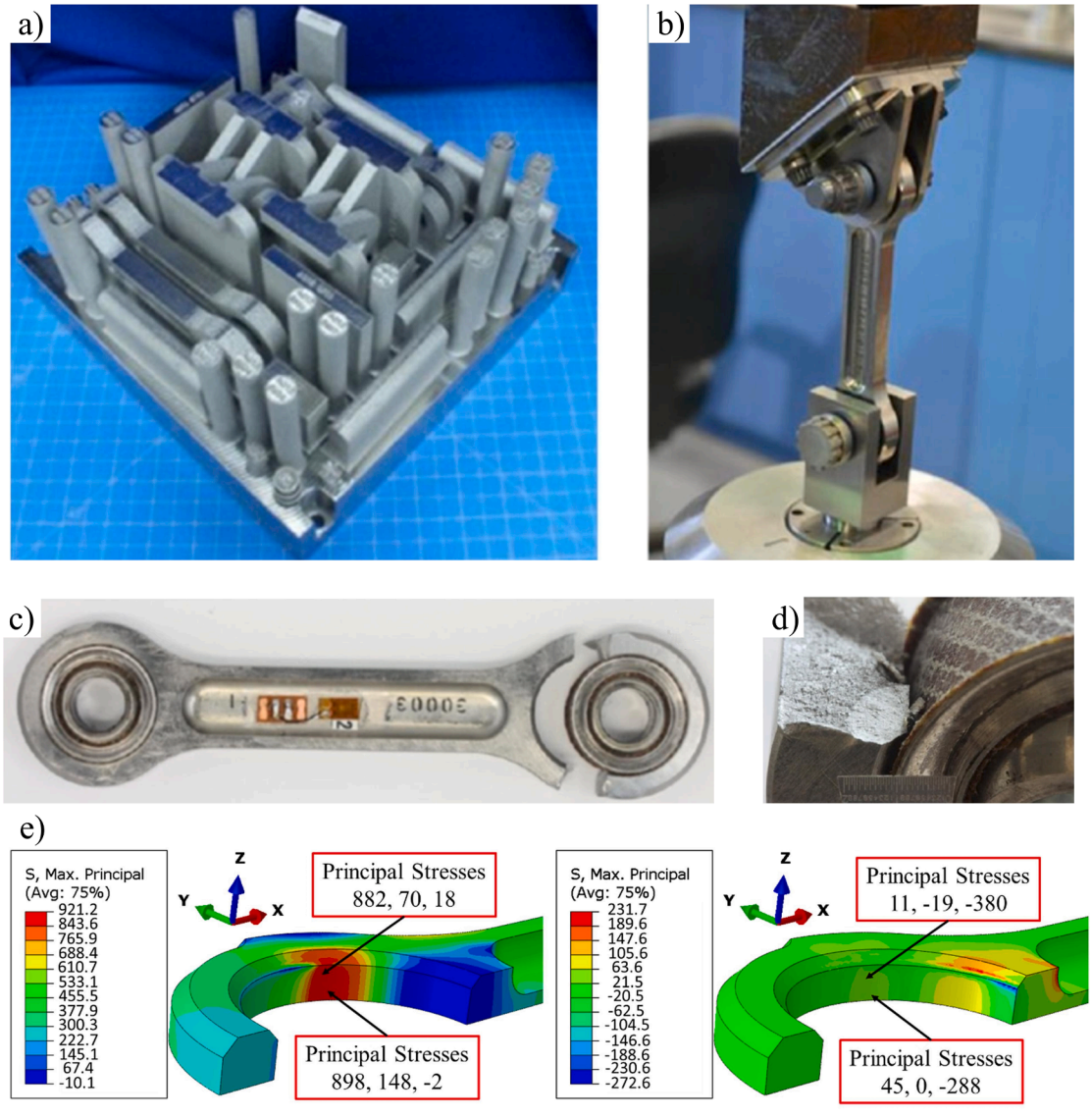

(caption on next page)

Fig. 33. a) Layout of the build plate for flight-critical nacelle link of an aircraft and witness coupons for specimen machining made with LPBF Ti6Al4V; b) fatigue test setup of the flight-critical nacelle link; c) failed nacelle link; d) fracture surface showing the crack initiation location; e) FE results of the link during the tension–compression load cycle showing consistency of failure loacation between the model and real component; f) fatigue data correlation through the FS critical plane approach considering specimen data from [169] and real component and test coupon data from [295]. Figure adapted from [116].

entrapped gas pores that are typically spherical.

AM parts in the as-built surface condition typically have significantly higher surface roughness relative to their traditionally manufactured counterparts because of the inherent repetitive nature of the fabrication process. The surface roughness is influenced by several factors including the manufacturing process type and parameters, powder size, part geometry, and layer thickness and orientation. Higher surface roughness is usually observed on the overhanging surface, as compared with the contracting surface (ie, the surface facing upward). Fatigue cracks in as-built surface condition almost always initiate from the surface. Therefore, removal of the rough outer layer thickness by machining or other methods can play a significant role in improving fatigue performance of AM parts. However, as one of the key advantages of the AM technique is the capability of fabricating complex geometries as net shape, machining of such complex geometries would be difficult, if not impossible. Therefore, choosing proper powder characteristics and optimizing AM process and design parameters to obtain a smoother surface are important considerations to enhance the fatigue performance.

Layer orientation can significantly affect the fatigue performance of AM parts, resulting in anisotropic behaviour. As the orientation of LOF defects are generally perpendicular to the build direction, fatigue behaviour can be related to the relative angle between the loading direction and layer orientation. Therefore, vertically built specimens with loading direction perpendicular to the defects typically exhibit shorter fatigue lives, as compared with horizontally built specimens with defect orientation parallel to the loading direction. However, in the absence of LOF defects, little or no anisotropy in fatigue performance has been observed. Although the relative angle between the loading direction and layer orientation can also dictate directionality of the microstructure, defect directionality plays a larger role on the anisotropic fatigue response.

The common annealing treatment, if done at proper temperature and duration, can significantly improve ductility and, therefore, reduce the notch sensitivity of defects, as well as reducing or relaxing residual stresses, and in some cases minimizing structural anisotropy. HIP is an effective thermo-mechanical treatment to reduce the volume of porosity and internal voids (LOF defects) and their sharpness. This results in improved fatigue resistance and reduced anisotropy. Experimental fatigue data for L-PBF Ti-6Al-4 V after the HIP treatment indicate a similar performance to that of the wrought material. However, the significant effect of HIP treatment can only be observed after subsequent machining since the rough surface of as-built HIPed specimens still plays a key role in shortening their fatigue lives, especially in HCF regime. It has also been observed that HIP effect may depend on the type of loading. For example, the effect has been found to be smaller in torsion, as compared to axial loading, where the difference between the two loading conditions with regards to HIPing effect may be attributed to the stress gradient in torsion, leading to a smaller highly stressed volume.

Observed crack initiation and crack growth orientations under different stress states indicate the failure mechanism and how they are affected by the defect morphology, and as a consequence, by the process parameters and post-treatment processes that are widely known to affect them. Shrinking or eliminating the internal defects and transforming the microstructure to a more ductile structure using the HIP process changes the tensile failure mechanism to shear failure mechanism. Surface roughness which was shown to significantly affect the multiaxial fatigue performance of AM materials, has a synergistic effect in combination with internal defects and component geometry and may lead to significant changes in the component fatigue performance. However, the microstructure has also been shown to have significant effects on the fatigue behavior, determining the damage mechanism affecting these components. Depending on cooling rates inherent to a particular AM process, a broad range of phase structures can be produced.

Presence of stress concentrations such as notches can significantly affect the load bearing capacity of AM parts. Cracking behavior at notches in AM parts can be very different from that in wrought metals due to the presence of surface and/or near surface defects and their interactions with the mechanically induced notch, anisotropy, ductility, and build orientation. When stress concentrations due to notches or geometry complexities are present in AM metal parts, the effect of internal defects may become small and the notched fatigue behavior could be similar to the notched wrought metal. However, a built-in notch can result in significant shorter fatigue life as compared to a machined notch because of the rough surface of the as-built notch vs the smooth surface of a machined notch. Also, while different heat treatments can significantly affect the fatigue performance of AM metals in the unnotched condition, they may have a small effect when a mechanically induced notch is present.

Fatigue data are often generated under constant amplitude loading, while service load histories are typically variable amplitude in nature. Under such loading, effects such as load sequence and interactions become important. If periodic overloads exist in the load history and the AM material microstructure is such that cyclic hardening or softening occurs during the overload cycles, then deformation memory effect becomes an important consideration. It should also be noted that while a fatigue limit or endurance limit may be exhibited under constant amplitude loading, such limits do not generally exist under variable amplitude loading. In such cases, stress or strain amplitudes below the endurance limit from a S-N or strain-life curve generated from constant amplitude loading, will cause fatigue damage under variable amplitude service load histories.

Several fatigue prediction methodologies were reviewed with a focus on their accuracy in correlating fatigue data subjected to different loadings in both as-built and machined surface conditions and considering the effect of post-processing treatments. The identification of the damage mechanism affecting the component is the basis for achieving an accurate fatigue assessment under multiaxial loading conditions. Critical plane approaches, especially those considering the modified FS damage parameter which are consistent with the physics of the damage process, have been shown to provide a feasible tool for the multiaxial fatigue assessment of

AM components. The fatigue data correlations and life predictions presented based on this approach included both unnotched and notched data, as well as well as constant and variable amplitude axial and multiaxial loading conditions.

FM approaches were also considered, and it was shown that the reliability of their predictions is highly dependent on the assumed defect location and size and on the applied methodology to account for surface roughness; their application is also subject to the availability of statistical studies describing the defect morphologies inside the AM components, where defects are significantly affected by the large number of parameters involved in AM processes. Extreme Value Statistics (EVS) and equivalent defect size based on Murakami's method for approximation of the initial defect size have shown promising results for representation of defects and surface roughness in application of FM approach to fatigue life prediction of AM metals.

The fatigue data correlations and life predictions presented included data with different crack growth modes, depending on the observed crack growth mechanism for each material, manufacturing process, and post-process conditions. Predictions are expected to improve if small crack growth properties for each crack growth mode would have been available, instead of using mode I long crack growth properties for the predictions. Consideration of roughness-induced crack closure under mode II and mixed-mode crack growth may also be an important aspect to consider. The significant attention gained by AM technologies in recent years has provided a growing insight into the mechanical behavior of AM components. In addition, multiscale simulation techniques, which can predict the defect distribution and microstructure of the resulting structure by considering the thermal history [275] of the component, in combination with new investigation techniques, such as data-driven approaches [296–303], can help in relating several process parameters with the component mechanical behavior to increase their reliability and, thus, their real application, while decreasing the need for expensive and time-consuming experimental campaigns.

The full potential of AM with respect to fatigue performance has yet to be realized. For example, depending on cooling rates inherent to a particular AM process, a broad range of phase structures can be produced, monitoring or controlling the melt pool size may lead to the ability to custom tailor microstructure for a desired application, or improvements in in-situ monitoring and ultimately closed loop control can provide the ability to fabricate a functionally graded microstructure [196]. Data-driven approaches can help in relating process parameters to attributes affecting fatigue performance. For example, while surface roughness is known to reduce the fatigue resistance of as-built AM parts, there is not a clear consensus of which roughness parameters can most effectively capture this effect. Such approaches may provide quantitative models to account for the effect of these surface discontinuities on fatigue performance.

Nearly all the fatigue data are for cycles to failure less than 10^7 cycles. In some applications the life regime of interest is much higher, e.g., giga cycle fatigue. Testing in this life regime is not feasible with conventional fatigue testing machines. New testing machines that can operate at kHz frequencies are now more widely available to probe this important life regime in AM materials and investigate the role of AM defects and their characteristics. Also, factors such as size effects, friction and contact stresses, and environmental effects which typically are not considered in the laboratory scale can result in different fatigue behaviors at the component level. For example, different locations of AM fabricated components may have different microstructures and defect characteristics due to different thermal histories. It is also important to consider the environmental effects such as corrosion in the component scale study of AM metals, where the variabilities in the microstructure and defects can result in very different corrosion behaviors, even for a particular part.

To produce AM functional parts, qualification and certification will be needed to ensure safety, consistency, and reliability of performance. The current qualification or certification procedures rely on a "building block" concept and a statistical approach based on extensive mechanical test data to quantify uncertainty with respect to material and process variations, requiring extensive physical testing. Experimental qualification and certification are time extensive and costly as any changes in part size/geometry, process, or post-process conditions affect the thermal history, which, in turn, can affect microstructure, defect distribution, mechanical properties, and ultimately part performance. Developing an effective qualification and certification approach requires a good understanding of the large number of machine-to-machine and process parameter variabilities. This can be facilitated by integrating experiments and computational modeling based on material models at multiple length scales, including simulation of the thermal history to predict the resulting microstructure and defect formation.

Declaration of Competing Interest

The authors declare that they have no known competing financial interests or personal relationships that could have appeared to influence the work reported in this paper.

Data availability

The data that has been used is available in literature.

References

[1] Padture NP, Gell M, Jordan EH. Thermal barrier coatings for gas-turbine engine applications. Science (80-) 2002;296:280–4. https://doi.org/10.1126/science.1068609.
[2] Cooley WG. Application of functionally graded materials in aircraft structures 2005.
[3] Kellner T. Fit to print: new plant will assemble world's first passenger jet engine with 3D printed fuel nozzles, next-gen materials. Gen Electr Boston, MA, Accessed Nov 2014;29:2016.

[4] Taminger KM, Hafley RA. Electron beam freeform fabrication for cost effective near-net shape manufacturing. NATO/RTO AVT-139 Spec. Cost Eff Manuf via Net Shape Process 2006.
[5] Gasser A, Backes G, Kelbassa I, Weisheit A, Wissenbach K. Laser metal deposition (LMD) and selective laser melting (SLM) in turbo-engine applications. Laser Tech J 2010;2:58–63.
[6] Bici M, Brischetto S, Campana F, Ferro CG, Seclì C, Varetti S, et al. Development of a multifunctional panel for aerospace use through SLM additive manufacturing. Procedia Cirp 2018;67:215–20.
[7] Trivedi G. potential future applications of 3D printing within the aerospace industry 5AD.
[8] Jones JB, McNutt P, Tosi R, Perry C, Wimpenny DI. Remanufacture of turbine blades by laser cladding, machining and in-process scanning in a single machine 2012.
[9] Richter K-H, Orban S, Nowotny S. Laser cladding of the titanium alloy Ti6242 to restore damaged blades. Int. Congr. Appl. Lasers Electro-Optics, vol. 2004, Laser Institute of America; 2004, p. 1506.
[10] Gao J, Folkes J, Yilmaz O, Gindy N. Investigation of a 3D non-contact measurement based blade repair integration system. Aircr Eng Aerosp Technol 2005.
[11] Kelbassa I, Albus P, Dietrich J, Wilkes J. Manufacture and repair of aero engine components using laser technology. Pacific Int. Conf. Appl. Lasers Opt., vol. 2008, Laser Institute of America; 2008, p. 208–13.
[12] Zheng J, Li Z, Chen X. Worn area modeling for automating the repair of turbine blades. Int J Adv Manuf Technol 2006;29:1062–7.
[13] Dey NK, Liou FW, Nedic C. Additive Manufacturing Laser Deposition of Ti-6Al-4V for Aerospace Repair Applications 2013.
[14] Grady JE, Halbig MC, Singh M. A fully non-metallic gas turbine engine enabled by additive manufacturing. Int. Symp. Air Breath. Engines (ISABE 2015), 2015.
[15] Schimek M, Springer A, Kaierle S, Kracht D, Wesling V. Laser-welded Dissimilar Steel-aluminum Seams for Automotive Lightweight Construction. Phys Procedia 2012;39:43–50. https://doi.org/10.1016/j.phpro.2012.10.012.
[16] Schmitt M, Mehta RM, Kim IY. Additive manufacturing infill optimization for automotive 3D-printed ABS components. Rapid Prototyp J 2020.
[17] Kantareddy SNR, Roh BM, Simpson TW, Joshi S, Dickman C, Lehtihet EA. Saving weight with metallic lattice structures: Design challenges with a real-world example. University of Texas at Austin; 2016.
[18] Hands CH, du Plessis A, Minnaar N, Blakey-Milner BA, Burger E. Can Additive Manufacturing Help Win the Race? 2018.
[19] Patalas-Maliszewska J, Topczak M, Kłos S. The level of the additive manufacturing technology use in polish metal and automotive manufacturing enterprises. Appl Sci 2020;10:735.
[20] Leal R, Barreiros FM, Alves L, Romeiro F, Vasco JC, Santos M, et al. Additive manufacturing tooling for the automotive industry. Int J Adv Manuf Technol 2017;92:1671–6.
[21] Dwivedi G, Srivastava SK, Srivastava RK. Analysis of barriers to implement additive manufacturing technology in the Indian automotive sector. Int J Phys Distrib Logist Manag 2017.
[22] Böckin D, Tillman A-M. Environmental assessment of additive manufacturing in the automotive industry. J Clean Prod 2019;226:977–87.
[23] Sarvankar SG, Yewale SN. Additive manufacturing in automobile industry. Int J Res Aeronaut Mech Eng 2019;7:1–10.
[24] Wiese M, Thiede S, Herrmann C. Rapid manufacturing of automotive polymer series parts: A systematic review of processes, materials and challenges. Addit Manuf 2020;36:101582.
[25] Shanmugam S, Naik A, Sujan T, Desai S. Developing Robust 3D Printed Parts For Automotive Application Using Design For Additive Manufacturing And Optimization Techniques. INCOSE Int. Symp., vol. 29, Wiley Online Library; 2019, p. 394–407.
[26] Astori P, Zanella M, Bernardini M. Validation of numerical models of a rotorcraft crashworthy seat and subfloor. Aerospace 2020;7:174.
[27] Balla VK, Banerjee S, Bose S, Bandyopadhyay A. Direct laser processing of a tantalum coating on titanium for bone replacement structures. Acta Biomater 2010;6:2329–34.
[28] Zadpoor AA, Malda J. Additive Manufacturing of Biomaterials, Tissues, and Organs. Ann Biomed Eng 2017;45:1–11. https://doi.org/10.1007/s10439-016-1719-y.
[29] Tan XP, Tan YJ, Chow CSL, Tor SB, Yeong WY. Metallic powder-bed based 3D printing of cellular scaffolds for orthopaedic implants: A state-of-the-art review on manufacturing, topological design, mechanical properties and biocompatibility. Mater Sci Eng C 2017;76:1328–43. https://doi.org/10.1016/j.msec.2017.02.094.
[30] Yadroitsava I, Du Plessis A, Yadroitsev I. Bone regeneration on implants of titanium alloys produced by laser powder bed fusion: A review. Titan Consum Appl 2019:197–233.
[31] Zadpoor AA. Mechanical performance of additively manufactured meta-biomaterials. Acta Biomater 2019;85:41–59. https://doi.org/10.1016/j.actbio.2018.12.038.
[32] Murr LE. Open-cellular metal implant design and fabrication for biomechanical compatibility with bone using electron beam melting. J Mech Behav Biomed Mater 2017;76:164–77.
[33] Wang Y, Arabnejad S, Tanzer M, Pasini D. Hip implant design with three-dimensional porous architecture of optimized graded density. J Mech Des 2018;140:111406.
[34] Chen H, Han Q, Wang C, Liu Y, Chen B, Wang J. Porous scaffold design for additive manufacturing in orthopedics: A review. Front Bioeng Biotechnol 2020;8:609.
[35] Zhang X-Y, Fang G, Zhou J. Additively manufactured scaffolds for bone tissue engineering and the prediction of their mechanical behavior: A review. Materials (Basel) 2017;10:50.
[36] Zhang XZ, Leary M, Tang HP, Song T, Qian M. Selective electron beam manufactured Ti-6Al-4V lattice structures for orthopedic implant applications: Current status and outstanding challenges. Curr Opin Solid State Mater Sci 2018;22:75–99.
[37] Wang X, Xu S, Zhou S, Xu W, Leary M, Choong P, et al. Topological design and additive manufacturing of porous metals for bone scaffolds and orthopaedic implants: A review. Biomaterials 2016;83:127–41. https://doi.org/10.1016/j.biomaterials.2016.01.012.
[38] Murr LE. Strategies for creating living, additively manufactured, open-cellular metal and alloy implants by promoting osseointegration, osteoinduction and vascularization: An overview. J Mater Sci Technol 2019;35:231–41.
[39] Stucker BE, Obielodan JO, Ceylan A, Murr LE. Multi-material bonding in ultrasonic consolidation. Rapid Prototyp J 2010;16:180–8. https://doi.org/10.1108/13552541011034843.
[40] Benedetti M, du Plessis A, Ritchie RO, Dallago M, Razavi N, Berto F. Architected cellular materials: A review on their mechanical properties towards fatigue-tolerant design and fabrication. Mater Sci Eng R Reports 2021;144:100606. https://doi.org/10.1016/j.mser.2021.100606.
[41] Al-Saedi DSJ, Masood SH, Faizan-Ur-Rab M, Alomarah A, Ponnusamy P. Mechanical properties and energy absorption capability of functionally graded F2BCC lattice fabricated by SLM. Mater Des 2018;144:32–44. https://doi.org/10.1016/j.matdes.2018.01.059.
[42] Dallago M, Raghavendra S, Luchin V, Zappini G, Pasini D, Benedetti M. The role of node fillet, unit-cell size and strut orientation on the fatigue strength of Ti-6Al-4V lattice materials additively manufactured via Laser Powder Bed Fusion. Int J Fatigue 2020;105946. https://doi.org/10.1016/j.ijfatigue.2020.105946.
[43] Huynh L, Rotella J, Sangid MD. Fatigue behavior of IN718 microtrusses produced via additive manufacturing. Mater Des 2016;105:278–89. https://doi.org/10.1016/j.matdes.2016.05.032.
[44] Zhao S, Li SJ, Hou WT, Hao YL, Yang R, Misra RDK. The influence of cell morphology on the compressive fatigue behavior of Ti-6Al-4V meshes fabricated by electron beam melting. J Mech Behav Biomed Mater 2016;59:251–64. https://doi.org/10.1016/j.jmbbm.2016.01.034.
[45] Liu YJ, Wang HL, Li SJ, Wang SG, Wang WJ, Hou WT, et al. Compressive and fatigue behavior of beta-type titanium porous structures fabricated by electron beam melting. Acta Mater 2017;126:58–66. https://doi.org/10.1016/j.actamat.2016.12.052.
[46] Van Hooreweder B, Apers Y, Lietaert K, Kruth JP. Improving the fatigue performance of porous metallic biomaterials produced by Selective Laser Melting. Acta Biomater 2017;47:193–202. https://doi.org/10.1016/j.actbio.2016.10.005.
[47] du Plessis A, Razavi N, Benedetti M, Murchio S, Leary M, Watson M, et al. Properties and applications of additively manufactured metallic cellular materials: A review. Prog Mater Sci 2022;125:100918. https://doi.org/10.1016/j.pmatsci.2021.100918.

[48] Leary M. Design of titanium implants for additive manufacturing. In: Froes F, Qian M, editors. Titan. Med. Dent. Appl. Woodhead P, 2018, p. 203–24.
[49] Amin Yavari S, Ahmadi SM, Wauthle R, Pouran B, Schrooten J, Weinans H, et al. Relationship between unit cell type and porosity and the fatigue behavior of selective laser melted meta-biomaterials. J Mech Behav Biomed Mater 2015;43:91–100. https://doi.org/10.1016/j.jmbbm.2014.12.015.
[50] Kelly CN, Francovich J, Julmi S, Safranski D, Guldberg RE, Maier HJ, et al. Fatigue behavior of As-built selective laser melted titanium scaffolds with sheet-based gyroid microarchitecture for bone tissue engineering. Acta Biomater 2019;94:610–26. https://doi.org/10.1016/j.actbio.2019.05.046.
[51] Lietaert K, Cutolo A, Boey D, Van Hooreweder B. Fatigue life of additively manufactured Ti6Al4V scaffolds under tension-tension, tension-compression and compression-compression fatigue load. Sci Rep 2018;8:1–9. https://doi.org/10.1038/s41598-018-23414-2.
[52] Refai K, Brugger C, Montemurro M, Saintier N. An experimental and numerical study of the high cycle multiaxial fatigue strength of titanium lattice structures produced by Selective Laser Melting (SLM). Int J Fatigue 2020;138:105623. https://doi.org/10.1016/j.ijfatigue.2020.105623.
[53] Dallago M, Fontanari V, Torresani E, Leoni M, Pederzolli C, Potrich C, et al. Fatigue and biological properties of Ti-6Al-4V ELI cellular structures with variously arranged cubic cells made by selective laser melting. J Mech Behav Biomed Mater 2018;78:381–94. https://doi.org/10.1016/j.jmbbm.2017.11.044.
[54] Burr A, Persenot T, Doutre PT, Buffiere JY, Lhuissier P, Martin G, et al. A numerical framework to predict the fatigue life of lattice structures built by additive manufacturing. Int J Fatigue 2020;139:105769. https://doi.org/10.1016/j.ijfatigue.2020.105769.
[55] Bobbio LD, Otis RA, Borgonia JP, Dillon RP, Shapiro AA, Liu ZK, et al. Additive manufacturing of a functionally graded material from Ti-6Al-4V to Invar: Experimental characterization and thermodynamic calculations. Acta Mater 2017;127:133–42. https://doi.org/10.1016/j.actamat.2016.12.070.
[56] Zuback JS, Palmer TA, DebRoy T. Additive manufacturing of functionally graded transition joints between ferritic and austenitic alloys. J Alloys Compd 2019; 770:995–1003. https://doi.org/10.1016/j.jallcom.2018.08.197.
[57] Li Y, Feng Z, Hao L, Huang L, Xin C, Wang Y, et al. A Review on Functionally Graded Materials and Structures via Additive Manufacturing: From Multi-Scale Design to Versatile Functional Properties. Adv. Mater Technol 2020:5. https://doi.org/10.1002/admt.201900981.
[58] Rafiee M, Farahani RD, Therriault D. Multi-Material 3D and 4D Printing: A Survey. Adv Sci 2020;7:1–26. https://doi.org/10.1002/advs.201902307.
[59] Zhang B, Jaiswal P, Rai R, Nelaturi S. Additive Manufacturing of Functionally Graded Material Objects: A Review. J Comput Inf Sci Eng 2018:18. https://doi.org/10.1115/1.4039683.
[60] Tammas-Williams S, Todd I. Design for additive manufacturing with site-specific properties in metals and alloys. Scr Mater 2017;135:105–10. https://doi.org/10.1016/j.scriptamat.2016.10.030.
[61] Bandyopadhyay A, Heer B. Additive manufacturing of multi-material structures. Mater Sci Eng R Reports 2018;129:1–16. https://doi.org/10.1016/j.mser.2018.04.001.
[62] Loh GH, Pei E, Harrison D, Monzón MD. An overview of functionally graded additive manufacturing. Addit Manuf 2018;23:34–44. https://doi.org/10.1016/j.addma.2018.06.023.
[63] Carroll BE, Otis RA, Borgonia JP, Suh JO, Dillon RP, Shapiro AA, et al. Functionally graded material of 304L stainless steel and inconel 625 fabricated by directed energy deposition: Characterization and thermodynamic modeling. Acta Mater 2016;108:46–54. https://doi.org/10.1016/j.actamat.2016.02.019.
[64] Yan L, Chen Y, Liou F. Additive manufacturing of functionally graded metallic materials using laser metal deposition. Addit Manuf 2020;31:100901. https://doi.org/10.1016/j.addma.2019.100901.
[65] Reichardt A, Shapiro AA, Otis R, Dillon RP, Borgonia JP, McEnerney BW, et al. Advances in additive manufacturing of metal-based functionally graded materials. Int Mater Rev 2021;66:1–29. https://doi.org/10.1080/09506608.2019.1709354.
[66] Hofmann DC, Kolodziejska J, Roberts S, Otis R, Dillon RP, Suh JO, et al. Compositionally graded metals: A new frontier of additive manufacturing. J Mater Res 2014;29:1899–910. https://doi.org/10.1557/jmr.2014.208.
[67] Zhang C, Chen F, Huang Z, Jia M, Chen G, Ye Y, et al. Additive manufacturing of functionally graded materials: A review. Mater Sci Eng A 2019;764:138209. https://doi.org/10.1016/j.msea.2019.138209.
[68] Bandyopadhyay A, Zhang Y, Bose S. Recent developments in metal additive manufacturing. Curr Opin Chem Eng 2020;28:96–104. https://doi.org/10.1016/j.coche.2020.03.001.
[69] Fatemi A, Molaei R, Simsiriwong J, Sanaei N, Pegues J, Torries B, et al. Fatigue behaviour of additive manufactured materials: An overview of some recent experimental studies on Ti-6Al-4V considering various processing and loading direction effects. Fatigue Fract Eng Mater Struct 2019;42:991–1009. https://doi.org/10.1111/ffe.13000.
[70] Morgan EF, Unnikrisnan GU, Hussein AI. Annual Review of Biomedical Engineering Bone Mechanical Properties in Healthy and Diseased States 2018. Doi: 10.1146/annurev-bioeng-062117.
[71] Kemppainen JM, Hollister SJ. Differential effects of designed scaffold permeability on chondrogenesis by chondrocytes and bone marrow stromal cells. Biomaterials 2010;31:279–87. https://doi.org/10.1016/j.biomaterials.2009.09.041.
[72] Ali D, Ozalp M, Blanquer SBG, Onel S. Permeability and fluid flow-induced wall shear stress in bone scaffolds with TPMS and lattice architectures: A CFD analysis. Eur J Mech B/Fluids 2020;79:376–85. https://doi.org/10.1016/j.euromechflu.2019.09.015.
[73] Alabort E, Barba D, Reed RC. Design of metallic bone by additive manufacturing. Scr Mater 2019;164:110–4. https://doi.org/10.1016/j.scriptamat.2019.01.022.
[74] Robling AG, Castillo AB, Turner CH. Biomechanical and molecular regulation of bone remodeling. Annu Rev Biomed Eng 2006;8:455–98. https://doi.org/10.1146/annurev.bioeng.8.061505.095721.
[75] Arjunan A, Demetriou M, Baroutaji A, Wang C. Mechanical performance of highly permeable laser melted Ti6Al4V bone scaffolds. J Mech Behav Biomed Mater 2020;102:103517. https://doi.org/10.1016/j.jmbbm.2019.103517.
[76] Yánez A, Cuadrado A, Martel O, Afonso H, Monopoli D. Gyroid porous titanium structures: A versatile solution to be used as scaffolds in bone defect reconstruction. Mater Des 2018;140:21–9. https://doi.org/10.1016/j.matdes.2017.11.050.
[77] Ataee A, Li Y, Fraser D, Song G, Wen C. Anisotropic Ti-6Al-4V gyroid scaffolds manufactured by electron beam melting (EBM) for bone implant applications. Mater Des 2018;137:345–54. https://doi.org/10.1016/j.matdes.2017.10.040.
[78] Yánez A, Herrera A, Martel O, Monopoli D, Afonso H. Compressive behaviour of gyroid lattice structures for human cancellous bone implant applications. Mater Sci Eng C 2016;68:445–8. https://doi.org/10.1016/j.msec.2016.06.016.
[79] Khanoki SA, Pasini D. The fatigue design of a bone preserving hip implant with functionally graded cellular material. J Med Devices, Trans ASME 2013;7:1–2. https://doi.org/10.1115/1.4024310.
[80] Caiazzo F, Alfieri V, Bujazha BD. Additive manufacturing of biomorphic scaffolds for bone tissue engineering. Int J Adv Manuf Technol 2021;113:2909–23. https://doi.org/10.1007/s00170-021-06773-5.
[81] Bartolomeu F, Costa MM, Alves N, Miranda G, Silva FS. Additive manufacturing of NiTi-Ti6Al4V multi-material cellular structures targeting orthopedic implants. Opt Lasers Eng 2020;134:106208. https://doi.org/10.1016/j.optlaseng.2020.106208.
[82] Murr LE, Gaytan SM, Martinez E, Medina F, Wicker RB. Next generation orthopaedic implants by additive manufacturing using electron beam melting. Int J Biomater 2012; 2012.. https://doi.org/10.1155/2012/245727.
[83] Molaei R, Fatemi A. Fatigue Design with Additive Manufactured Metals: Issues to Consider and Perspective for Future Research. Procedia Eng 2018;213:5–16. https://doi.org/10.1016/j.proeng.2018.02.002.
[84] Zheng B, Zhou Y, Smugeresky JE, Schoenung JM, Lavernia EJ. Thermal behavior and microstructure evolution during laser deposition with laser-engineered net shaping: Part II. Experimental investigation and discussion. Metall Mater Trans A Phys Metall Mater Sci 2008;39:2237–45. https://doi.org/10.1007/s11661-008-9566-6.
[85] Vilaro T, Colin C, Bartout JD. As-Fabricated and Heat-Treated Microstructures of the Ti-6Al-4V Alloy Processed by Selective Laser Melting. Metall Mater Trans A 2011;42:3190–9. https://doi.org/10.1007/s11661-011-0731-y.
[86] Zheng B, Zhou Y, Smugeresky JE, Schoenung JM, Lavernia EJ. Thermal behavior and microstructural evolution during laser deposition with laser-engineered net shaping: Part I. Numerical calculations. Metall Mater Trans A Phys Metall Mater Sci 2008;39:2228–36. https://doi.org/10.1007/s11661-008-9557-7.
[87] Kobryn PA, Semiatin SL. The laser additive manufacture of Ti-6Al-4V. JOM 2001;53:40–2. https://doi.org/10.1007/s11837-001-0068-x.

[88] Lambrakos SG, Cooper KP. A general algorithm for inverse modeling of layer-by-layer liquid-metal deposition. J Mater Eng Perform 2010;19:314–24. https://doi.org/10.1007/s11665-009-9497-4.
[89] Lambrakos SG, Cooper KP. An algorithm for inverse modeling of layer-by-layer deposition processes. J Mater Eng Perform 2009;18:221–30. https://doi.org/10.1007/s11665-008-9268-7.
[90] Gong H, Rafi K, Gu H, Starr T, Stucker B. Analysis of defect generation in Ti-6Al-4V parts made using powder bed fusion additive manufacturing processes. Addit Manuf 2014;1:87–98. https://doi.org/10.1016/j.addma.2014.08.002.
[91] Kasperovich G, Haubrich J, Gussone J, Requena G. Correlation between porosity and processing parameters in TiAl6V4 produced by selective laser melting. Mater Des 2016;105:160–70. https://doi.org/10.1016/j.matdes.2016.05.070.
[92] Agarwala M, Bourell D, Beaman J, Marcus H, Barlow J. Post-processing of selective laser sintered metal parts. Rapid Prototyp J 1995.
[93] Edwards P, Ramulu M. Fatigue performance evaluation of selective laser melted Ti-6Al-4V. Mater Sci Eng A 2014;598:327–37. https://doi.org/10.1016/j.msea.2014.01.041.
[94] Shao S, Mahtabi MJ, Shamsaei N, Thompson SM. Solubility of argon in laser additive manufactured α-titanium under hot isostatic pressing condition. Comput Mater Sci 2017;131:209–19. https://doi.org/10.1016/j.commatsci.2017.01.040.
[95] Zhang B, Ham K, Shao S, Shamsaei N, Thompson SM. Effect of heat treatment and hot isostatic pressing on the morphology and size of pores in additive manufactured Ti-6Al-4V parts. Solid Free Fabr 2017 Proc 28th Annu Int Solid Free Fabr Symp - An Addit Manuf Conf SFF 2017 2020:107–14.
[96] Li P, Warner DH, Fatemi A, Phan N. Critical assessment of the fatigue performance of additively manufactured Ti-6Al-4V and perspective for future research. Int J Fatigue 2016;85:130–43. https://doi.org/10.1016/j.ijfatigue.2015.12.003.
[97] Sterling AJ, Torries B, Shamsaei N, Thompson SM, Seely DW. Fatigue behavior and failure mechanisms of direct laser deposited Ti-6Al-4V. Mater Sci Eng A 2016;655:100–12. https://doi.org/10.1016/j.msea.2015.12.026.
[98] Kimura Y, Ogawa F, Itoh T. Fatigue Property of Additively Manufactured Ti-6Al-4V under Nonproportional Multiaxial Loading. Chinese J Mech Eng (English Ed 2021:34. https://doi.org/10.1186/s10033-021-00626-8.
[99] Shrestha R, Dastranjy Nezhadfar P, Masoomi M, Simsiriwong J, Phan N, Shamsaei N. Effects of design parameters on thermal history and mechanical behavior of additively manufactured 17-4 PH stainless steel. Solid Free Fabr 2018 Proc 29th Annu Int Solid Free Fabr Symp - An Addit Manuf Conf SFF 2018 2020:1277–89.
[100] Yadollahi A, Shamsaei N. Additive manufacturing of fatigue resistant materials: Challenges and opportunities. Int J Fatigue 2017;98:14–31. https://doi.org/10.1016/j.ijfatigue.2017.01.001.
[101] Torries B, Shamsaei N. Fatigue Behavior and Modeling of Additively Manufactured Ti-6Al-4V Including Interlayer Time Interval Effects. JOM 2017;69:2698–705. https://doi.org/10.1007/s11837-017-2625-y.
[102] Torries B, Shao S, Shamsaei N, Thompson SM. Effect of inter-layer time interval on the mechanical behavior of direct laser deposited Ti-6Al-4V. Solid Free Fabr 2016 Proc 27th Annu Int Solid Free Fabr Symp - An Addit Manuf Conf SFF 2016 2016:1272–82.
[103] Yadollahi A, Shamsaei N, Thompson SM, Seely DW. Effects of process time interval and heat treatment on the mechanical and microstructural properties of direct laser deposited 316L stainless steel. Mater Sci Eng A 2015;644:171–83. https://doi.org/10.1016/j.msea.2015.07.056.
[104] Liu Y, Mahadevan S. Multiaxial high-cycle fatigue criterion and life prediction for metals. Int J Fatigue 2005;27:790–800. https://doi.org/10.1016/j.ijfatigue.2005.01.003.
[105] Fatemi A, Shamsaei N. Multiaxial fatigue: An overview and some approximation models for life estimation. Int J Fatigue 2011;33:948–58. https://doi.org/10.1016/j.ijfatigue.2011.01.003.
[106] Wang YY, Yao WX. Evaluation and comparison of several multiaxial fatigue criteria. Int J Fatigue 2004;26:17–25. https://doi.org/10.1016/S0142-1123(03)00110-5.
[107] Zerres P, Vormwald M. Review of fatigue crack growth under non-proportional mixed-mode loading. Int J Fatigue 2014;58:75–83. https://doi.org/10.1016/j.ijfatigue.2013.04.001.
[108] You B-R, Lee S-B. A critical review on multiaxial fatigue assessments of metals. vol. 18. 1996.
[109] Carpinteri A, Spagnoli A. International Journal of Fatigue Multiaxial high-cycle fatigue criterion for hard metals. vol. 23. 2001.
[110] Papadopoulos I V, Davoli P, Gorla C, Filippinp M, Bernasconi A. A comparative study of multiaxial high-cycle fatigue criteria for metals. vol. 19. 1997.
[111] Shokrieh MM, Lessard LB. Multiaxial fatigue behaviour of unidirectional plies based on uniaxial fatigue experiments m I. Modelling 1997;19.
[112] Zhu SP, Yu ZY, Correia J, De Jesus A, Berto F. Evaluation and comparison of critical plane criteria for multiaxial fatigue analysis of ductile and brittle materials. Int J Fatigue 2018;112:279–88. https://doi.org/10.1016/j.ijfatigue.2018.03.028.
[113] Yamamoto T, Itoh T, Sakane M, Tsukada Y. Creep-fatigue life of Sn-8Zn-3Bi solder under multiaxial loading. Int J Fatigue 2012;43:235–41. https://doi.org/10.1016/j.ijfatigue.2012.04.007.
[114] Branco R, Costa JD, Borrego LP, Berto F, Razavi N, Macek W. Comparison of different one-parameter damage laws and local stress-strain approaches in multiaxial fatigue life assessment of notched components. Int J Fatigue 2021:151. https://doi.org/10.1016/j.ijfatigue.2021.106405.
[115] Karolczuk A. Analysis of revised fatigue life calculation algorithm under proportional and non-proportional loading with constant amplitude. Int J Fatigue 2016;88:111–20. https://doi.org/10.1016/j.ijfatigue.2016.03.027.
[116] Molaei R, Fatemi A, Sanaei N, Pegues J, Shamsaei N, Shao S, et al. Fatigue of additive manufactured Ti-6Al-4V, Part II: The relationship between microstructure, material cyclic properties, and component performance. Int J Fatigue 2020:132. https://doi.org/10.1016/j.ijfatigue.2019.105363.
[117] Fatemi A, Molaei R, Phan N. Multiaxial fatigue of additive manufactured metals: Performance, analysis, and applications. Int J Fatigue 2020;134:1–13. https://doi.org/10.1016/j.ijfatigue.2020.105479.
[118] Roessle ML, Fatemi A. Strain-controlled fatigue properties of steels and some simple approximations. Int J Fatigue 2000;22:495–511. https://doi.org/10.1016/S0142-1123(00)00026-8.
[119] Muralidharan U, Manson SS. Equation for Estimation of Fatigue. J Eng Mater Technol 1988;110:55–8.
[120] Foti P, Santonocito D, Ferro P, Risitano G, Berto F. Determination of fatigue limit by static thermographic method and classic thermographic method on notched specimens. Procedia Struct Integr 2020;26:166–74. https://doi.org/10.1016/j.prostr.2020.06.020.
[121] Risitano A, Risitano G. Determining fatigue limits with thermal analysis of static traction tests. Fatigue Fract Eng Mater Struct 2013;36:631–9. https://doi.org/10.1111/ffe.12030.
[122] Shamsaei N, McKelvey SA. Multiaxial life predictions in absence of any fatigue properties. Int J Fatigue 2014;67:62–72. https://doi.org/10.1016/j.ijfatigue.2014.02.020.
[123] Santonocito D. Evaluation of fatigue properties of 3D-printed Polyamide-12 by means of energy approach during tensile tests. Procedia Struct Integr 2020;25:355–63. https://doi.org/10.1016/j.prostr.2020.04.040.
[124] Derrick C, Fatemi A. Correlations of fatigue strength of additively manufactured metals with hardness and defect size. Int J Fatigue 2022::106920. https://doi.org/10.1016/j.ijfatigue.2022.106920.
[125] Gates NR, Fatemi A. Multiaxial variable amplitude fatigue life analysis using the critical plane approach, Part I: Un-notched specimen experiments and life estimations. Int J Fatigue 2017;105:283–95. https://doi.org/10.1016/j.ijfatigue.2017.09.008.
[126] Niesłony A. Determination of fragments of multiaxial service loading strongly influencing the fatigue of machine components. Mech Syst Signal Process 2009;23:2712–21. https://doi.org/10.1016/j.ymssp.2009.05.010.
[127] Brighenti R, Carpinteri A. A notch multiaxial-fatigue approach based on damage mechanics. Int J Fatigue 2012;39:122–33. https://doi.org/10.1016/j.ijfatigue.2011.02.003.
[128] Anes V, Reis L, Li B, Fonte M, De Freitas M. New approach for analysis of complex multiaxial loading paths. Int J Fatigue 2014;62:21–33. https://doi.org/10.1016/j.ijfatigue.2013.05.004.
[129] Carpinteri A, Brighenti R, Macha E, Spagnoli A. Expected principal stress directions under multiaxial random loading. Part II: numerical simulation and experimental assessment through the weight function method. vol. 21. 1999.

[130] Carpinteri A, Boaretto J, Fortese G, Giordani F, Rodrigues RI, Iturrioz I, et al. Welded joints under multiaxial non-proportional loading. Theor Appl Fract Mech 2018;93:202–10. https://doi.org/10.1016/j.tafmec.2017.08.004.
[131] Anes V, Reis L, Li B, De Freitas M. New cycle counting method for multiaxial fatigue. Int J Fatigue 2014;67:78–94. https://doi.org/10.1016/j.ijfatigue.2014.02.010.
[132] Ge J, Sun Y, Zhou S. Fatigue life estimation under multiaxial random loading by means of the equivalent Lemaitre stress and multiaxial S-N curve methods. Int J Fatigue 2015;79:65–74. https://doi.org/10.1016/j.ijfatigue.2015.04.022.
[133] Carpinteri A, Fortese G, Ronchei C, Scorza D, Spagnoli A, Vantadori S. Fatigue life evaluation of metallic structures under multiaxial random loading. Int J Fatigue 2016;90:191–9. https://doi.org/10.1016/j.ijfatigue.2016.05.007.
[134] Ince A, Glinka G, Buczynski A. Computational modeling of multiaxial elasto-plastic stress-strain response for notched components under non-proportional loading. Int J Fatigue 2014;62:42–52. https://doi.org/10.1016/j.ijfatigue.2013.10.008.
[135] Carpinteri A, Vantadori S, Łagoda T, Karolczuk A, Kurek M, Ronchei C. Fatigue assessment of metallic components under uniaxial and multiaxial variable amplitude loading. Fatigue Fract Eng Mater Struct 2018;41:1306–17. https://doi.org/10.1111/ffe.12773.
[136] Ahmadzadeh GR, Varvani-Farahani A. Fatigue damage and life evaluation of SS304 and Al 7050–T7541 alloys under various multiaxial strain paths by means of energy-based Fatigue damage models. Mech Mater 2016;98:59–70. https://doi.org/10.1016/j.mechmat.2016.04.007.
[137] Carpinteri A, Spagnoli A, Vantadori S. A multiaxial fatigue criterion for random loading. n.d.
[138] Bolchoun A, Wiebesiek J, Kaufmann H, Sonsino CM. Application of stress-based multiaxial fatigue criteria for laserbeam-welded thin aluminium joints under proportional and non-proportional variable amplitude loadings. Theor Appl Fract Mech 2014;73:9–16. https://doi.org/10.1016/j.tafmec.2014.05.009.
[139] Braccesi C, Cianetti F, Lori G, Pioli D. Random multiaxial fatigue: A comparative analysis among selected frequency and time domain fatigue evaluation methods. Int J Fatigue 2015;74:107–18. https://doi.org/10.1016/j.ijfatigue.2015.01.003.
[140] Meggiolaro MA, De Castro JTP. Prediction of non-proportionality factors of multiaxial histories using the Moment of Inertia method. Int J Fatigue 2014;61:151–9. https://doi.org/10.1016/j.ijfatigue.2013.11.016.
[141] Foti P, Berto F. Fatigue assessment of high strength welded joints through the strain energy density method. Fatigue Fract Eng Mater Struct 2020;43:2694–702. https://doi.org/10.1111/ffe.13336.
[142] Radaj D, Lazzarin P, Berto F. Fatigue assessment of welded joints under slit-parallel loading based on strain energy density or notch rounding. Int J Fatigue 2009;31:1490–504. https://doi.org/10.1016/j.ijfatigue.2009.05.005.
[143] Ince A, Glinka G. Innovative computational modeling of multiaxial fatigue analysis for notched components. Int. J. Fatigue, vol. 82, Elsevier Ltd; 2016, p. 134–45. Doi: 10.1016/j.ijfatigue.2015.03.019.
[144] Berto F, Campagnolo A, Lazzarin P. Fatigue strength of severely notched specimens made of Ti-6Al-4V under multiaxial loading. Fatigue Fract Eng Mater Struct 2015;38:503–17. https://doi.org/10.1111/ffe.12272.
[145] Berto F, Lazzarin P. Fatigue strength of structural components under multi-axial loading in terms of local energy density averaged on a control volume. Int J Fatigue 2011;33:1055–65. https://doi.org/10.1016/j.ijfatigue.2010.11.019.
[146] Leuders S, Thöne M, Riemer A, Niendorf T, Tröster T, Richard HAA, et al. On the mechanical behaviour of titanium alloy TiAl6V4 manufactured by selective laser melting: Fatigue resistance and crack growth performance. Int J Fatigue 2013;48:300–7. https://doi.org/10.1016/j.ijfatigue.2012.11.011.
[147] Carroll BE, Palmer TA, Beese AM. Anisotropic tensile behavior of Ti-6Al-4V components fabricated with directed energy deposition additive manufacturing. Acta Mater 2015;87:309–20. https://doi.org/10.1016/j.actamat.2014.12.054.
[148] Sridharan N, Chaudhary A, Nandwana P, Babu SS. Texture Evolution During Laser Direct Metal Deposition of Ti-6Al-4V. JOM 2016;68:772–7. https://doi.org/10.1007/s11837-015-1797-6.
[149] Yadollahi A, Shamsaei N, Thompson SM, Elwany A, Bian L. Effects of building orientation and heat treatment on fatigue behavior of selective laser melted 17–4 PH stainless steel. Int J Fatigue 2017;94:218–35. https://doi.org/10.1016/j.ijfatigue.2016.03.014.
[150] Simonelli M, Tse YY, Tuck C. Effect of the build orientation on the mechanical properties and fracture modes of SLM Ti-6Al-4V. Mater Sci Eng A 2014;616:1–11. https://doi.org/10.1016/j.msea.2014.07.086.
[151] Bača A, Konečná R, Nicoletto G, Kunz L. Influence of Build Direction on the Fatigue Behaviour of Ti6Al4V Alloy Produced by Direct Metal Laser Sintering. Mater Today Proc 2016;3:921–4. https://doi.org/10.1016/j.matpr.2016.03.021.
[152] Sanaei N, Fatemi A, Phan N. Defect characteristics and analysis of their variability in metal L-PBF additive manufacturing. Mater Des 2019;182:108091. https://doi.org/10.1016/j.matdes.2019.108091.
[153] Molaei R, Fatemi A, Phan N. Multiaxial fatigue of LB-PBF additive manufactured 17–4 PH stainless steel including the effects of surface roughness and HIP treatment and comparisons with the wrought alloy. Int J Fatigue 2020;137:1–54. https://doi.org/10.1016/j.ijfatigue.2020.105646.
[154] Le VD, Pessard E, Morel F, Edy F. Interpretation of the fatigue anisotropy of additively manufactured TA6V alloys via a fracture mechanics approach. vol. 214. 2019. Doi: 10.1016/j.engfracmech.2019.03.048.
[155] Vantadori S, Carpinteri A, Fortese G, Ronchei C, Scorza D, Zanichelli A. Fatigue lifetime evaluation of notched components: Implementation of the control volume concept in a strain-based LCF criterion. Theor Appl Fract Mech 2018;97:400–8. https://doi.org/10.1016/j.tafmec.2017.07.001.
[156] Itoh T, Sakane M, Ohsuga K. Multiaxial low cycle fatigue life under non-proportional loading. Int J Press Vessel Pip 2013;110:50–6. https://doi.org/10.1016/j.ijpvp.2013.04.021.
[157] Carpinteri A, Ronchei C, Spagnoli A, Vantadori S. Lifetime estimation in the low/medium-cycle regime using the Carpinteri-Spagnoli multiaxial fatigue criterion. Theor Appl Fract Mech 2014;73:120–7. https://doi.org/10.1016/j.tafmec.2014.06.002.
[158] Liu B, Yan X. A new method for studying the effect of multiaxial strain states on low cycle non-proportional fatigue prediction. Int J Fatigue 2018;117:420–31. https://doi.org/10.1016/j.ijfatigue.2018.08.030.
[159] Skibicki D, Pejkowski Ł. Low-cycle multiaxial fatigue behaviour and fatigue life prediction for CuZn37 brass using the stress-strain models. Int J Fatigue 2017;102:18–36. https://doi.org/10.1016/j.ijfatigue.2017.04.011.
[160] Branco R, Costa JD, Berto F, Antunes FV. Effect of loading orientation on fatigue behaviour in severely notched round bars under non-zero mean stress bending-torsion. Theor Appl Fract Mech 2017;92:185–97. https://doi.org/10.1016/j.tafmec.2017.07.015.
[161] Kluger K, Łagoda T. New energy model for fatigue life determination under multiaxial loading with different mean values. Int J Fatigue 2014;66:229–45. https://doi.org/10.1016/j.ijfatigue.2014.04.008.
[162] Susmel L, Tovo R, Lazzarin P. The mean stress effect on the high-cycle fatigue strength from a multiaxial fatigue point of view. Int J Fatigue 2005;27:928–43. https://doi.org/10.1016/j.ijfatigue.2004.11.012.
[163] Gates NR, Fatemi A. Multiaxial variable amplitude fatigue life analysis using the critical plane approach, Part II: Notched specimen experiments and life estimations. Int J Fatigue 2018;106:56–69. https://doi.org/10.1016/j.ijfatigue.2017.09.009.
[164] Mei J, Dong P. A new path-dependent fatigue damage model for non-proportional multi-axial loading. Int J Fatigue 2016;90:210–21. https://doi.org/10.1016/j.ijfatigue.2016.05.010.
[165] Meggiolaro MA, de Castro JTP, Wu H. Non-linear incremental fatigue damage calculation for multiaxial non-proportional histories. Int J Fatigue 2017;100:502–11. https://doi.org/10.1016/j.ijfatigue.2016.12.008.
[166] Ince A, Glinka G. A generalized fatigue damage parameter for multiaxial fatigue life prediction under proportional and non-proportional loadings. Int J Fatigue 2014;62:34–41. https://doi.org/10.1016/j.ijfatigue.2013.10.007.
[167] Molaei R, Fatemi A. Fatigue performance of additive manufactured metals under variable amplitude service loading conditions including multiaxial stresses and notch effects: Experiments and modelling. Int J Fatigue 2021;145:106002. https://doi.org/10.1016/j.ijfatigue.2020.106002.
[168] Iyyer N, Sarkar S, Merrill R, Phan N. Aircraft life management using crack initiation and crack growth models - P-3C Aircraft experience. Int J Fatigue 2007;29:1584–607. https://doi.org/10.1016/j.ijfatigue.2007.03.017.
[169] Molaei R, Fatemi A, Phan N. Significance of hot isostatic pressing (HIP) on multiaxial deformation and fatigue behaviors of additive manufactured Ti-6Al-4V including build orientation and surface roughness effects. Int J Fatigue 2018;117:352–70. https://doi.org/10.1016/j.ijfatigue.2018.07.035.

[170] Ali H, Ghadbeigi H, Mumtaz K. Effect of scanning strategies on residual stress and mechanical properties of Selective Laser Melted Ti6Al4V. Mater Sci Eng A 2018;712:175–87. https://doi.org/10.1016/j.msea.2017.11.103.
[171] Parry L, Ashcroft IA, Wildman RD. Understanding the effect of laser scan strategy on residual stress in selective laser melting through thermo-mechanical simulation. Addit Manuf 2016;12:1–15. https://doi.org/10.1016/j.addma.2016.05.014.
[172] Ali H, Ma L, Ghadbeigi H, Mumtaz K. In-situ residual stress reduction, martensitic decomposition and mechanical properties enhancement through high temperature powder bed pre-heating of Selective Laser Melted Ti6Al4V. Mater Sci Eng A 2017;695:211–20. https://doi.org/10.1016/j.msea.2017.04.033.
[173] Aboulkhair NT, Maskery I, Tuck C, Ashcroft I, Everitt NM. Improving the fatigue behaviour of a selectively laser melted aluminium alloy: Influence of heat treatment and surface quality. Mater Des 2016;104:174–82. https://doi.org/10.1016/j.matdes.2016.05.041.
[174] Lavery NP, Cherry J, Mehmood S, Davies H, Girling B, Sackett E, et al. Effects of hot isostatic pressing on the elastic modulus and tensile properties of 316L parts made by powder bed laser fusion. Mater Sci Eng A 2017;693:186–213. https://doi.org/10.1016/j.msea.2017.03.100.
[175] Benedetti M, Torresani E, Leoni M, Fontanari V, Bandini M, Pederzolli C, et al. The effect of post-sintering treatments on the fatigue and biological behavior of Ti-6Al-4V ELI parts made by selective laser melting. J Mech Behav Biomed Mater 2017;71:295–306. https://doi.org/10.1016/j.jmbbm.2017.03.024.
[176] Tammas-Williams S, Withers PJ, Todd I, Prangnell PB. The Effectiveness of Hot Isostatic Pressing for Closing Porosity in Titanium Parts Manufactured by Selective Electron Beam Melting. Metall Mater Trans A Phys Metall Mater Sci 2016;47:1939–46. https://doi.org/10.1007/s11661-016-3429-3.
[177] Kasperovich G, Hausmann J. Improvement of fatigue resistance and ductility of TiAl6V4 processed by selective laser melting. J Mater Process Technol 2015; 220:202–14. https://doi.org/10.1016/j.jmatprotec.2015.01.025.
[178] Hrabe N, Gnäupel-Herold T, Quinn T. Fatigue properties of a titanium alloy (Ti–6Al–4V) fabricated via electron beam melting (EBM): Effects of internal defects and residual stress. Int J Fatigue 2017;94:202–10. https://doi.org/10.1016/j.ijfatigue.2016.04.022.
[179] Greitemeier D, Palm F, Syassen F, Melz T. Fatigue performance of additive manufactured TiAl6V4 using electron and laser beam melting. Int J Fatigue 2017; 94:211–7. https://doi.org/10.1016/j.ijfatigue.2016.05.001.
[180] Guo N, Leu MC. Additive manufacturing: Technology, applications and research needs. Front Mech Eng 2013;8:215–43. https://doi.org/10.1007/s11465-013-0248-8.
[181] Standard A. Standard Practice for Strain-Controlled Axial-Torsional Testing with Thin Walled Tube Specimens. Annual Book of ASTM Standards, Vol. 03.01, American Society of Testing and Materials; 2006.
[182] Application F. Standard Practice for Verification of Testing Frame and Specimen Alignment Under Tensile and Compressive Axial 2013.
[183] Bae KH, Lee SB. The effect of specimen geometry on the low cycle fatigue life of metallic materials. Mater High Temp 2011;28:33–9. https://doi.org/10.3184/096034011X12982896521562.
[184] Bonacuse PJ, Kalluri S. Axial-torsional fatigue: a study of tubular specimen thickness effects. J Test Eval 1993;21:160–7.
[185] de Albuquerque Simões D, de Castro JTP, Meggiolaro MA. Improved Fatigue Test Specimens With Minimum. 67th ABM Int Congr 2012:1911–23.
[186] Fatemi A, Molaei R. Novel specimen geometries for fatigue testing of additive manufactured metals under axial, torsion, and combined axial-torsion loadings. Int J Fatigue 2020;130:105287. https://doi.org/10.1016/j.ijfatigue.2019.105287.
[187] Macek W, Branco R, Trembacz J, Costa JD, Ferreira JAM, Capela C. Effect of multiaxial bending-torsion loading on fracture surface parameters in high-strength steels processed by conventional and additive manufacturing. Eng Fail Anal 2020;118:104784. https://doi.org/10.1016/j.engfailanal.2020.104784.
[188] Sanaei N, Fatemi A. Analysis of the effect of internal defects on fatigue performance of additive manufactured metals. Mater Sci Eng A 2020;785:139385. https://doi.org/10.1016/j.msea.2020.139385.
[189] Sanaei N, Fatemi A. Analysis of the effect of surface roughness on fatigue performance of powder bed fusion additive manufactured metals. Theor Appl Fract Mech 2020;108:102638. https://doi.org/10.1016/j.tafmec.2020.102638.
[190] Gong H, Rafi K, Gu H, Janaki Ram GD, Starr T, Stucker B. Influence of defects on mechanical properties of Ti-6Al-4V components produced by selective laser melting and electron beam melting. Mater Des 2015;86:545–54. https://doi.org/10.1016/j.matdes.2015.07.147.
[191] Tammas-Williams S, Withers PJ, Todd I, Prangnell PB. The Influence of Porosity on Fatigue Crack Initiation in Additively Manufactured Titanium Components. Sci Rep 2017;7:1–13. https://doi.org/10.1038/s41598-017-06504-5.
[192] Greitemeier D, Dalle Donne C, Syassen F, Eufinger J, Melz T. Effect of surface roughness on fatigue performance of additive manufactured Ti–6Al–4V. Mater Sci Technol (United Kingdom) 2016;32:629–34. https://doi.org/10.1179/1743284715Y.0000000053.
[193] Shrestha R, Simsiriwong J, Shamsaei N, Thompson SM, Bian L. Effect of build orientation on the fatigue behavior of stainless steel 316L manufactured via a laser-powder bed fusion process. Solid Free Fabr 2016 Proc 27th Annu Int Solid Free Fabr Symp - An Addit Manuf Conf SFF 2016 2016:605–16.
[194] Wang Y, Su Z. Effect of micro-defects on fatigue lifetime of additive manufactured 316L stainless steel under multiaxial loading. Theor Appl Fract Mech 2021; 111:102849. https://doi.org/10.1016/j.tafmec.2020.102849.
[195] Sanaei N, Fatemi A. Defects in additive manufactured metals and their effect on fatigue performance: A state-of-the-art review. Prog Mater Sci 2021;117: 100724. https://doi.org/10.1016/j.pmatsci.2020.100724.
[196] Pegues JWW, Shao S, Shamsaei N, Sanaei N, Fatemi A, Warner DHH, et al. Fatigue of additive manufactured Ti-6Al-4V, Part I: The effects of powder feedstock, manufacturing, and post-process conditions on the resulting microstructure and defects. Int J Fatigue 2020;132:105358. https://doi.org/10.1016/j.ijfatigue.2019.105358.
[197] Renzo DA, Sgambitterra E, Magarò P, Furgiuele F, Maletta C, Biffi CA, et al. Multiaxial fatigue behavior of additively manufactured Ti6Al4V alloy: Axial–torsional proportional loads. Mater Des Process Commun 2021;3:1–10. https://doi.org/10.1002/mdp2.190.
[198] Renzo DA, Sgambitterra E, Maletta C, Furgiuele F, Biffi CA, Fiocchi J, et al. Multiaxial fatigue behavior of SLM Ti6Al4V alloy under different loading conditions. Fatigue Fract Eng Mater Struct 2021;44:2625–42. https://doi.org/10.1111/ffe.13518.
[199] Fatemi A, Molaei R, Sharifimehr S, Shamsaei N, Phan N. Torsional fatigue behavior of wrought and additive manufactured Ti-6Al-4V by powder bed fusion including surface finish effect. Int J Fatigue 2017;99:187–201. https://doi.org/10.1016/j.ijfatigue.2017.03.002.
[200] Zhang J, Fatemi A. Surface roughness effect on multiaxial fatigue behavior of additive manufactured metals and its modeling. Theor Appl Fract Mech 2019; 103:102260. https://doi.org/10.1016/j.tafmec.2019.102260.
[201] Chan KS, Koike M, Mason RL, Okabe T. Fatigue life of titanium alloys fabricated by additive layer manufacturing techniques for dental implants. Metall Mater Trans A Phys Metall Mater Sci 2013;44:1010–22. https://doi.org/10.1007/s11661-012-1470-4.
[202] Spierings AB, Herres N, Levy G. Influence of the particle size distribution on surface quality and mechanical properties in AM steel parts. Rapid Prototyp J 2011;17:195–202. https://doi.org/10.1108/13552541111124770.
[203] Frazier WE. Metal additive manufacturing: A review. J Mater Eng Perform 2014;23:1917–28. https://doi.org/10.1007/s11665-014-0958-z.
[204] Strano G, Hao L, Everson RM, Evans KE. Surface roughness analysis, modelling and prediction in selective laser melting. J Mater Process Technol 2013;213: 589–97. https://doi.org/10.1016/j.jmatprotec.2012.11.011.
[205] Solberg K, Hovig EW, Sørby K, Berto F. Directional fatigue behaviour of maraging steel grade 300 produced by laser powder bed fusion. Int J Fatigue 2021:149. https://doi.org/10.1016/j.ijfatigue.2021.106229.
[206] Jafarlou DM, Ferguson G, Tsaknopoulos KL, Chuang AC, Nardi A, Cote D, et al. Structural integrity of additively manufactured stainless steel with cold sprayed barrier coating under combined cyclic loading. Addit Manuf 2020;35:101338. https://doi.org/10.1016/j.addma.2020.101338.
[207] Nalli F, Cortese L, Concli F. Ductile damage assessment of Ti6Al4V, 17–4PH and AlSi10Mg for additive manufacturing. Eng Fract Mech 2021;241:107395. https://doi.org/10.1016/j.engfracmech.2020.107395.
[208] Molaei R, Fatemi A. Crack paths in additive manufactured metallic materials subjected to multiaxial cyclic loads including surface roughness, HIP, and notch effects. Int J Fatigue 2019;124:558–70. https://doi.org/10.1016/j.ijfatigue.2019.03.007.
[209] Kahlin M, Ansell H, Moverare JJ. Fatigue behaviour of notched additive manufactured Ti6Al4V with as-built surfaces. Int J Fatigue 2017;101:51–60. https://doi.org/10.1016/j.ijfatigue.2017.04.009.
[210] Vayssette B, Saintier N, Brugger C, Elmay M, Pessard E. Surface roughness of Ti-6Al-4V parts obtained by SLM and EBM: Effect on the High Cycle Fatigue life. Procedia Eng 2018;213:89–97. https://doi.org/10.1016/j.proeng.2018.02.010.

[211] Yadollahi A, Mahtabi MJ, Khalili A, Doude HR, Newman JC. Fatigue life prediction of additively manufactured material: Effects of surface roughness, defect size, and shape. Fatigue Fract Eng Mater Struct 2018;41:1602–14. https://doi.org/10.1111/ffe.12799.
[212] Mower TM, Long MJ. Mechanical behavior of additive manufactured, powder-bed laser-fused materials. Mater Sci Eng A 2016;651:198–213. https://doi.org/10.1016/j.msea.2015.10.068.
[213] Wu MW, Lai PH. The positive effect of hot isostatic pressing on improving the anisotropies of bending and impact properties in selective laser melted Ti-6Al-4V alloy. Mater Sci Eng A 2016;658:429–38. https://doi.org/10.1016/j.msea.2016.02.023.
[214] Cao F, Zhang T, Ryder MA, Lados DA. A Review of the Fatigue Properties of Additively Manufactured Ti-6Al-4V. JOM 2018;70:349–57. https://doi.org/10.1007/s11837-017-2728-5.
[215] Benedetti M, Cazzolli M, Fontanari V, Leoni M. Fatigue limit of Ti6Al4V alloy produced by Selective Laser Sintering. Procedia Struct Integr 2016;2:3158–67. https://doi.org/10.1016/j.prostr.2016.06.394.
[216] Masuo H, Tanaka Y, Morokoshi S, Yagura H, Uchida T, Yamamoto Y, et al. Effects of Defects, Surface Roughness and HIP on Fatigue Strength of Ti-6Al-4V manufactured by Additive Manufacturing. Procedia Struct Integr 2017;7:19–26. https://doi.org/10.1016/j.prostr.2017.11.055.
[217] Leuders S, Lieneke T, Lammers S, Tröster T, Niendorf T. On the fatigue properties of metals manufactured by selective laser melting – The role of ductility. J Mater Res 2014;29:1911–9. https://doi.org/10.1557/jmr.2014.157.
[218] Fatemi A, Molaei R, Sharifimehr S, Phan N, Shamsaei N. Multiaxial fatigue behavior of wrought and additive manufactured Ti-6Al-4V including surface finish effect. Int J Fatigue 2017;100:347–66. https://doi.org/10.1016/j.ijfatigue.2017.03.044.
[219] Razavi N, Berto F. Directed Energy Deposition versus Wrought Ti-6Al-4V: A Comparison of Microstructure, Fatigue Behavior, and Notch Sensitivity. Adv Eng Mater 2019;1900220:1–15. https://doi.org/10.1002/adem.201900220.
[220] Solberg K, Berto F. Notch-defect interaction in additively manufactured Inconel 718. Int J Fatigue 2019;122:35–45. https://doi.org/10.1016/j.ijfatigue.2018.12.021.
[221] Nicoletto G, Kone R, Frkan M, Riva E. In fl uence of layer-wise fabrication and surface orientation on the notch fatigue behavior of as-built additively manufactured Ti6Al4V 2020;134. Doi: 10.1016/j.ijfatigue.2020.105483.
[222] Solberg K, Berto F. A diagram for capturing and predicting failure locations in notch geometries produced by additive manufacturing. Int J Fatigue 2020;134:105428. https://doi.org/10.1016/j.ijfatigue.2019.105428.
[223] Molaei R, Fatemi A, Phan N. Notched fatigue of additive manufactured metals under axial and multiaxial loadings, Part I: Effects of surface roughness and HIP and comparisons with their wrought alloys. Int J Fatigue 2021;143:106003. https://doi.org/10.1016/j.ijfatigue.2020.106003.
[224] Biswal R, Zhang X, Syed AK, Awd M, Ding J, Walther F, et al. Criticality of porosity defects on the fatigue performance of wire + arc additive manufactured titanium alloy. Int J Fatigue 2019;122:208–17. https://doi.org/10.1016/j.ijfatigue.2019.01.017.
[225] Molaei R, Fatemi A, Phan N. Notched fatigue of additive manufactured metals under axial and multiaxial loadings, part II: Data correlations and life estimations. Int J Fatigue 2022;156:106648. https://doi.org/10.1016/j.ijfatigue.2021.106648.
[226] Carrion P, Imandoust A, Simsiriwong J, Shamsaei N. Effects of layer orientation on the multiaxial fatigue behavior of additively manufactured Ti-6Al-4V. Solid Free Fabr 2018 Proc 29th Annu Int Solid Free Fabr Symp - An Addit Manuf Conf SFF 2018 2020:1384–92.
[227] Nicoletto G. Anisotropic high cycle fatigue behavior of Ti–6Al–4V obtained by powder bed laser fusion. Int J Fatigue 2017;94:255–62. https://doi.org/10.1016/j.ijfatigue.2016.04.032.
[228] Pegues J, Roach M, Scott Williamson R, Shamsaei N. Surface roughness effects on the fatigue strength of additively manufactured Ti-6Al-4V. Int J Fatigue 2018;116:543–52. https://doi.org/10.1016/j.ijfatigue.2018.07.013.
[229] Wycisk E, Solbach A, Siddique S, Herzog D, Walther F, Emmelmann C. Effects of defects in laser additive manufactured Ti-6Al-4V on fatigue properties. Phys Procedia 2014;56:371–8. https://doi.org/10.1016/j.phpro.2014.08.120.
[230] Torries B, Shamsaei N, Thompson S. Effect of build orientation on fatigue performance of Ti-6Al-4V parts fabricated via laser-based powder bed fusion. Solid Free Fabr 2017 Proc 28th Annu Int Solid Free Fabr Symp - An Addit Manuf Conf SFF 2017 2020:115–21.
[231] Wu MW, Lai PH, Chen JK. Anisotropy in the impact toughness of selective laser melted Ti-6Al-4V alloy. Mater Sci Eng A 2016;650:295–9. https://doi.org/10.1016/j.msea.2015.10.045.
[232] Gu H, Gong H, Pal D, Rafi K, Starr T, Stucker B. Influences of energy density on porosity and microstructure of selective laser melted 17-4PH stainless steel. 2013 Int. Solid Free. Fabr. Symp., University of Texas at Austin; 2013.
[233] Carrion PE, Shamsaei N, Daniewicz SR, Moser RD. Fatigue behavior of Ti-6Al-4V ELI including mean stress effects. Int J Fatigue 2017;99:87–100. https://doi.org/10.1016/j.ijfatigue.2017.02.013.
[234] Sanaei N, Fatemi A. Defect-based fatigue life prediction of L-PBF additive manufactured metals. Eng Fract Mech 2021;244:107541. https://doi.org/10.1016/j.engfracmech.2021.107541.
[235] Ritchie RO. Mechanisms of fatigue crack propagation in metals, ceramics and composites: Role of crack tip shielding. Mater Sci Eng 1988;103:15–28. https://doi.org/10.1016/0025-5416(88)90547-2.
[236] Renzo DA, Sgambitterra E, Magarò P, Furgiuele F, Maletta C, Biffi C, et al. Multiaxial fatigue behavior of additive manufactured Ti-6Al-4V under in-phase stresses. Procedia Struct Integr 2019;18:914–20. https://doi.org/10.1016/j.prostr.2019.08.243.
[237] Bressan S, Ogawa F, Itoh T, Berto F. Cyclic plastic behavior of additively manufactured Ti-6Al-4V under uniaxial and multiaxial non-proportional loading. Int J Fatigue 2019;126:155–64. https://doi.org/10.1016/j.ijfatigue.2019.05.003.
[238] Gates N, Fatemi A. Notched fatigue behavior and stress analysis under multiaxial states of stress. Int J Fatigue 2014;67:2–14. https://doi.org/10.1016/j.ijfatigue.2014.01.014.
[239] Makabe C, Socie DF. Crack growth mechanism in precracked torsional fatigue specimens. Fatigue Fract Eng Mater Struct 2001;24:607–15. https://doi.org/10.1046/j.1460-2695.2001.00430.x.
[240] Gates N, Fatemi A. Friction and roughness induced closure effects on shear-mode crack growth and branching mechanisms. Int J Fatigue 2016;92:442–58. https://doi.org/10.1016/j.ijfatigue.2016.01.023.
[241] Gates N, Fatemi A. Fatigue crack growth behavior in the presence of notches and multiaxial nominal stress states. Eng Fract Mech 2016;165:24–38. https://doi.org/10.1016/j.engfracmech.2016.08.017.
[242] Stephens RI, Fatemi A, Stephens RR, Fuchs HO. Metal fatigue in engineering. John Wiley & Sons; 2000.
[243] De-Guang S, De-Junt W. A new multiaxial fatigue damage model based on the critical plane approach. vol. 20. 1998.
[244] Lu C, Melendez J, Martínez-Esnaola JM. Modelling multiaxial fatigue with a new combination of critical plane definition and energy-based criterion. Int J Fatigue 2018;108:109–15. https://doi.org/10.1016/j.ijfatigue.2017.12.004.
[245] Liu Y, Stratman B, Mahadevan S. Fatigue crack initiation life prediction of railroad wheels. Int J Fatigue 2006;28:747–56. https://doi.org/10.1016/j.ijfatigue.2005.09.007.
[246] Soares H, Anes V, Freitas M, Reis L. Fatigue life of a railway wheel under uniaxial and multiaxial loadings. Procedia Struct. Integr., vol. 13, Elsevier B.V.; 2018, p. 1786–91. Doi: 10.1016/j.prostr.2018.12.362.
[247] Carpinteri A, Spagnoli A, Vantadori S. Multiaxial fatigue assessment using a simplified critical plane-based criterion. Int J Fatigue 2011;33:969–76. https://doi.org/10.1016/j.ijfatigue.2011.01.004.
[248] Carpinteri A, Kurek M, Łagoda T, Vantadori S. Estimation of fatigue life under multiaxial loading by varying the critical plane orientation. Int J Fatigue 2017;100:512–20. https://doi.org/10.1016/j.ijfatigue.2016.10.028.
[249] Carpinteri A, Ronchei C, Spagnoli A, Vantadori S. On the use of the Prismatic Hull method in a critical plane-based multiaxial fatigue criterion. Int J Fatigue 2014;68:159–67. https://doi.org/10.1016/j.ijfatigue.2014.05.007.
[250] Varvani-Farahani A. A new energy-critical plane parameter for fatigue life assessment of various metallic materials subjected to in-phase and out-of-phase multiaxial fatigue loading conditions. vol. 22. 2000.

[251] Carpinteri A, Spagnoli A, Vantadori S. Reformulation in the frequency domain of a critical plane-based multiaxial fatigue criterion. Int J Fatigue 2014;67:55–61. https://doi.org/10.1016/j.ijfatigue.2014.01.008.
[252] Vantadori S, Carpinteri A, Luciano R, Ronchei C, Scorza D, Zanichelli A. Mean stress effect on fatigue life estimation for Inconel 718 alloy. Int J Fatigue 2020:133. https://doi.org/10.1016/j.ijfatigue.2019.105391.
[253] Carpinteri A, Ronchei C, Scorza D, Vantadori S. Critical Plane Orientation Influence on Multiaxial High-Cycle Fatigue Assessment. Phys Mesomech 2015;18:348–54. https://doi.org/10.1134/S1029959915040074.
[254] Xu S, Zhu SP, Hao YZ, Liao D, Qian G. A new critical plane-energy model for multiaxial fatigue life prediction of turbine disc alloys. Eng Fail Anal 2018;93:55–63. https://doi.org/10.1016/j.engfailanal.2018.07.001.
[255] Lopez-Crespo P, Moreno B, Lopez-Moreno A, Zapatero J. Study of crack orientation and fatigue life prediction in biaxial fatigue with critical plane models. Eng Fract Mech 2015;136:115–30. https://doi.org/10.1016/j.engfracmech.2015.01.020.
[256] Castro F, Jiang Y. Fatigue life and early cracking predictions of extruded AZ31B magnesium alloy using critical plane approaches. Int J Fatigue 2016;88:236–46. https://doi.org/10.1016/j.ijfatigue.2016.04.002.
[257] Karolczuk A, Macha E. A review of critical plane orientations in multiaxial fatigue failure criteria of metallic materials. Int J Fract 2005;134:267–304. https://doi.org/10.1007/s10704-005-1088-2.
[258] Socie DF. Multiaxial fatigue damage models 1987.
[259] Gates NR, Fatemi A. On the consideration of normal and shear stress interaction in multiaxial fatigue damage analysis. Int J Fatigue 2017;100:322–36. https://doi.org/10.1016/j.ijfatigue.2017.03.042.
[260] Shamsaei N, Fatemi A. Small fatigue crack growth under multiaxial stresses. Int J Fatigue 2014;58:126–35. https://doi.org/10.1016/j.ijfatigue.2013.02.002.
[261] Taylor D. The theory of critical distances. Eng Fract Mech 2008;75:1696–705.
[262] Susmel L. The theory of critical distances: a review of its applications in fatigue. Eng Fract Mech 2008;75:1706–24. https://doi.org/10.1016/j.engfracmech.2006.12.004.
[263] Taddesse AT, Zhu SP, Liao D, Huang HZ. Cyclic plastic zone modified critical distance theory for notch fatigue analysis of metals. Eng Fail Anal 2021:121. https://doi.org/10.1016/j.engfailanal.2020.105163.
[264] Louks R, Gerin B, Draper J, Askes H, Susmel L. On the multiaxial fatigue assessment of complex three-dimensional stress concentrators. Int J Fatigue 2014;63:12–24. https://doi.org/10.1016/j.ijfatigue.2014.01.001.
[265] Carpinteri A, Spagnoli A, Vantadori S, Viappiani D. A multiaxial criterion for notch high-cycle fatigue using a critical-point method. Eng Fract Mech 2008;75:1864–74. https://doi.org/10.1016/j.engfracmech.2006.11.002.
[266] Carpinteri A, Berto F, Campagnolo A, Fortese G, Ronchei C, Scorza D, et al. Fatigue assessment of notched specimens by means of a critical plane-based criterion and energy concepts. Theor Appl Fract Mech 2016;84:57–63. https://doi.org/10.1016/j.tafmec.2016.03.003.
[267] Susmel L, Taylor D. A critical distance/plane method to estimate finite life of notched components under variable amplitude uniaxial/multiaxial fatigue loading. Int J Fatigue 2012;38:7–24. https://doi.org/10.1016/j.ijfatigue.2011.11.015.
[268] Liao D, Zhu SP, Qian G. Multiaxial fatigue analysis of notched components using combined critical plane and critical distance approach. Int J Mech Sci 2019;160:38–50. https://doi.org/10.1016/j.ijmecsci.2019.06.027.
[269] Ronchei C, Vantadori S. Notch fatigue life estimation of Ti-6Al-4V. Eng Fail Anal 2021:120. https://doi.org/10.1016/j.engfailanal.2020.105098.
[270] Wang Y, Wang W, Susmel L. Constant/variable amplitude multiaxial notch fatigue of additively manufactured AISI 316L. Int J Fatigue 2021;152:106412. https://doi.org/10.1016/j.ijfatigue.2021.106412.
[271] Bannantine JA. A variable amplitude multiaxial fatigue life prediction method 1989.
[272] Bannantine A, Socie DF. A Multiaxial Fatigue Life Estimation. Adv Fatigue Lifetime Predict Tech 1992;1122:249.
[273] Nezhadfar PD, Shrestha R, Phan N, Shamsaei N. Fatigue behavior of additively manufactured 17–4 PH stainless steel: Synergistic effects of surface roughness and heat treatment. Int J Fatigue 2019;124:188–204. https://doi.org/10.1016/j.ijfatigue.2019.02.039.
[274] Nezhadfar PD, Burford E, Anderson-Wedge K, Zhang B, Shao S, Daniewicz SR, et al. Fatigue crack growth behavior of additively manufactured 17–4 PH stainless steel: Effects of build orientation and microstructure. Int J Fatigue 2019;123:168–79. https://doi.org/10.1016/j.ijfatigue.2019.02.015.
[275] Sanaei N, Fatemi A. Defect-based multiaxial fatigue life prediction of L-PBF additive manufactured metals. Fatigue Fract Eng Mater Struct 2021;44:1897–915. https://doi.org/10.1111/ffe.13449.
[276] Benedetti M, Santus C. Notch fatigue and crack growth resistance of Ti-6Al-4V ELI additively manufactured via selective laser melting: A critical distance approach to defect sensitivity. Int J Fatigue 2019;121:281–92. https://doi.org/10.1016/j.ijfatigue.2018.12.020.
[277] Campbell JP, Ritchie RO. Mixed-mode, high-cycle fatigue-crack growth thresholds in Ti-6A1-4V I. A comparison of large- and short-crack behavior. Eng Fract Mech 2000;67:209–27. https://doi.org/10.1016/S0013-7944(00)00046-1.
[278] Gates NR, Fatemi A. Experimental fatigue crack growth behavior and predictions under multiaxial variable amplitude service loading histories. Eng Fract Mech 2017;174:80–103. https://doi.org/10.1016/j.engfracmech.2016.11.023.
[279] Reddy SC, Fatemi A, Mitchell MR, Landgraf RW. Small crack growth in multiaxial fatigue. ASTM STP 1992;1122:276–98.
[280] Romano S, Brückner-Foit A, Brandão A, Gumpinger J, Ghidini T, Beretta S. Fatigue properties of AlSi10Mg obtained by additive manufacturing: Defect-based modelling and prediction of fatigue strength. Eng Fract Mech 2018;187:165–89. https://doi.org/10.1016/j.engfracmech.2017.11.002.
[281] Murakami Y. Metal fatigue: effects of small defects and nonmetallic inclusions. Academic Press; 2019.
[282] Wu SC, Xiao TQ, Withers PJ. The imaging of failure in structural materials by synchrotron radiation X-ray microtomography. Eng Fract Mech 2017;182:127–56. https://doi.org/10.1016/j.engfracmech.2017.07.027.
[283] Yamabe J, Kobayashi M. Influence of casting surfaces on fatigue strength of ductile cast iron. Fatigue Fract Eng Mater Struct 2006;29:403–15.
[284] Murakami Y. Quantitative evaluation of the effect of surface roughness. Trans Japan Soc Mech Eng Ser A 1997;63:12–9.
[285] Murakami Y. Analysis of stress intensity factors of modes i, i1 and. Stress Int J Biol Stress 1985;22:101–14.
[286] Solberg K, Guan S, Razavi N, Welo T, Chan KC, Berto F. Fatigue of additively manufactured 316L stainless steel: The influence of porosity and surface roughness. Fatigue Fract Eng Mater Struct 2019;42:2043–52. https://doi.org/10.1111/ffe.13077.
[287] Pugno N, Ciavarella M, Cornetti P, Carpinteri A. A generalized Paris' law for fatigue crack growth. J Mech Phys Solids 2006;54:1333–49. https://doi.org/10.1016/j.jmps.2006.01.007.
[288] Ayatollahi MR, Razavi N, Yahya MY. Mixed mode fatigue crack initiation and growth in a CT specimen repaired by stop hole technique. Eng Fract Mech 2015;145:115–27. https://doi.org/10.1016/j.engfracmech.2015.03.027.
[289] Jones R, Michopoulos JG, Iliopoulos AP, Singh Raman RK, Phan N, Nguyen T. Representing crack growth in additively manufactured Ti-6Al-4V. Int J Fatigue 2018;116:610–22. https://doi.org/10.1016/j.ijfatigue.2018.07.019.
[290] Iliopoulos A, Jones R, Michopoulos J, Phan N, Singh RR. Crack Growth in a Range of Additively Manufactured Aerospace Structural Materials. Aerospace 2018;5:118. https://doi.org/10.3390/aerospace5040118.
[291] Newman Jr JC. FASTRAN-2: A fatigue crack growth structural analysis program. NASA STI/Recon Tech Rep N 1992;92:30964.
[292] Newman Jr JC. A Crack-Closure Model for Predicting Fatigue Crack Growth under Aircraft. Methods Model Predict Fatigue Crack Growth under Random Load 1981:53.
[293] Newman JC. Prediction of fatigue crack growth under variable-amplitude and spectrum loading using a closure model. ASTM. International 1982.
[294] Gladskyi M, Fatemi A. Load sequence effects on fatigue crack growth in notched tubular specimens subjected to axial and torsion loadings. Theor Appl Fract Mech 2014;69:63–70. https://doi.org/10.1016/j.tafmec.2013.12.001.
[295] Kasprzak JM, Lass AB, Miller CE. Development, test, and evaluation of additively manufactured flight critical aircraft components. AHS Int. 73rd Annu. Forum Technol. Display, TX, 2017.
[296] Chen J, Liu Y. Fatigue property prediction of additively manufactured Ti-6Al-4V using probabilistic physics-guided learning. Addit Manuf 2021;39:101876. https://doi.org/10.1016/j.addma.2021.101876.

[297] Zhang M, Sun CN, Zhang X, Wei J, Hardacre D, Li H. Predictive models for fatigue property of laser powder bed fusion stainless steel 316L. Mater Des 2018; 145:42–54. https://doi.org/10.1016/j.matdes.2018.02.054.
[298] Zhang M, Sun CN, Zhang X, Goh PC, Wei J, Hardacre D, et al. High cycle fatigue life prediction of laser additive manufactured stainless steel: A machine learning approach. Int J Fatigue 2019;128:105194. https://doi.org/10.1016/j.ijfatigue.2019.105194.
[299] Zhan Z, Li H. A novel approach based on the elastoplastic fatigue damage and machine learning models for life prediction of aerospace alloy parts fabricated by additive manufacturing. Int J Fatigue 2021;145:106089. https://doi.org/10.1016/j.ijfatigue.2020.106089.
[300] Zhan Z, Hu W, Meng Q. Data-driven fatigue life prediction in additive manufactured titanium alloy: A damage mechanics based machine learning framework. Eng Fract Mech 2021;252:107850. https://doi.org/10.1016/j.engfracmech.2021.107850.
[301] Bao H, Wu S, Wu Z, Kang G, Peng X, Withers PJ. A machine-learning fatigue life prediction approach of additively manufactured metals. Eng Fract Mech 2021; 242:107508. https://doi.org/10.1016/j.engfracmech.2020.107508.
[302] Hu YN, Wu SC, Withers PJ, Zhang J, Bao HYX, Fu YN, et al. The effect of manufacturing defects on the fatigue life of selective laser melted Ti-6Al-4V structures. Mater Des 2020:192. https://doi.org/10.1016/j.matdes.2020.108708.
[303] Zhan Z. Experiments and numerical simulations for the fatigue behavior of a novel TA2-TA15 titanium alloy fabricated by laser melting deposition. Int J Fatigue 2019;121:20–9. https://doi.org/10.1016/j.ijfatigue.2018.12.001.